REPORT DOCUMENTATION PAGE

Form Approved
OMB No. 0704-0188

1. AGENCY	3. REPORT TYPE AND DATES COVERED
	Final Report 01 Jan 90 - 31 Dec 92

4. TITLE AND SUBTITLE
Research support for the Laboratory for Lightwave Technology

5. FUNDING NUMBERS
2301/AS

6. AUTHOR(S)
Professor T. F. Morse

7. PERFORMING ORGANIZATION NAME(S) AND ADDRESS(ES)
Division of Engineering
Brown University
Providence, RI 02912

8. PERFORMING ORGANIZATION REPORT NUMBER

9. SPONSORING/MONITORING AGENCY NAME(S) AND ADDRESS(ES)
AFOSR/NE
BLDG 410
Bolling AFB DC 20332-6448

10. SPONSORING/MONITORING AGENCY REPORT NUMBER
AFOSR-90-0062

11. SUPPLEMENTARY NOTES

12a. DISTRIBUTION/AVAILABILITY STATEMENT
UNLIMITED

12b. DISTRIBUTION CODE

13. ABSTRACT *(Maximum 200 words)*

SEE ATTACHED ABSTRACT

14. SUBJECT TERMS	15. NUMBER OF PAGES
	16. PRICE CODE

17. SECURITY CLASSIFICATION OF REPORT	18. SECURITY CLASSIFICATION OF THIS PAGE	19. SECURITY CLASSIFICATION OF ABSTRACT	20. LIMITATION OF ABSTRACT
UNCLASSIFIED	UNCLASSIFIED	UNCLASSIFIED	UL

The Laboratory for Lightwave Technology within the Division of Engineering at Brown University is one of the few university laboratories at which it is possible to design, fabricate, and characterize optical fibers of not only traditional, but of unusual design. These fibers have an increasingly important role in a host of applications of significance to the defense requirements of the United States. Among these are fiber lasers for the measurement of clear air turbulence (in an important eye-safe region of the spectrum), fiber sensors for the measurement of temperature, strain, not only in high temperature composite materials, but in structural concrete, important for roads, runways, and buildings. We are also engaged in research, an outgrowth of our work in optical fibers, on novel techniques for the formation of nano-phase oxide particles, both ceramic and amorphous. The work on amorphous oxides is associated with our MCVD and OVD laboratories. In these, to be discussed below, we have proposed and studied a new technique for the formation of multi-component oxides to be used in the doping of optical fiber preforms. In this synthesis, an aerosol of organo-metallic precursors is convectively transported into a reaction zone where it is pyrolized. The liquid aerosol is homogeneous at the molecular level, so that subsequent reactions produce glasses that are not phase separated. This has also been used to study the synthesis of high temperature ceramic nano-phase single crystal oxides that may be produced at a high rate. The synthesis of both glasses and ceramics using novel techniques has meshed with our research in novel optical fibers and fiber sensors. In this report, we discuss the general activities of our laboratory.

Final Report

to the Air Force Office of Scientific Research: Physics

Research Support for the Laboratory for Lightwave Technology

Division of Engineering, Brown University,

Providence, RI 02912

January 1-December 31, 1992

T.F. Morse, Professor of Engineering

I. Introduction

The Laboratory for Lightwave Technology within the Division of Engineering at Brown University is one of the few university laboratories at which it is possible to design, fabricate, and characterize optical fibers of not only traditional, but of unusual design. These fibers have an increasingly important role in a host of applications of significance to the defense requirements of the United States. Among these are fiber lasers for the measurement of clear air turbulence (in an important eye-safe region of the spectrum), fiber sensors for the measurement of temperature, strain, not only in high temperature composite materials, but in structural concrete, important for roads, runways, and buildings. We are also engaged in research, an outgrowth of our work in optical fibers, on novel techniques for the formation of nano-phase oxide particles, both ceramic and amorphous. The work on amorphous oxides is associated with our MCVD and OVD laboratories. In these, to be discussed below, we have proposed and studied a new technique for the formation of multi-component oxides to be used in the doping of optical fiber preforms. In this synthesis, an aerosol of organo-metallic precursors is convectively transported into a reaction zone where it is pyrolized. The liquid aerosol is homogeneous at the molecular level, so that subsequent reactions produce glasses that are not phase separated. This has also been used to study the synthesis of high temperature ceramic nano-phase single crystal oxides that may be produced at a high rate. The synthesis of both glasses and ceramics using novel techniques has meshed with our research in novel optical fibers and fiber sensors. In this report, we discuss the general activities of our laboratory.

II. Research Completed during 1992

During the past year, several articles have appeared in various refereed journals, as well as in the proceedings of several conferences. These will be briefly discussed, and the numbers correspond to the publications below. In [1], we performed a detailed spectroscopic study on the behavior of an alumino-silicate fiber doped with europium in the +2 state. This is of interest because this was the first time in which it was possible to write a grating in a fiber that did not contain any germanium. The optical activity shows promise of a more efficient grating in a fiber than those depending upon the defect associated with the germanium e' center. Such gratings can form in-line mirrors, wavelength selectors, and are also crucial to the formation of optical strain gauges in embedded fibers.

In [2], we presented a survey of the use of optical fiber sensors in embedded concrete structures. We believe that this is a field still in its infancy, and that significant technological applications will, in the not too distant future, be applied in the field. In [3, 4, 5], we presented work on a new technique for the measurement of electric field strength. In this technique, a micro Fabry-Perot

cavity is placed atop a GRIN lens. The cavity is very short (circa 4 microns), and it is aluminized, so that no field can penetrate into the cavity, thus functioning as a Faraday cage. Since the surface is conducting, it is iso-potential, and the redistribution of charges that nulls the internal field also causes the surface to interact with the external field. This attraction causes a force on the surface, which is distorted by the electric field. This detunes the micro Fabry-Perot, and the back reflected light can be readily detected. All of the work contained in these publications was done on DC fields, with a minimum threshold of 30,000 V/m. Recently, however, we tested our probe at the 3M' Corporation's high voltage facility in Austin, TX, and discovered that the probe worked as well in alternating fields. A patent has been applied for on this device. In [4], we discuss the techniques by which the surface diaphragm is "machined" from a silicon wafer, using chip technology.

In [6], we were invited to contribute to a volume on sol-gel processing. Our aerosol technique is basically a sol-gel process; however, the great difference is that the reactions do not occur at room temperature as in traditional sol-gel synthesis, but at temperatures in excess of 1,300 C. For this reason, the usual problems of the slowness of the reactions, or the different reaction rates leading to phase separation are not important. We have also used this process in an external burner, modelled after the OVD process, to produce completely spherical, unagglomerated, single crystal particles of nano-phase powders. We have done this with alumina, titania, and zirconia. The temperatures reach nearly 3,000 K, consequently, the organo-metallic aerosol precursors are all in the gas phase, and we believe that this is the explanation for the highly spherical resulting powders. We have recently demonstrated that multi-component oxides can be produced in this manner. In particular, we have obtained YAG particles with a size distribution peaking at 35 nm. The Air Force is interested in the possible use of YAG composited materials for high temperature applications, and such particles are of importance, particularly if they can be produced in quantity at a reasonable price. We are cooperating in this research with Dr. R. Kerans of Wright-Patterson AFB, and we have recently submitted a "white paper" pre-proposal to Dr. Alex Pechenik (AFOSR, Chemistry and Materials) on this subject. We believe that our process is a significant improvement in nano-phase particle production. The key to this success is a novel burner that we have developed under Air Force sponsorship, and we are applying for a patent on this.

Reference [7] uses the modal cut-off of an optical fiber as a temperature sensor, and [8] discusses the effect of stress during processing on the temperature behavior of an optical fiber. In reference [9], we have modelled the initial stage of the CVI (Chemical Vapor Infiltration) process used in the synthesis of Nickalon-SiC composites. We believe that this can aid the understanding of the process so that higher formation rates, and thus reduced costs can result. As an outgrowth of this research, we have developed a reasonably effective fiber optic temperature sensor that, in the laboratory, has been able to measure temperature

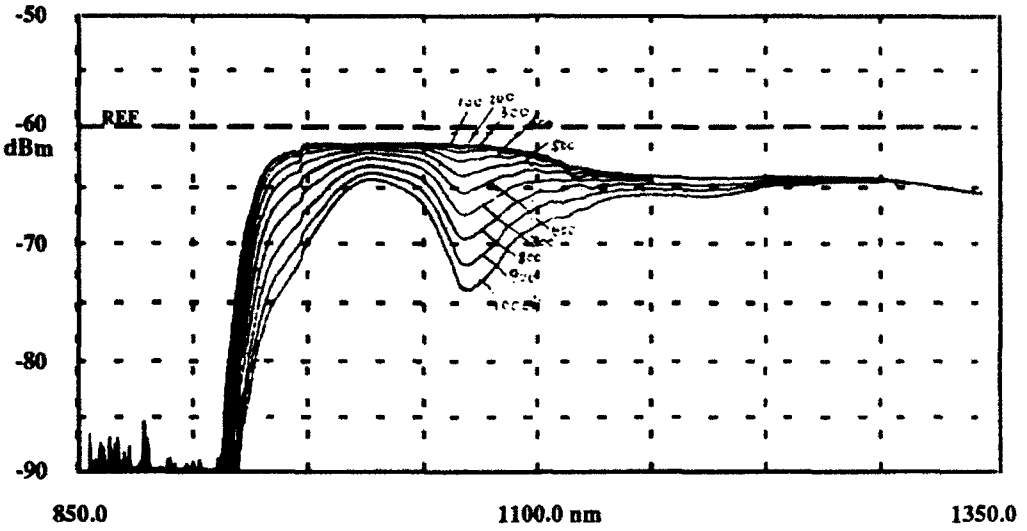

Fig. 1 Nd fiber absorption as a function of temperature and wavelength.

from room temperature to over 1000 °C. By doping a fiber heavily with Nd, (see Figures 1 and 2), and probing the 1.06 micron transition, we see that as temperature increases, the Boltzmann distribution shifts, and the absorption significantly increases. We are in the process of ruggedizing this sensor, and hope to participate in a "Sea Trial" at the end of March for the U.S. Navy. At the present time, there is no commercially available fiber optic temperature sensor that can cover this range. It is not too difficult to imagine scenarios in which the Air Force might also be interested in such a fiber optic temperature sensor. A possible configuration for such a sensor is shown in Figure 3.

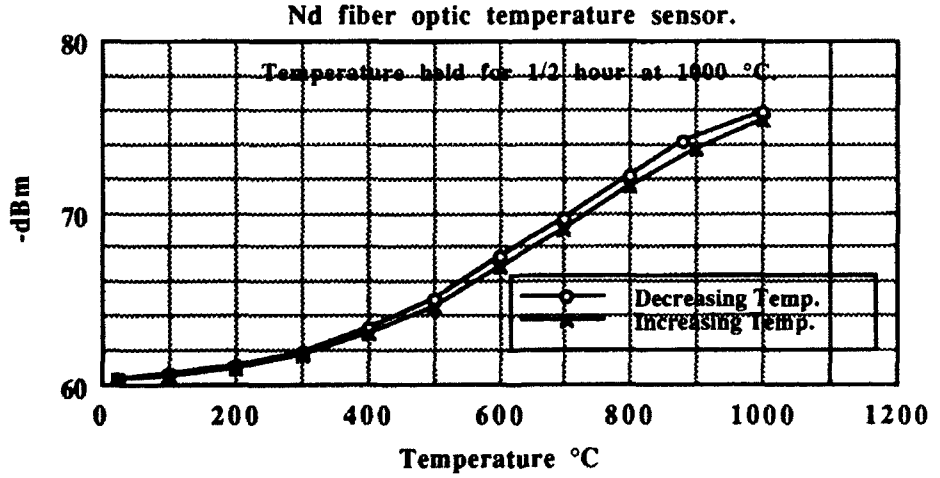

Fig. 2 Nd fiber absorption as a function of temperature.

The final article [10], has been submitted and will be presented by Prof. Fork of RPI at CLEO. One of our erbium doped fibers was given to Prof. Fork, and he has been studying its use in mode locking applications. We have also

been cooperating with Prof. S. Rand of the University of Michigan in supplying specialty fibers for their research. In both cases, these are programs that are supported by the Air Force Office of Scientific Research. We have also supplied nano-phase YAG powder to Professor Halloran of the University of Michigan, who is conducting research on YAG ceramic composites.

III. Future Directions of Research

We will continue our program on specialty fibers. In particular, we have just made a Tm doped fiber that is quite efficient, and lases near 1.8 micron just from the 4% Fresnel reflection from an uncoated fiber end. This wavelength has been cited in an Air Force RFP as a candidate for a mode-locked laser in the 2.0 micron region, which is eye safe and useful for laser ranging. We have had preliminary discussions with Raytheon on this matter. We also hope to develop develop such a laser as a possible diode pumped carbon dioxide sensor using evanescent wave techniques.

Our electric field sensor research is continuing, and we anticipate that it may be commercialized. Discussions on this are in progress with the 3M corporation. We will also continue with our work on the Nd temperature sensor, since we believe that using a high power stripe diode, that many of these sensors could be pumped from one source, thus reducing costs.

Our work on nano-phase materials will continue, since we believe that we are in a unique position to produce, with our new burner design, large quantities of such powders. We hope to be able to look at more complex oxides (staying away from super-conducting powders) for electronic applications. This work, as of now, has no separate external support, and we hope this will change in the near future.

Since we use a novel process for glass and ceramic formation, we can make multi-component oxides that are not possible with other techniques. We are hoping to use an aerosol of organo-metallic precursors to put down thin films of low temperature glasses on planar substrates of Si. No one is able to do this at the present time (for thicknesses of the order of 10 micron), and we believe that it may be possible using our aerosol process. Such surfaces could be of importance for planar waveguides, that will be an enormous market if fiber-to-the-home ever appears. The Japanese are working on this, and it is not inconceivable that our process could "leapfrog" their technology. The advantages would be that a multi-component glass might be a better host for active devices, the expansion coefficient of Si could be matched, and the processing temperatures would be significantly lower. We have convinced Bell Laboratory that if we can produce such films, they will see how they can be fashioned into planar waveguides. I have traveled to DARPA to visit Dr. Andrew Yang with Dr. John MacChesney (a Senior AT&T Fellow, and the inventor of MCVD, the process by which AT&T makes their optical fibers) to make a presentation on this matter, and we hope to

hear in the near future if DARPA will support this work. Since I believe this is important to future technology, I am sending along the brief proposal that was submitted to DARPA, which summarizes the present state of research in planar waveguides.

By using OTDR (Optical Time Domain Reflectometry) we have a new technique for measuring in-situ the curing of concrete as well as thermo-setting and thermo-plastic composites. Highly doped rare-earth glasses exhibit a large Verdet constant that makes them suitable for Faraday rotators, isolators, and circulators. We are attempting to synthesize these compositions in fiber form to see if the Verdet constant is large enough for practical devices. We are also engaged in a project in examining strain and temperature sensors in embedded materials, i.e., concrete as well as plastics. By writing "gratings" in the fiber with uv light, sensitive sensors can be formed. Thus far, all gratings have been written at 244 nm, which requires either a frequency doubled dye laser, or a frequency doubled argon ion laser. We plan to dope our glasses with different elements that will create a grating at those lines accessible to an argon ion laser with uv mirrors (275-330 nm). Thus, it would not be necessary to frequency double the laser, which would be a great simplification.

IV. Completed Research

A. Articles

1. Kyunghwan Oh, T.F. Morse, L. Reinhart, A. Kilian, and W.M. Risen, Jr., "Spectroscopic analysis of a Eu-doped aluminosilicate optical fiber preform". J. Non-Crystalline Solids, 194 (1992) 229-242.
2. Alexis Méndez, T.F. Morse, " Overview of Embedded Optical Fiber Sensors in Concrete", SPIE OE/Fibers 92, Boston, MA, September 1992, to appear.
3. T.F. Morse, et al., "A Novel Optical Fiber Electic Field Sensor", Proceedings of Conference on Sensing in the Electric Power Industry, Philadelphia, PA., EPRI Journal, to appear.
4. A. Méndez, T.F. Morse, and K.A. Ramsey, "Fiber Optic Electric Field Micro-Sensor", SPIE Proceedings, Boston, MA, September 1992, to appear.
5. Alexis Méndez, T.F. Morse, and K. Ramsey, " Micromachined Fabry-Perot Interfometer with Corrugated Silicon Diaphragm for Fiber Optic Sensing Applications, SPIE, OE/Fibers 92, Boston , MA, September 1992. to appear.
6. T.F. Morse, "High Temperature Sol-Gel Processing: Aerosol Techniques in Fiber Fabrication", to appear in "Processes for Optical Waveguides", edited by Lisa Klein,
7. Q. Zhang, T. F. Morse, L. Reinhart, A. Kililan, " Temperature Dependence of effective Cutoff Wavelength in Depressede Clad Single Mode Fiber", SPIE, OE/Fibers 92, Boston , MA, September 1992. to appear.

8. Q. Zhang, T.F. Morse, L. Reinhart, and A. Kilian, "A New Temperature Sensitive Fiber Design based on Temperature Shift of Effective Cutoff Wavelength", SPIE, OE/Fibers 92, Boston , MA, September 1992. to appear.
9. Han-Chieh Chang, Brian W. Sheldon, and T.F. Morse, "Modeling of the Isothermal Chemical Vapor Infiltration Process During the Initial Stage for Estimating the Infiltration time During the Formation of Composite Materials", submitted to the Journal of Materials Processing and Manufacturing Science.
10. to be presented at 93 CLEO, "High Power Passively Mode-Locked Er Doped Fiber Laser", Song Wu, Richard L. Fork, T.F. Morse.

B. Presentations

1. Las Vegas, Society of Fine Particles
2. Philadelphia, EPRI Workshop on Optical Sensing in Utility Applications
3. Boston, SPIE, OE/92
4. Boston, MRS (Materials Research Society)
5. San Fransico, American Association of Aerosol Research
6. With H.C. Chang, and B. Sheldon, "Reaction and Transport Kinetics "During the Formation of Composite Materials by Chemical Vapor Infiltration", Hawaii Conference on Transport Phenomen.
7. The Gordon Conference, Optical Phenomena in Glass, Tilton, NH.

C. Invited Lectures

1. AT&T Bell Laboratories, Murray Hill, NJ
2. University of Michigan, Electrical Engineering Seminar
3. Engineering Research Society Workshop, Hawaii
4. Ruhr University, Bochum, Germany

D. Patents

1. A novel device for the detection of AC and DC electric fields, submitted January 23, 1992.

V. Research Funding

The funding from the Air Force Office of Research of great importance to the activities our laboratory. For completeness, I have listed below the other agencies that have contributed to this effort during the past year. The support is primarily in the form of individual investigator, multi-year grants from the federal government. This comes largely from diverse groups within NSF and the Department of Defense. NSF: Materials Science, Electrical Sciences and Telecommunications, Chemical and Thermal Systems, Mechanics of Materials and Solids. DoD: Air Force Office of Scientific Research, Physics; Army Research Office, Durham, Materials Science. EPRI (Electric Power Research Institute), Rotating Machinery, and the Gas Research Institute (Exploratory Research). Thus, in terms of traditional departmental groupings, research is funded by

Mechanical, Electrical, and Civil Engineering, as well as Materials Science, and Physics. The equipment in our laboratory represents an investment of approximately $2,000,000, of which $800,000 (replacement value) has come from industry.

A. Present Research Funding

1. "Nonlinear Effects in Silica Based Optical Fibers". National Science Foundation, Telecommunications and Electrical Sciences, Materials Science, NSF-ECS-8916997, $295,000, March 1-1990-February 28, 1993.

2. "Optical Fiber Technique for Sensing Voltage, (A.C. and D.C.) and Electric Field", Electric Power Research Institute, $300,000, February 1, 1990-January 31, 1993.

3. ``Research Support for the Laboratory for Lightwave Technology", Air Force Office of Scientific Research, Physics, AFOSR-90-0062, $555,000, October 1, 1989-November 30, 1992. This proposal has been renewed for three years for $660,000.

4. ``Fundamental Studies of Embedded Fibers in Composite Materials", National Science Foundation, Solid-Geomechanics Program, Mechanics, Structures, and Materials, with Prof. K.S. Kim, NSF-MSS-8904872, $170,000, June 15, 1989-June 14, 1992.

5. ``Fundamentals of Embedded Optical Fibers in Structural Concrete'', National Science Foundation, Non-Destructive Evaluation-MSS-901793, $300,000, February 1991-March 1993, with K.S. Kim (Solid Mechanics)

6. ``A Holmium Fiber Laser for Monitoring of carbon dioxide'', The Gas Research Institute, $95,000, eighteen months, August 1992, January, 1994.

7. "The Optical Fiber Sensors for In-Situ Temperature and Strain Measurements in Composite Materials", National Science Foundation, MS&P, $153,100, 9/15/92-9/14/93. First of three years. With Profs. Kim and Sheldon.

8. "An Optical Fiber Temperature Sensor for Detection of Ship-Board Fires", Naval Surface Weapons System, 3 months, $5,000, beginning November 1992.

B. Proposals in Progress

1. Organo-metallic aerosol pyrolysis for the formation of low melting point glasses for planar waveguides. A joint presentation between AT&T and the Laboratory for Lightwave Technology is being prepared for DARPA.

2. A proposal is being submitted to NSF and DOE on nano-phase powder synthesis.

New temperature-sensing approach based on temperature shift of effective cutoff wavelength

Q. Zhang, T. F. Morse, L. Reinhart, A. Kilian
Laboratory for Lightwave Technology, Division of Engineering
Brown University, Providence, R.I. 02912

Abstract

A new approach for temperature sensing between 20-300°C using a single mode fiber with a depressed cladding is presented. The effective cutoff wavelength (780nm) is a linear function of temperature for this fiber because of the mismatch of the thermal expansion coefficients between the core and cladding. Consequently the attenuation coefficient in the region of the cutoff wavelength is linearly dependent upon temperature. The advantage of this sensor is that the sensing wavelength may be selected between 600-780nm.

Introduction

Many different types of temperature sensing fiber have been reported[1]. They generally require either a special dopant[12], i.e. Nd, Ho, Er, etc., in the fiber core or other fiber components[2], i.e. fiber gratings. We report a preliminary study of a novel temperature sensitive fiber based on the shift of the effective cutoff wavelength λ_c of a depressed clad single mode fiber. Since this fiber design does not require a special dopant or fiber components, it can be relatively inexpensive and easy to fabricate. It has recently been found that the effective cutoff wavelength for this fiber is very temperature sensitive, and the attenuation coefficient in the cutoff region becomes a strong function of temperature. The theoretical explanation based on the thermal expansion mismatch between the core and cladding is described in the next section. The experimental results show that as λ_c shifts to longer wavelength the transmitted power increases linearly over a transition spectrum of the effective cutoff wavelength so that there is flexibility in choosing a suitable sensing wavelength. Therefore, an inexpensive light source can be easily found.

Theory

In a depressed clad fiber with core radius a, inner-cladding b and outer-cladding radius c, the core and cladding are composed of different dopant concentrations, each having different thermal expansion coefficients. Stresses will develop as temperature changes. The thermally induced stresses due to thermal expansion mismatching within each layer can be estimated by the following approach.

Since the fiber is drawn at relatively low tension, approximately 5g for the present fiber, and the temperature region under study (20-300°C) is far below the glass transition point, it is assumed that the residual stress[3] that is frozen in the fiber during the drawing process remaines a constant. It is further assumed[10] that Young's modulus, E, and Poisson's ratio, ν, are temperature invariants. The average thermal expansion coefficient α is independent of temperature because it is assumed that thermal expansion

in the fiber is linear. In addition, when the absence of shear stress is assumed, the stress components, σ_r, σ_θ and σ_z in cylindrical coordinates r, θ and z, as shown in Fig.1, will depend on r only[4]. ε_r, ε_θ and ε_z are the corresponding strain components. Using superscripts c, i, o to denote stress components in the core, inner-cladding and outer cladding (σ^c, σ^i, σ^o), stress and appropriate boundary conditions may be expressed as follows:

$$\begin{aligned}
\frac{\partial u^j}{\partial r} &= \varepsilon_r^j \\
\frac{u^j}{r} &= \varepsilon_\theta^j \\
\sigma_r^j(r) &= \frac{E}{(1+\nu)(1-2\nu)}[\varepsilon_r^j(1-\nu)+\varepsilon_\theta^j\nu] \qquad (j=c,i,o) \\
\sigma_\theta^j(r) &= \frac{E}{(1+\nu)(1-2\nu)}[\varepsilon_r^j\nu+\varepsilon_\theta^j(1-\nu)]
\end{aligned} \tag{1}$$

where an intermediate variable, the radial expansion displacement u^j $(j = c, i, o)$ is introduced for convenience. Apply Newton's law to each layer:

$$\begin{aligned}
r\sigma_r^c(r) &= \int_0^r \sigma_\theta^c(r')\mathrm{d}r' \\
r\sigma_r^i(r) - a\sigma_r^i(a) &= \int_a^r \sigma_\theta^i(r')\mathrm{d}r' \\
r\sigma_r^o(r) - b\sigma_r^o(b) &= \int_b^r \sigma_\theta^o(r')\mathrm{d}r'
\end{aligned} \tag{2}$$

And the boundary conditions are:

$$\begin{aligned}
&\sigma_r^i(a) = \sigma_r^c(a) \qquad && u^c(0) = 0 \\
&\sigma_r^o(b) = \sigma_r^i(b) \qquad && u^i(a) = u^c(a) - a\Delta T\alpha^c \\
&\sigma_r^o(c) = 0 \qquad && u^o(b) = u^i(b) - b\Delta T\alpha^i
\end{aligned} \tag{3}$$

where ΔT is the temperature difference with respect to room temperature. α^c, α^i are the thermal expansion coefficients of the core and inner-cladding, respectively. Because of the fact that $a \ll c$, the solutions for Eqs. (1) and (2) are:

$$\begin{aligned}
\sigma_r^c = \sigma_\theta^c &= \frac{1}{2}\left[b^2\left(\frac{1}{b^2}-\frac{1}{c^2}\right)\alpha^i + \alpha^c\right]\frac{E\Delta T}{(1-\nu^2)} \\
\sigma_r^i &= \frac{1}{2}\left[-b^2\left(\frac{1}{b^2}-\frac{1}{c^2}\right)\alpha^i - a^2\left(\frac{1}{c^2}-\frac{1}{r^2}\right)\alpha^c\right]\frac{E\Delta T}{(1-\nu^2)} \\
\sigma_\theta^i &= \frac{1}{2}\left[-b^2\left(\frac{1}{b^2}-\frac{1}{c^2}\right)\alpha^i - a^2\left(\frac{1}{c^2}+\frac{1}{r^2}\right)\alpha^c\right]\frac{E\Delta T}{(1-\nu^2)}
\end{aligned} \tag{4}$$

The relations of refractive index and stress, i.e. the photoelastic effects, are expressed ($\sigma_z = 0$) as:

$$\Delta n_r^j = C_1\sigma_r^j + C_2\sigma_\theta^j \qquad (j=c,i) \tag{5}$$

where C_1 and C_2 are the photoelastic coefficients, $C_1 = 0.7 \times 10^{-12}\mathrm{Pa}^{-1}$, $C_2 = 4.2 \times 10^{-12}\mathrm{Pa}^{-1}$ [11]. These values were taken from SiO_2. For the present fiber the dopant concentrations were low, the coefficients

should be close to that of SiO_2. The refractive index change in the radial direction is given by Δn_r^j. The index changes in the circumferential and axial directions are ignored because when a signal light is linearly polarized propogating in the cylindrically symmetric fiber, only the radial component of the refractive index affects the propogation constant. In Eq.(5) σ_z^j is excluded because it is originally assumed to be a constant which does not contribute to the index change.

The theoretical cutoff wavelength λ_c is given by[9]:

$$\lambda_c = \frac{2\pi a}{V_c}\sqrt{(n_1 + \Delta n_r^c)^2 - (n_2 + \Delta n_r^i)^2} \tag{6}$$

where $V_c = 2.405$ is the normalized cutoff frequency of the second linear polarized mode (LP_{11}). n_1, n_2 are the original indices of the core and inner-cladding, respectively. Eq.(6) indicates that both indices of the core and inner-cladding have an effect on the cutoff wavelength.

Ignoring the modal interference noise, the attenuation coefficient of LP_{11} mode in the cutoff region is defined as:

$$\alpha_{11}(\lambda) = \frac{I(\lambda) - I_0(\lambda_c)}{\Delta I} = K_{11}\frac{\lambda_c - \lambda}{\Delta\lambda} \tag{7}$$

where I, I_0 are the total signal light intensity and fundamental mode intensity, respectively. K_{11} is the LP_{11} mode excitation efficiency, and λ is the probe wavelength. In eq. (7), $\Delta I = I_1 - I_0$, and I_1 is given by the intersection of the slope of the portion of the power curve that decays in the cutoff transition region, and the slope of the dual mode power curve that increases near the cutoff region in a transmission spectrum. The mode cutoff transition bandwidth is given as $\Delta\lambda$.

Experiment

The fiber was fabricated by the MCVD process. The inner-cladding had 10 mol% B_2O_3 and the core was doped with 200ppm Eu and 2 mol% Al_2O_3. The refractive index profile is shown in Fig.2. Two 4m length of the same fiber were coiled at different diameters. Fiber 1 had a diameter of 9.5cm and Fiber 2 5.7cm. Since the effective cutoff wavelength is very sensitive to bending[5,6,7,8], the varied coil diameter gives the flexibility of choosing the probe's sensing wavelength. A suitable light source can be chosen accordingly. The coiled fiber was then put into a single heating zone temperature controlled furnace. An Anritsu MG922A white light source and an Ando AQ6312B optical spectrum analyzer were used to measure the transmission spectra *in situ*.

Before the fiber can be used for temperature sensing, a thermal treatment is necessary. This is because the fiber coating might not be completely cured, and therefore its structure could be changed at higher temperature. Our observation is that the coating needs to be heat treated at 100°C for about 5 minutes. Then it stays in a relatively stable condition between room temperature and approximately 300°C in which the modal interference is minimum. When temperature reaches 300°C, the coating starts to burn. During the process of the coating burn-off, the cutoff wavelength transition region shows anomalous modal noise, which is due to both optical fiber waveguide properties and the coating. The modal noise limits the performance of this fiber.

Fig. 3 (a), (b) is the measured temperature dependence of transmission spectra of the fibers in different coil radii, respectively. As we can see, the effective cutoff wavelength shifts to longer wavelength as temperature increases. The cutoff wavelength is determined by where the tangent to the power step intersects the base line. A probe wavelength can be selected between 690 - 720 nm or 620 - 650 nm from Fig. 3 (a), (b), respectively. In these wavelength regions, there are commercially available AlGaInP Diode lasers at 690 nm and HeNe laser at 633 nm. So these two wavelengths were chosen for investigating the linearity of its temperature response. The results are shown in Fig. 4. The calculated data from Eq. (7) agree reasonablly well with the experimental data. The measured sensitivity from Fig. 4 is approximately 0.003 dB/°C.

Conclusions

A new temperature sensitive fiber design based on the effect of temperature shift of the effective cutoff wavelength has been presented. Its dynamic range is 20-300 °C. The sensitivity is 0.003 dB/°C. The advantage of this sensor is that the probe wavelength can vary between 600 and 780 nm. Performance limitations are attributed to modal noise occuring at temperatures above 400 °C.

Acknowledgements

We thank Dr. S.Y. Shen for his stimulating discussions. This research was supported by grants from the National Science Foundation, Telecommunications and Electrical Science NSF-ECS-8916997, and the Department of Defense, AFOSR-90-0062.

References

1. E. Snitzer, W. W. Morey and W. H. Glenn, "Fiber optic rare earth temperature sensors", Proc. 1st International Conference on Optical Fiber sensors, *IEE Conf. Publication 221*, p. 78, 1983.
2. W. W. Morey, G. Meltz and W. H. Glenn, "Fiber optic Bragg Grating Sensors", *SPIE*, vol. 1169, p. 98, 1989.
3. Y. Hibino, F. Hanawa and M. Horiguchi, "Drawing-induced residual stress effects on optical characteristics in pure-silica-core single-mode fibers", *J. Appl. Phys.*, 65(1), p. 30, 1989.
4. U. C. Paek and C. R. Kurkjian, "Calculation of cooling rate and induced stresses in drawing of optical fibers", *J. American Ceramic Society*, vol. 58, no. 7-8, p. 330, 1975.
5. D. L. Franzen, "Determining the effective cutoff wavelength of single-mode fibers: An interlaboratory comparison", *J. Lightwave Technology*, vol. 3, no. 1, p. 128, 1985.
6. V. Shah, "Curvature dependence of the effective cutoff wavelength in single-mode fibers", *J. Lightwave Technology*, vol. 5, no. 1, p. 35, 1987.
7. S. A. Jacobs and D. W. Peckham, "The anomalous structure observed in single mode fiber cutoff wavelength measurements: Theory and solutions", *Technical Digest- Symposium on optical fiber measurements*, National Inst. Standard and Tech. Boulder, Colorado. 1990.
8. A. S. Sudbo and E. Nesset, "Attenuation coefficient and effective cutoff wavelength of the LP_{11} modes in curved optical fibers", *J. Lightwave Technology*, vol. 7, no. 5, p. 785, 1989.

9. M. Monerie, "Propagation in doubly clad single mode fibers", *IEEE J. Quantum Electron.*, v. 18, no. 4, p. 535, 1982.
10. N. P. Bansal and R. H. Doremus, ***Handbook of glass properties***, Academic Press, 1986.
11. W. Primak and D. Post, "Photoelastic constant of vitreous silica and its elastic coefficient of refractive index", *J. Appl. Phys.*, vol. 30, p. 779, 1959.
12. K. W. Quoi, R. A. Lieberman, L. G. Cohen, D. S. Shenk and J. R. Simpson, "Rare-earth doped optical fibers for temperature sensing", *J. Lightwave Technology*, vol. 10, No. 6, p. 847, 1992.

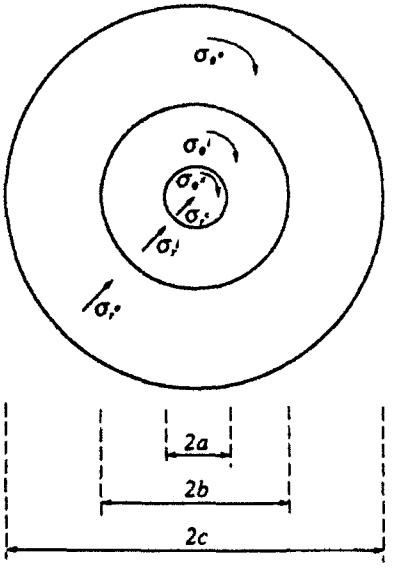

Fig.1 Thermal induced stresses in a depressed clad fiber

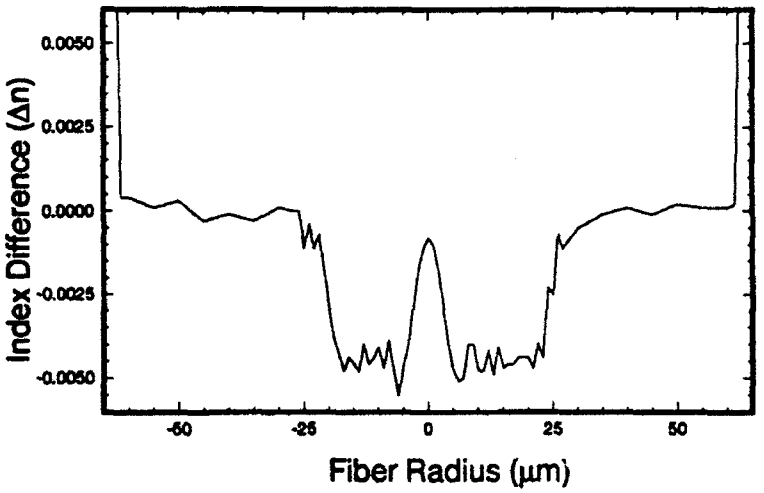

Fig.2 Refractive index profile of the fiber.

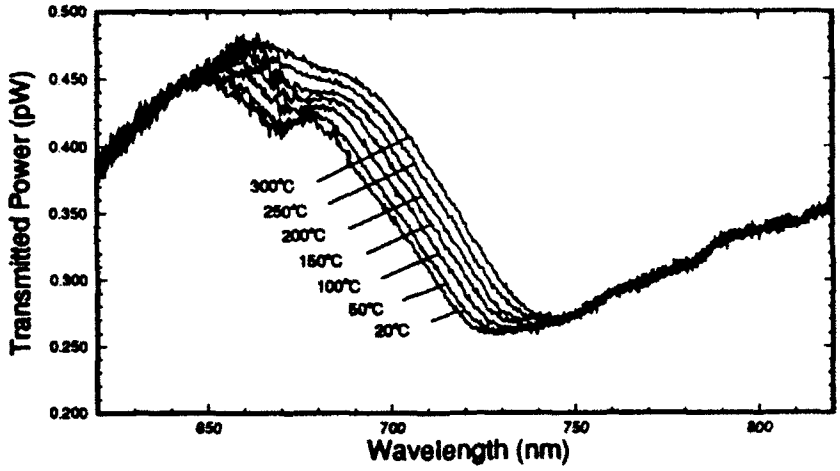

(a)

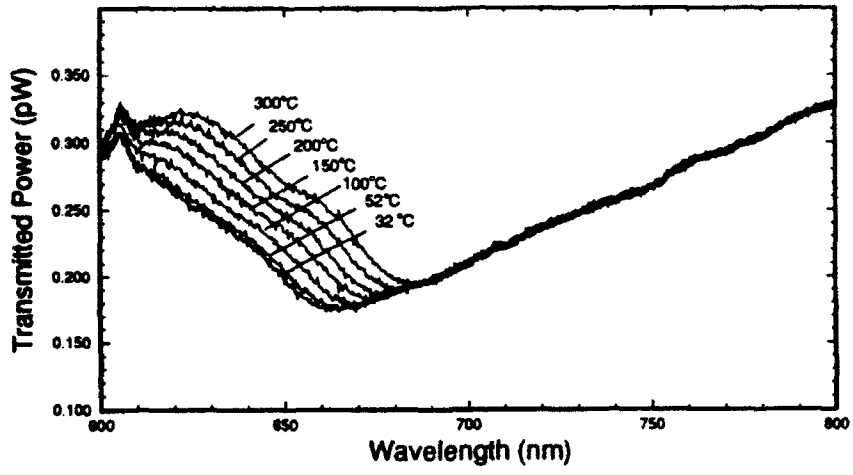

(b)

Fig.3 Temperature dependence of transmission spectra. (a) Fiber 1 coiled in 9.5cm dia; (b) Fiber 2 coiled in 5.7cm dia.

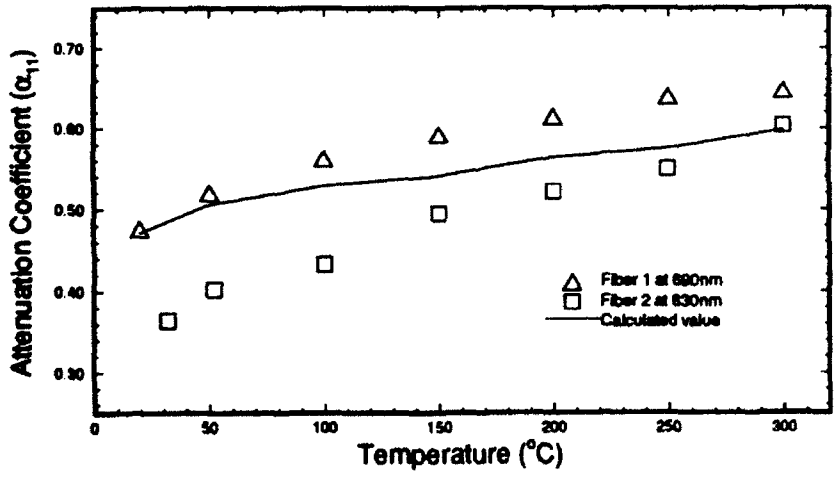

Fig.4 Temperature dependence of attenuation coefficient in the cutoff region.

A NOVEL OPTICAL FIBER ELECTRIC FIELD SENSOR

T. F. Morse
A. Méndez
L. Reinhart
Laboratory for Lightwave Technology
Brown University, Providence, RI 02912

J. Stein
EPRI
3412 Hillview Avenue
Palo Alto, CA 94304

ABSTRACT

A new method and apparatus are presented by which electric fields (AC and DC) can be measured above ground using a variable gap, Fabry-Perot cavity transducer which mounts directly on a multimode optical fiber waveguide. The sensor is characterized by being small, lightweight, unobtrusive, accurate and immune to electromagnetic interference (EMI), temperature or pressure effects.

This work is intended as exploratory research to determine the feasibility of implementing the proposed technology as an efficient and effective new electric field sensor to be used by electric power utilities. To achieve this goal, a laboratory prototype was designed, built and tested. The results of its evaluation are used to demonstrate the sensor's concept, as well as to identify technical difficulties and limitations, and possible improvements in its design.

DC electric fields in the range of 0 to $300 KV/m$ have been successfully measured. The minimum intensity detected was of the order of $40 KV/m$. This relatively low sensitivity is due to the high stiffness of the diaphragm arising from the high boron-diffusion and the increased thickness of $3.5 \mu m$ of the fabricated diaphragms, as opposed to the design value of $2 \mu m$. However, higher sensitivities are possible by thinning the diaphragm, increasing the radius, reducing the boss ratio or decreasing the corrugation depth.

In the sections to follow, the different aspects associated with the analysis, design and fabrication of the prototype are discussed in more detail.

A NOVEL OPTICAL FIBER ELECTRIC FIELD SENSOR

INTRODUCTION

With the strong dependence that today's society has on electricity, the safe, reliable and efficient generation, transmission and distribution of electric power has become of vital importance. Furthermore, in order to monitor, control and meter properly electric energy an extensive number of measurements are necessary within a given power network. This is confirmed by a recent study which indicates that electric power utilities, along with gas and water utilities, are the most measurement intensive sectors of the U.S. economy [1].

In this context, the measurement of electric fields in high voltage, high power equipment is of fundamental importance to the power industry. Knowledge of the local electric fields, both AC and DC, present in generators, transformers, power lines or any other HV component is essential in the understanding of their operation and behavior, as well as in the verification of new or modified designs. In addition, defective, malfunctioning or degraded equipment can be detected by continuously monitoring the changes in the electric fields being generated. An early indication of changing field gradients would allow the modification of the operating conditions to take whatever preventive maintenance measures are necessary to avoid equipment damage.

Furthermore, the use of extremely high voltage (EHV, up to 750 kV) and ultra high voltage (UHV, up to 1 MV) DC power lines to satisfy the ever-increasing demand of electricity has necessitated the investigation of associated physical phenomena, owing to the creation of an extensive space charge region, in contrast to the case of traditional AC power lines. Moreover, recent concerns over the biological effects of electromagnetic radiation [2,3] have motivated studies on the electric fields generated by power and transmission lines.

All this has promoted the development of new, efficient and economical sensors and sensing technologies. Among these, Fiber Optics has received special attention by power utilities over the last few years [4-7]. Optical fibers are attractive for the communication, measurement and control of data within HV plants because of their wide bandwidth, low transmission loss, small size and weight, electrical isolation, immunity to EMI, high signal security, ruggedness, reliability, ease of maintenance and potential low cost.

Optical fiber sensors offer the possibility of measuring a wide variety of parameters, from temperature and pressure, to chemical species and strain with high accuracy and sensitivity. Furthermore, they also offer the potential for distributed sensing, where the entire length of the fiber acts as a sensing element. This would allow, for instance, the monitoring in real-time of an entire power plant by placing optical fiber sensors in specific or important locations throughout the entire facility.

FABRICATION OF A PROTOTYPE

To demonstrate the sensor's concept as well as to identify technical difficulties and limitations a laboratory prototype was designed and built. The fabrication process for the protype sensing probe involved three tasks. Namely, the fabrication of silicon diaphragms, the deposition of mirror coatings and assembly of the FOC and finally, the attachment of the assembled FPC to the end of a especially terminated optical fiber.

The corrugated diaphragms were fabricated using standard photolithographic and silicon micromachining techniques[†] which consisted in the following. First, a small octagonal recession $1.7\mu m$ deep and slightly larger than the diaphragm itself is made on the epi side of a (100) silicon wafer using a KOH solution. Afterwards, a series of grooves, $5\mu m$ deep, are etched away from the surface of the wafer by means of an isotropic etching solution of hydrofluoric, nitric and acetic acid. These channels will define the top side of the corrugations. A heavy diffusion of boron is then introduced to act as an etch-stop for a wet anisotropic etch on the backside of the wafer. Since the boron diffusion follows the contour of the epitaxial features on the wafer, a deep etching on the backside of the wafer will result in a thin, corrugated, diaphragm with a thickness dependent on the depth of the boron diffusion. The small vent holes on the diaphragm are obtained by blocking the diffusion of boron with a SiO_2 mask, thus allowing the etch to attack the silicon all the way through in these regions.

The aspect of the final product can be appreciated in Fig. 1.8, which shows an SEM picture of the back-side view of the silicon diaphragm. Notice how well defined the structural features are such as the corrugations and the vent holes, as well as the smooth, shiny, finish of the silicon. The diaphragms appear translucent, with an orange-red color. Fig. 1.9 shows an SEM picture of the cross-section of the diaphragm, where the depth and smoothness of the grooves that define the corrugations can clearly be appreciated.

The Fabry-Perot cavity (FPC) is formed by bonding together a mirrored diaphragm with a metallized pyrex substrate. Since this arrangement has to be conductive all around for it to act as a Faraday cage as well as partially transmitting so that light can be coupled in and out of the cavity, it becomes necessary to have two distinct metal layers on the same glass substrate, each one with a different thickness. A thin, partially-transmitting, film on the center and a thick, highly-conductive, one extending from the limits of the inner film out to the limits of the cavity.

For this application pyrex microscope cover slips, $1x1cm$ square, $300\mu m$ thick and polished flat to $5\lambda/in.$ were used. Pyrex glass is used because its coefficient of thermal expansion matches that of silicon and because it is suitable for the bonding process used in this work. However, any other sodium-bearing glass could be used. Cavities are bonded together using the anodic bonding technique [11]. The final assembly of the cavities requires mounting the bonded miniature FPC on the tip of an optical fiber, and the attachment of a GRIN lens, as seen in Fig 1.2.

[†]Among these techniques are traditional micro-electronics fabrication processes such as wet chemical etching, plasma etching, dopant diffusion, oxidation, and thin-film evaporation.

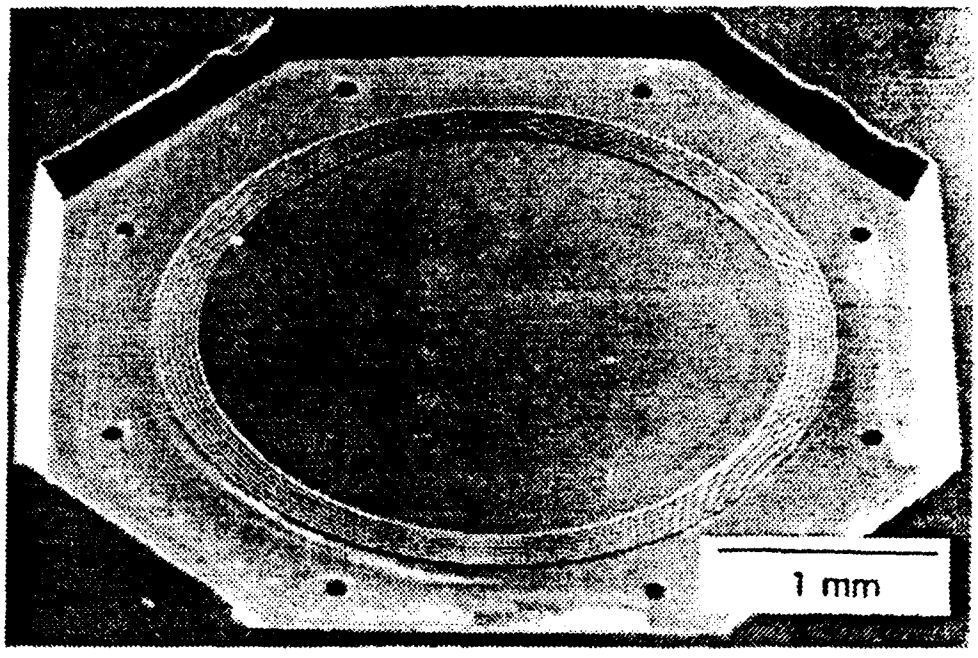

Figure 1.8: SEM perspective of silicon diaphragm.

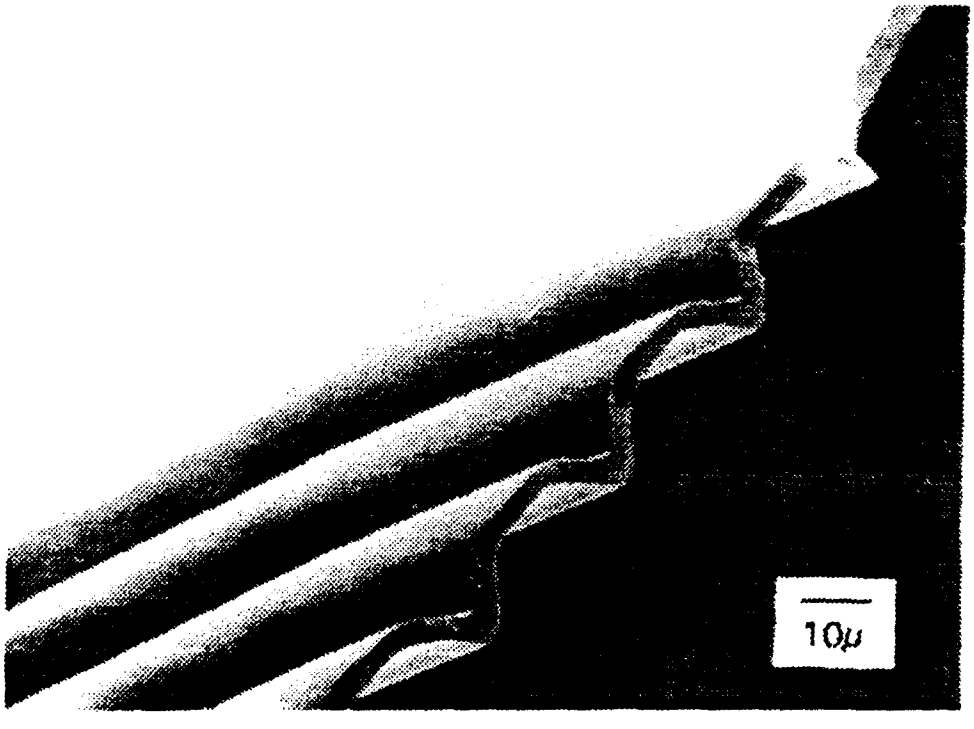

Figure 1.9: Detail of the corrugations.

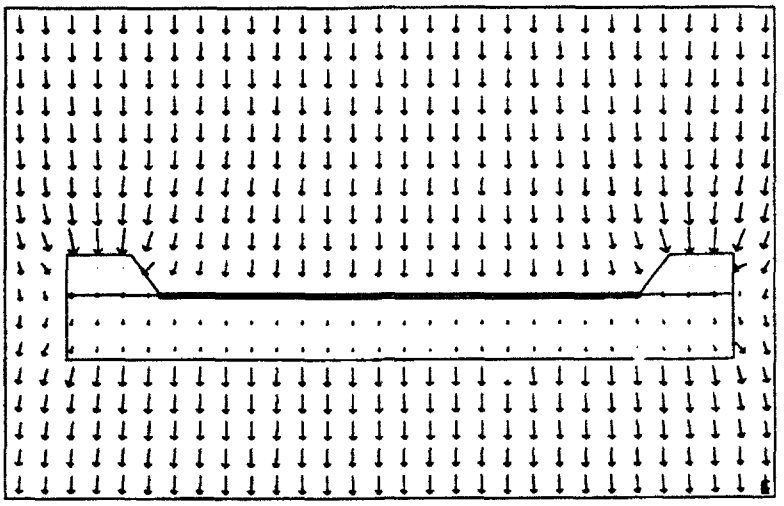

a)

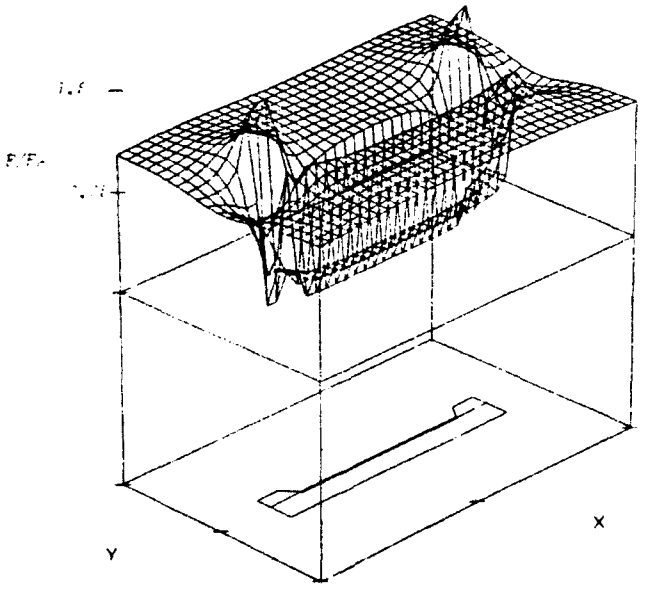

b)

Figure 1.6: a) Electric field arrow plot and b) Electric field distribution for $\alpha = 0°$

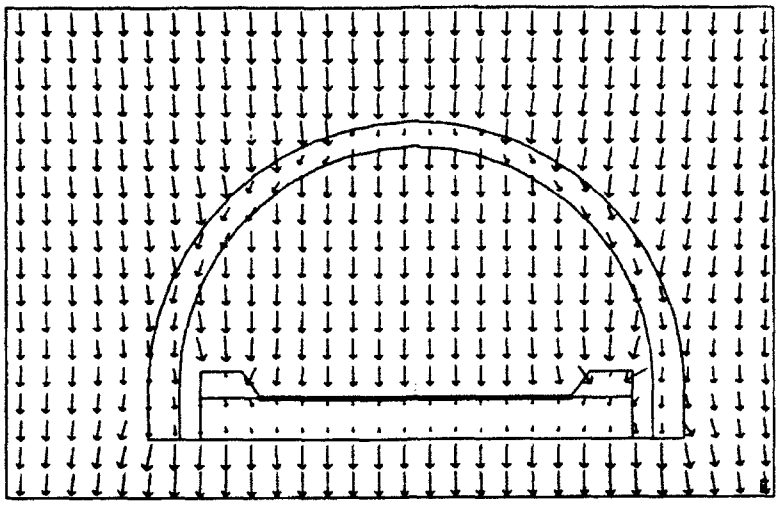

a)

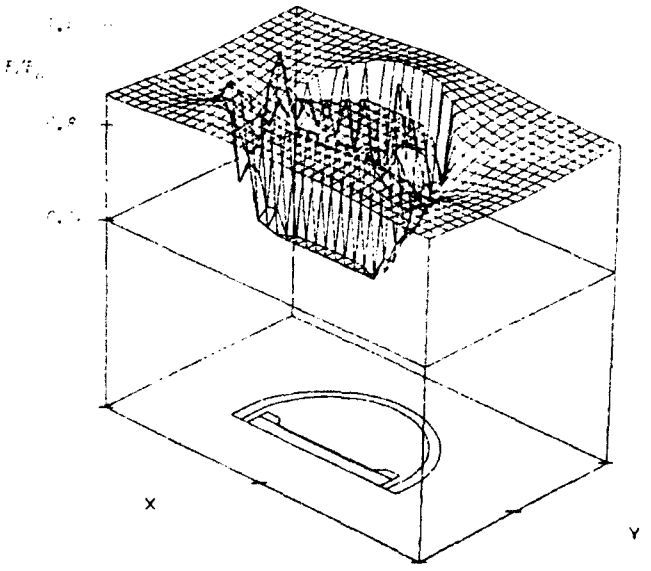

b)

Figure 1.7: a) Electric field lines for covered sensor and b) Surface electric field for covered sensor

ELECTROSTATIC ANALYSIS

Since the sensor is designed for the measurement of electric fields in and around HV environments, it is of vital importance to know what are the effects that it introduces into the field. To answer this question numerical calculations were performed using ELECTRO [10]. ELECTRO is a software program for the calculation of two-dimensional (including rotational symmetric), static or quasi-static electric fields using the boundary element method.

Static, 2-D analyses* were performed for three different probe orientations: $\alpha = 0°, 45°$ and $90°$, assuming that a uniform electric field E_0 prevailed before the introduction of the cavity. This is achieved by defining a constant potential across a given distance in the program.

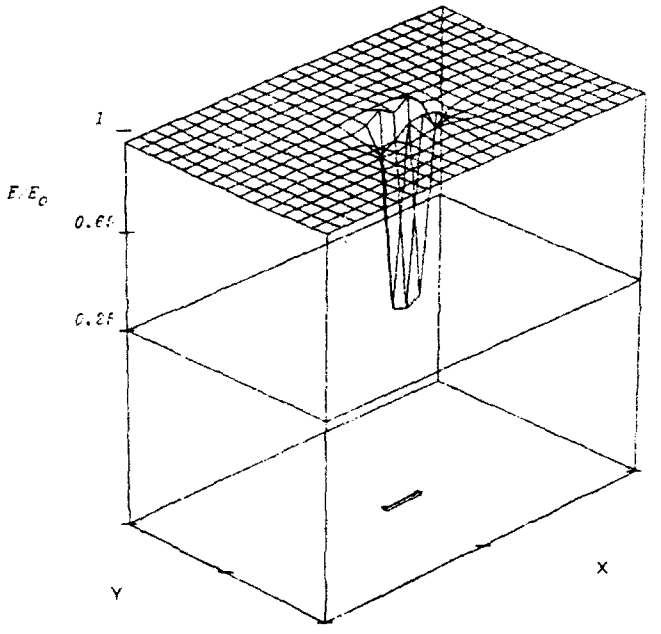

Figure 1.4: Electric field distribution away from the cavity

Calculation of the electric field distribution in the neighborhood of the cavity (Fig. 1.4) reveals that the perturbation of the field vanishes at a distance equivalent to half the cavity length away from the center. Furthermore, according to Fig. 1.5a which is a graph of the electric field intensity along the cavity, and Fig. 1.5b which depicts the field across the cavity, the field on the surface of the diaphragm is practically equivalent to E_0. However, inside the cavity it drops to zero, as a consequence of the Faraday-Cage effect. Inside the pyrex substrate the field has a value of about one fifth the magnitude of E_0, which is in good agreement with the fact that the permittivity in this medium is five times greater than that of air.

*Although the problem entails a 3-D object, it is possible to reduce it to the 2-D case due to the rotational symmetry of the circular cavity.

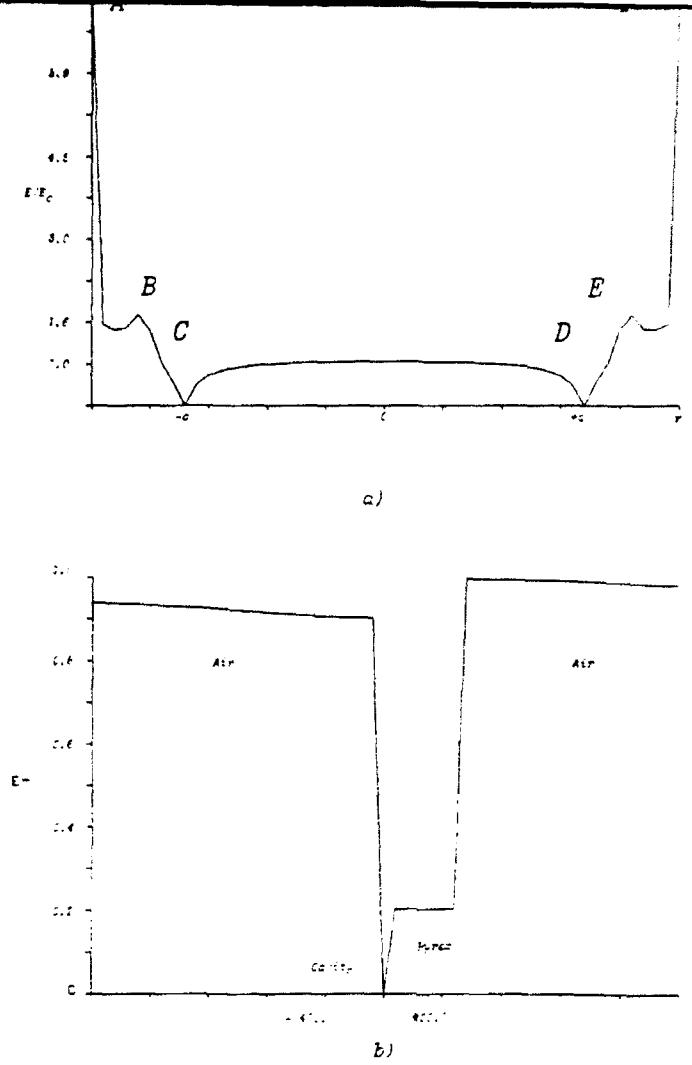

Figure 1.5: Electric field intensity, a) along the cavity and, b) across the cavity

Another important aspect is the variation of the electric field at the surface (E_{surf}). As seen from Fig. 1.5a, the field is practically uniform across the diaphragm, but increases sharply at cavity points A,B,E and F reaching values in excess of 10 times E_0. This is a result of the edge effects which give rise to a concentration of the field lines on the sharp edges or points of the cavity as illustrated in Figs. 1.6*a* and 1.6*b*. This problem is even more severe for values of α greater than zero, as the potential field distorts even more resulting in higher field intensities. Because of this non-uniform distribution of E_{surf}, the design of the diaphragm makes use of corrugations that allow only the deflection of the inner portion of the diaphragm, where E_{surf} is more uniform at $\alpha = 0$. The corrugations also help prevent any edge effects from producing any high magnitude forces on the diaphragm, due to the mechanical isolation between the diaphragm and the rest of the cavity.

In addition, to minimize the edge-effects of the cavity, a curved glass cap is used to protect and cover the entire probe. The dielectric sheath helps to reduce the high fields introduced by the sharp corner, by smoothing the field lines around the probe as seen from Figs. 1.7*a* and 1.7*b* (for $\alpha = 0$), where no high fields are present on the outside of the probe and yet, E_{surf} on the diaphragm remains practically unaffected.

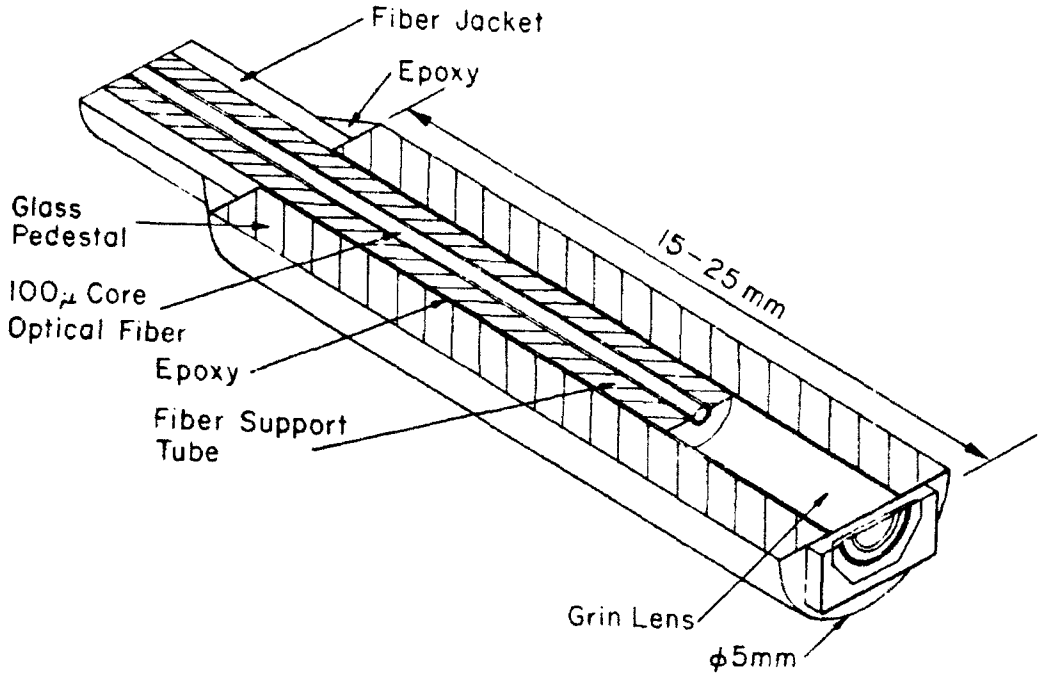

Figure 1.2: Mounting of sensor cavity on an optical fiber

and for the case of sinusoidal corrugations:

$$q = \sqrt{1 + 1.5\frac{H^2}{t^2}} \tag{5}$$

where P is the differential pressure, a the membrane radius, r the boss to diaphragm radius ratio, $E' = E \setminus (1 - \nu^2)$ is the plate modulus of elasticity, t the thickness, H the corrugation depth and q the corrugation quality factor.

Since the cavity is formed by a highly-doped silicon well and a metallic film, both good conducting materials at low frequencies, the structure acts as an ultra thin faraday cage, the interior of which contains no electric fields. Thus, a net electrostatic force will be exerted on the top surface of the silicon diaphragm when exposed to an external electric field. As the gap in the cavity increases, under the influence of the negative electrostatic pressure induced by the field, the intensity of the backreflected light into the fiber changes accordingly. Hence, the reflected light spectrum associated with the cavity shifts to longer wavelengths for increasing magnitudes of electric field. The spectral shift of the interferometer peak can be interrogated using an LED, which translates the cavity's spectral shifts into intensity variations of the LED output spectrum thus yielding a spectrally modulated envelope. These intensity changes are subsequently detected and processed to linearize the sensor's response.

To make the sensor immune to variations in light intensity due to bendi:g or transmission losses, as well as any possible degradation of the light source, a dual-wavelength referencing technique is used (see Fig. 1.3). Light from an LED source is launched into the multimode fiber and coupled into the cavity by the GRIN lens. Inside the cavity, each wavelength experiences a different amount of reflection due to the spectral dependence characteristics of the Fabry-Perot. The backreflected light is then split in two beams by means of an optical fiber coupler. Specific wavelengths are selected out of the LED's broad spectrum by narrow bandpass optical filters, and their intensities measured using optical detectors.

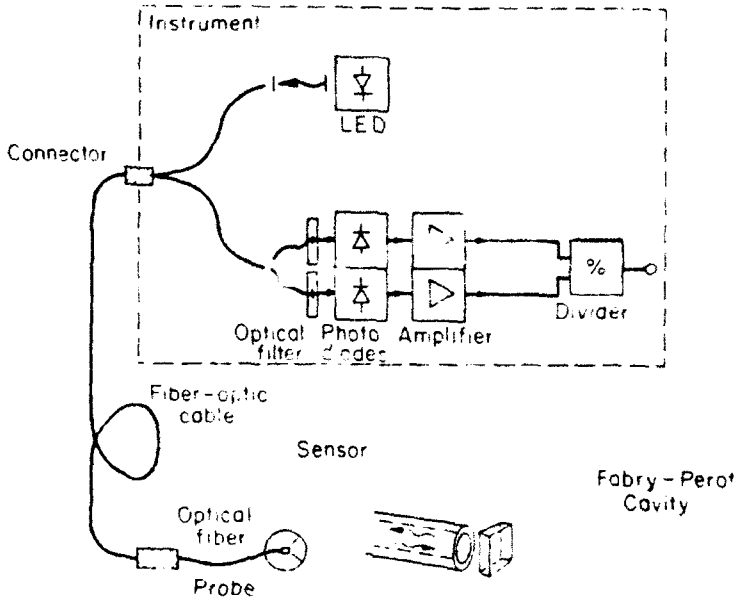

Figure 1.3: Sensor system schematic

In this fashion, the magnitude of the electric field is related to a change in the intensity ratio at these two wavelengths, with the added advantage that the reading obtained will be independent of any transmission losses since both signals undergo the same effects along their path. With careful design of cavity and diaphragm, it is possible to have a linear, monotonic, variation in intensity ratio over a given field range.

We are clearly measuring only one component of the vector electric field, however, either by reorientation of the probe, or by simultaneous probes mounted close to one another in orthogonal directions, all components of the vector field could be measured with a high degree of spatial resolution. As a consequence of the small size of the probe and the fact that there is little conducting material to perturb the electric field, it would be possible to have two or more probes a small distance apart to make simultaneous measurements.

Since the cavity chamber possesses vent holes that communicate to the surrounding environment, there will no net differential pressure acting on the membrane. Furthermore, because the sensor is protected by a glass cap, it is possible to be used in harsh environments such as that present in an oil-filled transformer.

PRINCIPLE OF OPERATION

There are 3 fundamental mechanisms for the measurement of electric fields: electrostatic induction, electrophysical phenomena (such as the pockels and the piezoelectric effects) and electrostatic forces. Methods based on electrostatic induction rely on the accurate measurement of the current resulting from the time variation of the charges induced on a metallic body immersed in a field, and thus are not suitable for use with fiber optics. Sensors based on electro-optic effects are usually bulky and suffer from detrimental temperature effects. Electrostatic force effects, on the other hand, are more amenable to be used with optical fibers and, although they go as the square of the electric field, they can be effectively used in schemes where adequate linearization is possible. Thus we have based our design on them.

Whenever a conductor is placed into an electric field, the free electrons in the material rearrange themselves in such a way as to render its interior field-free. This electron arrangement gives place to an induced charge on the surface of the conductor. However, the net charge in the body remains zero. The Coloumbic attraction between the induced charge and the external electric field, E, develops an electrostatic force density, f_s, acting normal to the surface of the conductor, for otherwise the charges would move along the surface, contradicting the assumption of an equipotential surface. Since the magnitude of f_s is given by $f_s = \frac{1}{2}\epsilon_0 E^2$, then its direction is always pointing away from the surface, regardless of the sign of the field. Such forces are very weak, and when acting on objects exert negative pressures of the order of a few pascals.

By combining the concept of a Faraday cage with an optical interferometer it is possible to measure this low pressure. The transmissivity (or reflectivity) of a Fabry-Perot cavity is extremely sensitive to changes in the length of the cavity, which in this case is caused by a pressure differential acting upon a movable mirror arrangement at one end of the cavity. A thin deformable diaphragm with provisions to reflect light can serve this purpose. Flat silicon diaphragms have been successfully used in the past as pressure transducers. These flat diaphragms, however, exhibit non-linear behavior for small thicknesses and uneven deflection across their radius. These problems can be corrected by the introduction of corrugations in the plane of the diaphragm which linearize its response making it move in a piston-like fashion.

As mentioned before, the proposed sensor is based on a variable gap, Fabry-Perot micro-cavity mounted on the end of an optical fiber. Fig. 1.1 depicts the Fabry-Perot cavity (FPC) design which is formed by a suspended, thin and corrugated silicon diaphragm bonded to a glass substrate. A metallic film on the surface of the silicon diaphragm acts as one of the cavity mirrors, while a thin, partially transmitting, aluminum film on the substrate acts as the other. This structure is then mounted on the tip of a 100/140 μm multimode optical fiber onto which a GRIN lens has been previously attached, as illustrated in Fig. 1.2. In this manner, light traveling in the core of the fiber will be collimated into the cavity, and the back-reflected light will be re-launched into the optical fiber.

The reflectance of a Fabry-Perot will be a function of spacing, index of refraction, mirror reflectivities and wavelength. Assuming that the mirrors are lossless, the reflected intensity is given as

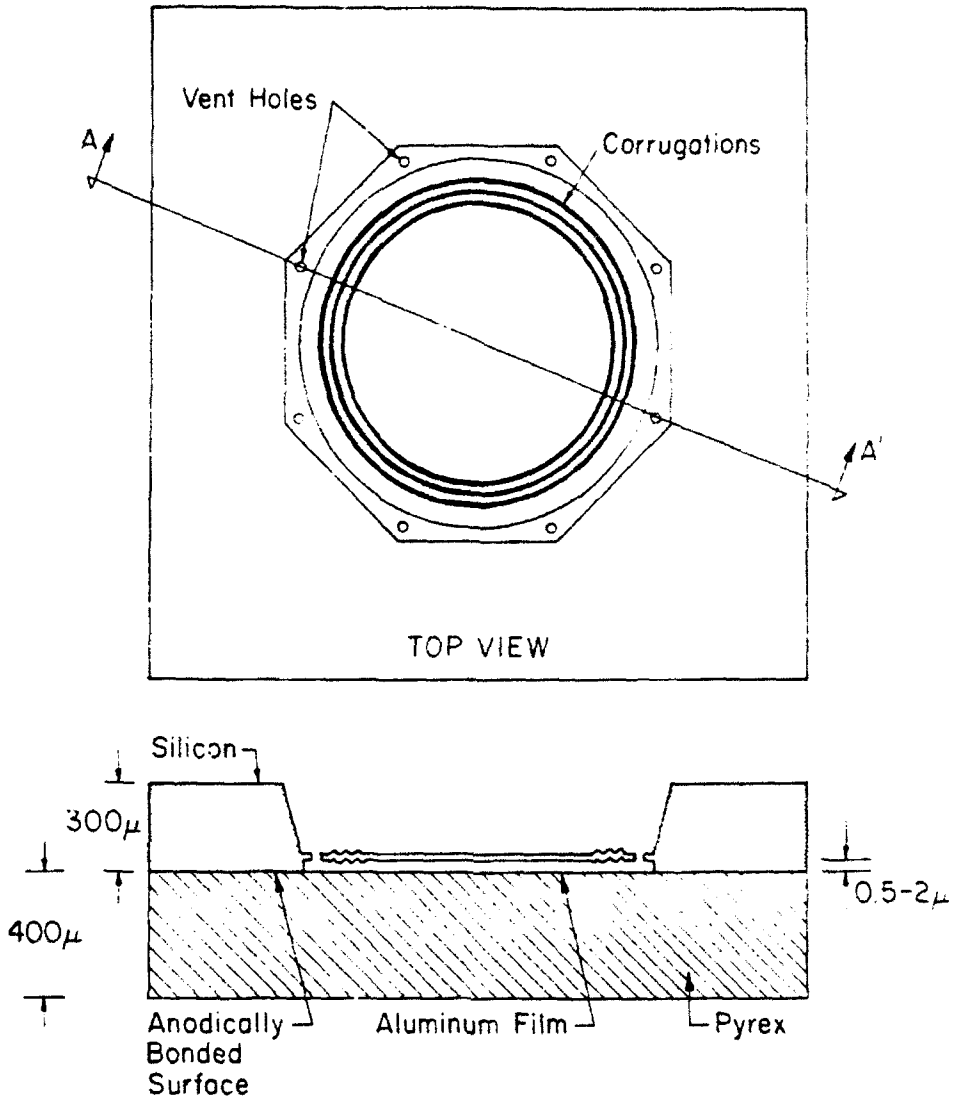

Figure 1.1: Fabry-Perot microcavity a) top-view, and b) cross-section

the following[8]:

$$\frac{I_r}{I_o} = \frac{4\sqrt{R_1R_2}sin^2(\frac{2\pi h}{\lambda})}{(1-\sqrt{R_1R_2})^2 + 4\sqrt{R_1R_2}sin^2(\frac{2\pi h}{\lambda})} \tag{1}$$

with

$$h = h_o + \delta h \tag{2}$$

where R_1 and R_2 are the mirror reflectivities, h_o is the height of the unperturbed cavity, and δh is the deflection of a bossed, corrugated membrane given by the expression[9]:

$$\delta h = \frac{\epsilon 3Pa^4}{16E't^3} \tag{3}$$

where

$$\epsilon = \frac{8(1-r^4)}{(q+3)(q+1)}\left(1 - \frac{8qr^4(1-r^{q-1})(1-r^{q-3})}{(q-1)(q-3)(1-r^4)(1-r^{2q})}\right) \tag{4}$$

PRELIMINARY RESULTS

To determine the performance of the sensor under the effects of an external electric field, measurements of the reflected intensity were made for a probe placed inside and electric-field test cage especially built for this purpose. The test cage consists of two parallel metallic plates separated by dielectric rods. The assembly was supported $1m$ above the ground and placed at least one meter away from any conducting surfaces. The plates were connected to the terminals of a $30KV$ DC power supply. In addition, sharp edges and corners were coated to prevent any possible corona effects. With this arrangement it was possible to generate uniform DC electric fields in the 0 to $300KV/m$ range.

Measurements made with probes under DC fields of up to $300KV/m$ showed no signs of electric discharge or corona effects. Reflected intensity measurements for different intensities of applied electric field were obtained using an arrangement similar to the one depicted in Fig. 1.3. Light from a white-light source is launched into one arm of a fused fiber coupler connected to the fiber probe, and the reflected light from the cavity is measured through the opposite arm of the fiber coupler by means of an optical spectrum analyzer. Fig. 1.11 shows the spectra for the reflected intensity with no field applied and with a field of $300KV/m$. Notice that the spectral shift in the resonance signature is towards longer wavelengths, which indicates that the cavity spacing is increasing as a function of field intensity as expected.

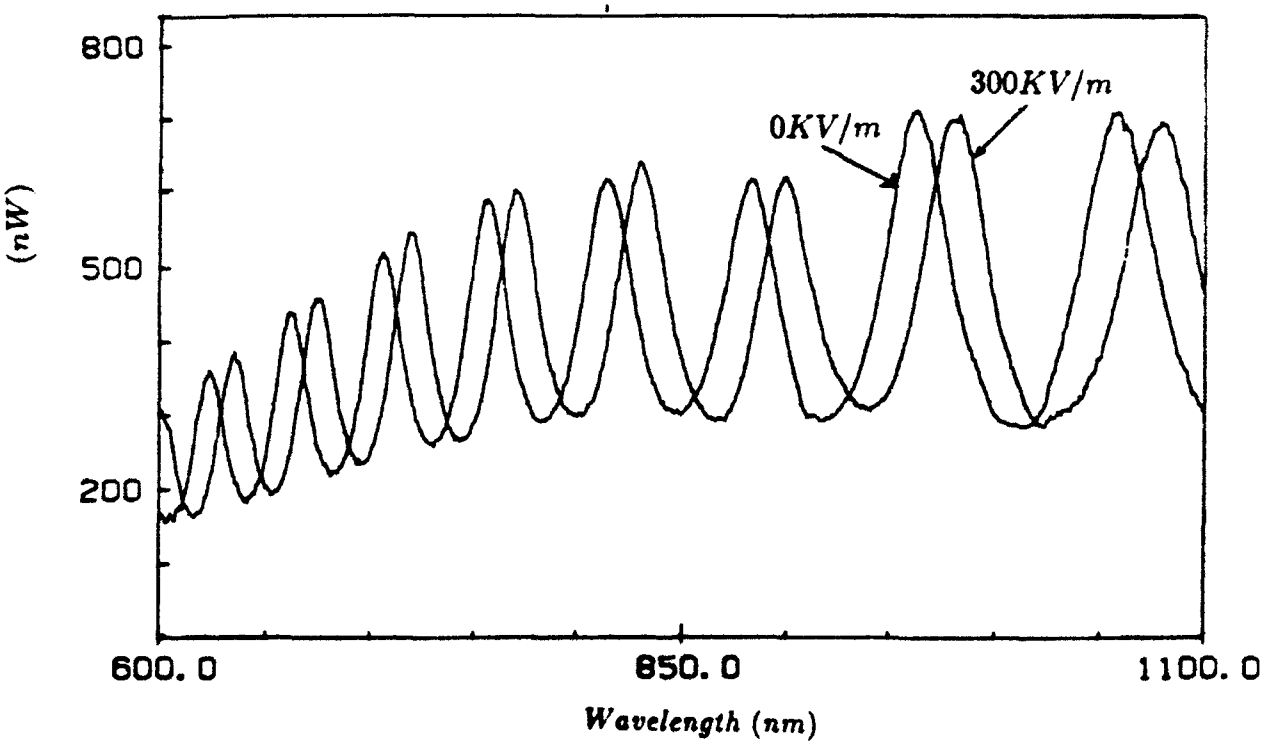

Figure 1.10: Reflected intensity with no field and with a field of $300KV/m$

The operation of the sensor was determined using an LED emitting at $850nm$ source instead of white light. Measured spectra at different applied field intensities are shown in Fig. 1.12. Notice

again that the cavity's diaphragm does indeed deflect under the influence of the external field and that this deflection brings upon a change in the reflected spectrum of the LED. As expected, the relative intensity changes of the detected power increase as the square of the electric field. Furthermore, $40KV/m$ was the minimum field for which a deflection was observed. This is attributed to the residual stress present in the diaphragm due to the heavy boron-doping used in its fabrication. Diaphragms fabricated using a stress-free process such as the electrochemical etching process, will result in sensors with increased sensitivity.

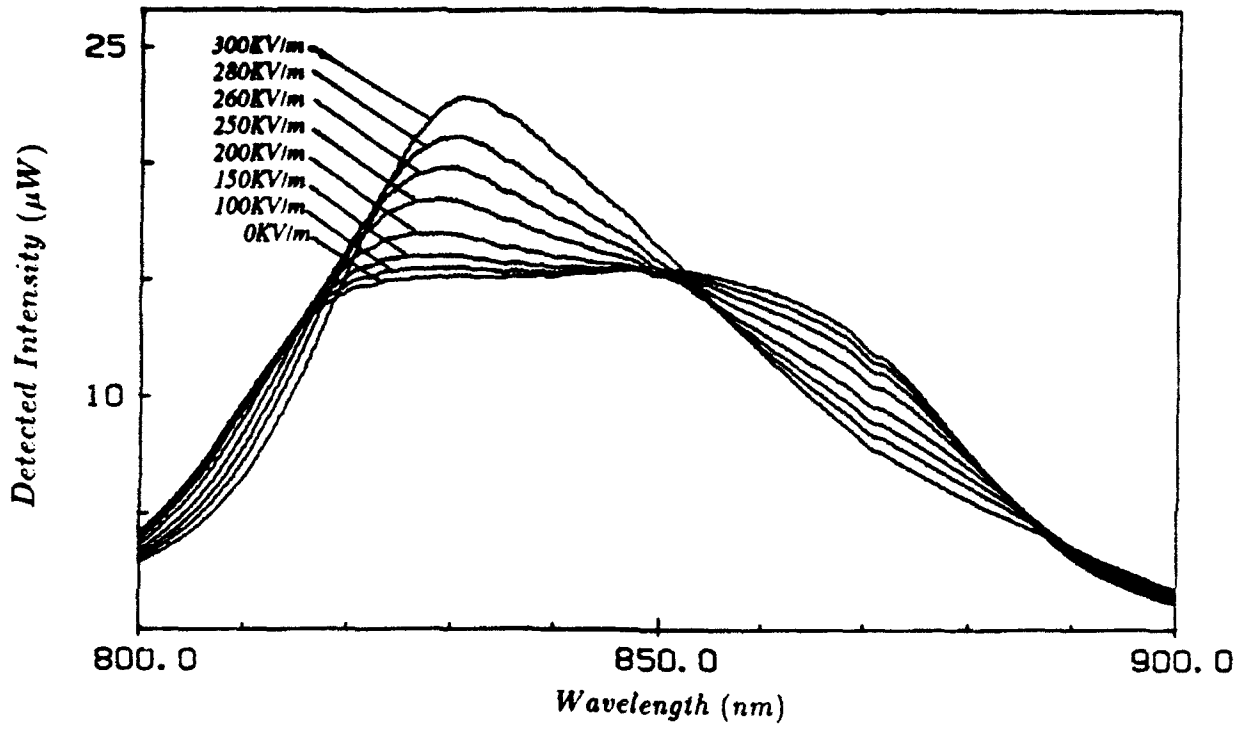

Figure 1.11: Measured reflected spectrum for different intensities of electric field.

CONCLUSIONS

A novel electric field sensor using a combination of Faraday cage and a micro Fabry-Perot interferometer mounted on the tip of an optical fiber has been demonstrated.

Electric fields in the range of 0 to $300KV/m$ were successfully measured. The minimum intensity detected was of the order of $40KV/m$. This relatively low sensitivity is due to the high stiffness of the diaphragm arising from the high boron-diffusion and the increased thickness of $3.5\mu m$ of the fabricated diaphragms, as opposed to the design value of $2\mu m$. However, higher sensitivities are possible by thinning the diaphragm, increasing the radius, reducing the boss ratio or decreasing the corrugation depth.

No corona or discharge effects were observed in the course of the field tests, and repeatable results were obtained in almost all cases, except for a few occasions for which the damping effects altered the response of the sensor.

ACKNOWLEDGEMENTS

This work was supported by the Electric Power Research Institute, Palo Alto, CA, under grant RP-8004-05.

The authors wish to thank Mr. Jan Stein, contract monitor for EPRI, for all his support and kind assistance throughout the entire project, as well as Dr. Dino Ciarlo of Lawrence Livermore National Labs for the fabrication of the silicon diaphragms used in this work and Prof. Bill Patterson for numerous helpful discussions.

REFERENCES

1. DonVito, P.A., "Estimates of the Costs of Measurements in the U.S. Economy", Nat. Bur. Stand., Planning Report 21, 1984.

2. Carstensen, E. L., *Biological Effects of Transmission Line Fields*, Elsevier, 1987.

3. Fitzgerald, K., Morgan, G., and Nair, I., "Electromagnetic Fields: The Jury's Still Out", IEEE Spectrum, August 1990, pp. 22-35.

4. Erikson, D.C., "The Use of Fiber Optics for Communications, Measurement and Control within High Voltage Substations", IEEE Trans. Pwr. App. Sys., Vol. PAS-99 No. 3, pp. 1057-1063, 1980.

5. Kirkham, H., Jonhston, A., Lutes, G., Daud, T. and Hyland, S., "Power System Applications of Fiber Optics", Jet Propulsion Laboratory Report # 84-28, Pasadena, CA, 1984.

6. Tenesse Valley Authority, "Research Planning Study of Fiber Optic Sensors", Electric Power Research Institute final report # ER-6428, 1989.

7. Boutacoff, D., "Optical Sensing for Power Plants", EPRI Journal, September 1990, pp. 14-21.

8. Born, M. and Wolf, E., *Principles of Optics*, Pergamon Press, New York, 1984.

9. Haringx, J. A., "The Rigidity of Corrugated Diaphragms", Appl. Sci. Res., Vol. A2, pp. 299-325, 1950.

10. ELECTRO is a Copyright of Integrated Engineering Software Inc., Winnipeg, Manitoba, Canada R3B 1Y6.

11. Wallis, G. and Pomerantz, D. I., "Field Assisted Glass-Metal Sealing", J. Appl. Phys., Vol. 40, No. 10, pp. 3946-3949, 1969.

Temperature Dependence of Effective Cutoff Wavelength in Depressed Clad Single Mode Fibers

Q. Zhang, T. F. Morse, L. Reinhart, A. Kilian
Laboratory for Lightwave Technology, Division of Engineering
Brown University, Providence, R.I. 02912

Abstract

The effective cutoff wavelength is known to be dependent on fiber length, bending radius and fiber connections. In this paper we show that the effective cutoff wavelength is also temperature dependent in depressed clad single mode fibers. The annealing condition which affects the results is discussed. A theoretical model based on residual stress remaining in the fiber during the drawing process is proposed to explain the experimental observation. The temperature dependence of the effective cutoff wavelength in matched clad fiber is also presented for comparison.

Introduction

Cutoff wavelength is defined as the wavelength at which the LP_{11} mode index equals the cladding refractive index. It is a very important parameter since the fiber becomes single mode beyond the cutoff wavelength. The theoretical cutoff wavelength is determined from the refractive index profile. In a practical situation, the cutoff wavelength is difficult to measure because it depends on fiber length [1], bending radius[2-5] and fiber coupling. Therefore, we experimentally determine an effective cutoff wavelength λ_c. The effective cutoff wavelength[6] is determined by the intersection of the slope of the portion of the power curve that decays near the cutoff region, and the slope of the single mode power in a transmission spectrum. While the effective cutoff wavelength dependence on bending has been investigated extensively, its dependence on temperature has not been well examined.

In this paper, we report our observation of temperature dependence of the effective cutoff wavelength in depressed clad single mode fibers. A linear temperature dependence was observed from room temperature to 300 °C. Anomalous phenomena were observed at temperatures greater than 400 °C. The coating affected the results in the region between 300-500 °C, and thermal annealing effects were observed at temperature greater than 700 °C. Annealing permanently shifted the effective cutoff wavelength to a much shorter wavelength. Since the effective cutoff wavelength is correlated with the refractive index profile, it is necessary to investigate the refractive index profile change as a function of annealing conditions. Similar experiments were also performed in matched-clad (step-index) single mode fibers for comparison.

Experiments

Two sets of experiments were performed. The first measured λ_c *in situ* as a function of temperature. We used a 6 m length of fiber of which 4 m were coiled with a diameter of 9.5 cm and the remaining was used

as a pigtail to a light source and a detector. The fiber coil was then placed into a precisely controlled single zone furnace. The second set of experiments consisted of 10 cm length of bare straight fiber to measure the refractive index profile change for different annealing conditions. Both fiber samples were baked at the same time to ensure the same thermal history and annealing condition. The experiments were performed using four different kinds of fibers:

Fiber A had a B_2O_3 (10 mol %) suppressed inner-cladding. The core was doped with 2 mol % of Al_2O_3 and 200 ppm Eu. It was single mode at 780 nm for a straight fiber arrangement.

Fiber B had an SF_6 suppressed inner-cladding with pure silica core. It was slightly multi-mode. Fibers were drawn from the same preform at different tensions. The low-tension fiber was drawn at 15g and the high-tension fiber at 120g.

Fiber C was a matched-clad single mode fiber highly doped with Nd^{3+} (2000 ppm). The cladding was pure SiO_2. The fiber was drawn at 30g. It was single mode at 1170 nm.

Fiber D was also a matched-clad single mode fiber. Its core was doped with 8 mol % GeO_2. The cladding was pure SiO_2. The fiber was drawn at 60g. It was single mode at 960 nm.

For the transmission spectrum measurements, an Anritsu MG922A white light source and an Ando AQ6312B optical spectrum analyzer were used. The refractive index profile was measured by the refracted near-field pattern method at 632.8 nm using York FCM1000.

Results and Discussion

1. Cutoff wavelength and temperature for fiber A.

The transmission spectra near the cutoff region for fiber A is shown for different temperatures in Fig. 1. This temperature dependence can be divided into three categories: 1. linear red-shift of λ_c between 20 - 300°C; 2. anomalous red-shift between 400 - 700°C; 3. a large annealing induced blue-shift of λ_c from 700°C and above. Categories 1 and 2 are shown in Fig. 1 (a), and category 3, in Fig.1 (b). The coating material Desotech 095-044 began to degrade at 80 °C. The theoretical prediction of λ_c shifts as results of linear thermal expansion is [13]:

$$\lambda_c = \frac{2\pi a}{V_c}\sqrt{(n_1+\Delta n_1)^2-(n_2+\Delta n_2)^2} \tag{1}$$

with[16]

$$\begin{aligned}\Delta n_1 &= \frac{1}{2}(C_1+C_2)\left[b^2\left(\frac{1}{b^2}-\frac{1}{c^2}\right)\alpha_2+\alpha_1\right]\frac{E\Delta T}{1-\nu^2}\\ \Delta n_2 &= -\frac{1}{2}\left[(C_1+C_2)b^2\left(\frac{1}{b^2}-\frac{1}{c^2}\right)\alpha_2+\frac{a^2}{c^2}(C_1+C_2)\alpha_1+\frac{a^2}{r^2}(C_2-C_1)\alpha_1\right]\frac{E\Delta T}{1-\nu^2}\end{aligned} \tag{2}$$

where $V_c = 2.405$. The radii of the core, inner-cladding and outer-cladding are a, b, and c , respectively, C_1 and C_2 are the photoelastic coefficients. The thermal expansion coefficients of the core and inner-cladding are α_i $(i = 1,2)$. n_i $(i = 1,2)$ are the refractive indices. Young's modulus is E and ν Poisson's ratio. The temperature difference with respect to room temperature is ΔT. The calculated results from Eq. (1) are shown in Fig. 2 together with the experimental data. They show good agreement between 20 and 700°C despite the anomalous behavior caused by modal noise and coating burning at above 500°C. After

the coating was completely burned off, the fiber was heated up to 1000°C. The observed anomalous modal noise at 400 °C and 700 °C indicates that coating has an influence on modal interference in this bent configuration. Recently, there have been reports on the anomalous structure of modal cutoff induced by bending and different lengths of fiber[2,3,4] in depressed clad single mode fibers. Shah[3], Sudbo and Nesset[4] reported that the anomalous effect was due to coupling or interference between the fundamental mode in the core and modes in the cladding, called "whispering gallery" modes. Jacobs and Peckham[2] argued that the finite cladding and coating model was more reasonable in explaining the observed anomalous phenomena. Our results seem to support Jacobs' model.

2. Refractive index and annealing conditions.

When a fiber is drawn from a preform, the frozen-in residual stress could change the refractive index by approximately 10^{-3}.[7,9] The residual stress frozen into the fiber during the drawing process results from a superposition of thermal and mechanical stress.[8,10] Thermal stress is caused by thermal expansion differences between the core and cladding, and the mechanical stress results from tension on the fiber during pulling. Annealing releases these stresses. It will tend to change the refractive index back to that found in a stress-free state. Therefore, it is expected that annealing will have a more pronounced effects on the fiber with higher residual stress, i.e. drawn at high tension. This was observed experimentally. Also, the glass softening temperature usually decreases as the dopant concentration in the fiber increases. The annealing temperature varies for different fibers depending on different glass softening temperature, thus different annealing temperatures show different degrees of stress relief.

2.1 Mechanical Model.[11,14]

A simple mechanical model is developed to aid in understanding the annealing effects on residual stress for various types of fibers. The subscripts 1, 2, 3 represent core, inner-cladding, and outer-cladding. Because the inner-cladding was slightly more doped than that in the core, the glass transition temperature T_i ($i = 1,2,3$) of each layer satisfies: $T_2 < T_1 < T_3$. Thus, the fiber becomes solid in three stages. Using the simple model that below the glass transition temperature T_i, the glass is solid and stressed, and above this temperature it is stress free, we found that at each stage the stress σ and strain ε can be expressed as follows, where superscripts refer to temperatures $(1,2,3,r)$ and subscripts refer to regions in the fiber $(1,2,3)$.

$$\sigma_3^3 = \frac{F}{A_3}, \qquad \varepsilon_3^3 = \frac{F}{E_3 A_3} + \alpha_3 T_3 \qquad (\text{at } T_3) \tag{3}$$

$$\begin{cases} \sigma_3^1 = \dfrac{F}{A_3}, & \varepsilon_3^1 = \dfrac{F}{E_3 A_3} + \alpha_3 T_1 \\ \sigma_1^1 = 0, & \varepsilon_1^1 = \alpha_1 T_1 \end{cases} \qquad (\text{at } T_1) \tag{4}$$

$$\begin{cases} \sigma_3^2 = \dfrac{F_3^2}{A_3}, & \varepsilon_3^2 = \dfrac{F_3^2}{E_3 A_3} + \alpha_3 T_2 \\ \sigma_1^2 = \dfrac{F_1^2}{A_1}, & \varepsilon_1^2 = \dfrac{F_1^2}{E_1 A_1} + \alpha_1 T_2 \\ \sigma_2^2 = 0, & \varepsilon_2^2 = \alpha_2 T_2 \end{cases} \qquad (\text{at } T_2) \tag{5}$$

where A_i ($i = 1,2,3$) are the area of each fiber layers. Eventually, the fiber reaches room temperature where the stresses and strains are given as follows:

$$\begin{aligned} \sigma_3^r &= \frac{F_3^r}{A_3}, \qquad \varepsilon_3^r = \frac{F_3^r}{A_3 E_3} \\ \sigma_1^r &= \frac{F_1^r}{A_1}, \qquad \varepsilon_1^r = \frac{F_1^r}{A_1 E_1} \\ \sigma_2^r &= \frac{F_2^r}{A_2}, \qquad \varepsilon_2^r = \frac{F_2^r}{A_2 E_2} \end{aligned} \tag{6}$$

Because the strain rate and actual forces in the core and claddings must be equal, we have

$$\begin{aligned} \varepsilon_3^1 - \varepsilon_3^2 &= \varepsilon_1^1 - \varepsilon_1^2 \\ \varepsilon_3^r - \varepsilon_3^2 &= \varepsilon_1^r - \varepsilon_1^2 = \varepsilon_2^r - \varepsilon_2^2 \\ F_1^2 + F_3^2 &= F \\ F_1^r + F_2^r + F_3^r &= F \end{aligned} \tag{7}$$

Finally, when the pulling tension is released, that is equivalent to applying a negative pulling force F to compress the fiber. The strain rate and the total force remain constants:

$$\begin{aligned} F_1^f + F_2^f + F_3^f &= F \\ \frac{F_1^f}{E_1 A_1} &= \frac{F_2^f}{E_2 A_2} = \frac{F_3^f}{E_3 A_3} \end{aligned} \tag{8}$$

Hence the total residual stress remaining in the fiber are:

$$\begin{aligned} \sigma_1^t &= \sigma_1^r - \frac{F_1^f}{A_1} \\ \sigma_2^t &= \sigma_2^r - \frac{F_2^f}{A_2} \end{aligned} \tag{9}$$

Solving Eqs. (3)-(9) gives the expressions for the residual stress in the core and inner-cladding:

$$\begin{aligned} \sigma_1^t &= \frac{(\alpha_1 - \alpha_3)(T_1 - T_2) A_3 E_1 E_3}{A_1 E_1 + A_3 E_3} + \frac{[(\alpha_1 - \alpha_3) A_3 E_3 + (\alpha_1 - \alpha_2) A_2 E_2] T_2 E_1 - F E_1}{A_1 E_1 + A_2 E_2 + A_3 E_3} \\ \sigma_2^t &= \frac{[(\alpha_1 - \alpha_3) A_3 E_3 + (\alpha_2 - \alpha_1)(A_1 E_1 + A_3 E_3)] T_2 E_2 - F E_2}{A_1 E_1 + A_2 E_2 + A_3 E_3} \end{aligned} \tag{10}$$

The refractive index change induced by stress is [7]:

$$\Delta n_i = -C_2 \sigma_i^t \qquad (i = 1, 2) \tag{11}$$

In Eq. (11), the photoelastic coefficient C_2 equals $4.2 \times 10^{-12} \mathrm{Pa}^{-1}$ for SiO_2. In slightly doped glass, this coefficient is approximately the same. Δn_i takes the positive value for the compression σ_i^t.

2.2 Experimental Measurement

For fiber A, Fig. 3 shows the refractive index profile changes for different annealing temperatures. Upon annealing, the refractive index increased in the inner-cladding and decreased in the core. This is in agreement with equations 10. This dependence on the annealing temperature indicates that the stress relief depends on the "softenness" of the glass. In the present fiber, the softening temperature at which stress-release began in the inner-cladding was about 700 °C and 800 °C in the core. The refractive index change in the core after annealing at 800 °C was 5×10^{-4}, and in the inner-cladding 1×10^{-3}, as shown in Fig. 3. The calculated

stresses from Eq.(10) in the inner-cladding and core, with $\alpha_1 \approx \alpha_3 = 5 \times 10^{-7}\ ^\circ C^{-1}$, $\alpha_2 = 9 \times 10^{-7}\ ^\circ C^{-1}$, are: $\sigma_1^i = -0.7$ MPa, $\sigma_2^i = 24.3$ MPa. The pulling force was not recorded for this fiber, but it was believed about 5g. The stress in the core is negative, i.e. compression, and there is tension in the the inner-cladding which agrees with the experimental observations. The index changes $\Delta n_1 = 3.0 \times 10^{-5}$, $\Delta n_2 = -1.0 \times 10^{-4}$. The calculated values are smaller than the experimentally measured ones.

For fiber B, Fig. 4 shows the refractive index profiles of a fiber pulled at low-tension and high-tension before and after annealing. Both fibers were baked at 1000°C for 10 minutes. The refractive index profiles for both fibers became identical after annealing. The lack of index change in outer-cladding showed that the stress in the outer-cladding was always negligibly small. For the low-tension fiber, the annealing raised the index in the inner-cladding by approximately 10^{-4}. The calculated stresses form Eq.(10) in the inner-cladding and core, after taking $\alpha_1 \approx \alpha_3 = 5 \times 10^{-7}\ ^\circ C^{-1}$, $\alpha_2 = 4 \times 10^{-7}\ ^\circ C^{-1}$, are: $\sigma_1^i = 2.0 - F \times 0.82$ MPa, $\sigma_2^i = -5.1 - F \times 0.82$ MPa. $F = 15$g for the low-tension fiber, and both core and inner-cladding are under compression. Experimental results, however, show that the cladding refractive index increases upon annealing, indicating that the cladding was in tension. This disagreement with our simple model may well be due to a neglect of radial and circumferential stresses. For the high-tension fiber, both theory and experiment show that the core and inner-cladding were under compression. The magnitudes of compression estimated from Eq.(10) are $\sigma_1^i = -96$ MP a and $\sigma_2^i = -103$ MPa. The calculated index changes are $\Delta n_1 = 4.1 \times 10^{-4}$, $\Delta n_2 = 4.3 \times 10^{-4}$. They agree reasonably well with the experimental measurements.

3. Annealing effects in matched-clad fibers

Fibers C and D were drawn at 30 g and 60 g respectively. For fiber C, the residual stress in the core was compressive [8,11]. The fact that very little difference was seen after the first baking at 1000°C for 10 minutes suggests that the residual stress in fiber C was very small. This fiber was then annealed a second time at 1000°C for 10 minutes, resulting in an index decrease of 10^{-4}. This was calculated from the transmission spectra shown in Fig. 5. The estimated stress given by Eq.(11) was approximately 2×10^{-2} GPa. We also noticed that the water peak at 1390 nm increased after each baking. Fiber D was Ge doped and the Ge concentration was relatively low. The residual stress in this fiber core was tension. Hence the index should increase upon annealing. As shown by the transmission spectra in Fig. 6, the index calculated from these measurements increased by 3×10^{-4}. The estimated tension was about 7×10^{-2} GPa. All measurements shown in Figs. 5 and 6 were taken at room temperature.

Conclusions

The temperature dependence on the effective cutoff wavelength in a depressed clad single mode fiber has been reported. It includes three steps: 1. linear red shift between 20-300 °C; 2. anomalous red shift between 400-700 °C; 3. blue shift from 700 °C and above. The first two steps are due to thermal expansion mismatching between core and cladding. The last step is due to residual stress annealing. The annealing effect decreased the refractive index profile by 10^{-3} which is equivalent to a 160nm shift in the cutoff wavelength. We also found that the annealing effect is temperature dependent. However, for low tension, SiO_2 matched clad single mode fibers showed that the annealing effect is not that significant because the residual stress is an order of magnitude smaller.

Acknowledgements

We wish to thank Prof. K. S. Kim for helpful discussions. This work was supported by grants from the National Science Foundation (ECS-8916997), the US Air Force Office of Scientific Research (AFOSR-90-0062) and Material Science, Army Research Office Durham (DAAL03-91-G-0205).

References

1. Y. Murakami, A. Kawana and H. Isuchiya, "Cutoff wavelength measurement for single mode optical fibers", *Appl. Opt.*, vol. 18, p. 1101, 1979
2. S. A. Jacobs and D. W. Peckham, "The anomalous structure observed in single mode fiber cutoff wavelength measurements: Theory and solutions", *Technical Digest- Symposium on optical fiber measurements*, National Inst. Standard and Tech. Boulder, Colorado. 1990
3. V. Shah, "Curvature dependence of the effective cutoff wavelength in single-mode fibers", *J. Lightwave Technology*, vol. 5, no. 1, p. 35, 1987
4. A. S. Sudbo and E. Nesset, "Attenuation coefficient and effective cutoff wavelength of the LP_{11} modes in curved optical fibers", *J. Lightwave Technology*, vol. 7, no. 5, p. 785, 1989
5. K. A. H. van Leeuwen and H. T. Nijnius, "Measurement of higher-order mode attenuation in single mode fibers: effective cutoff wavelength", *Opt. Lett.*, vol. 9, no. 6, p. 252, 1984
6. D. L. Franzen, "Determining the effective cutoff wavelength of single-mode fibers: An interlaboratory comparison", *J. Lightwave Technology*, vol-3, no. 1, p. 128, 1985
7. Y. Hibino, F. Hanawa and M. Horiguchi, "Drawing-induced residual stress effects on optical characteristics in pure-silica-core single-mode fibers", *J. Appl. Phys.*, 65(1), p. 30, 1989
8. U. C. Paek and C. R. Kurkjian, "Calculation of cooling rate and induced stresses in drawing of optical fibers", *J. American Ceramic Society*, vol. 58, no. 7-8, p. 330, 1975
9. Y. Hibino, T. Edahiro, T. Horiguchi, Y. Azuma and N. Shibata, "Evaluation of residual stress and viscosity in SiO_2-core/F-SiO_2 clad single mode optical fibers from Brillouin gain spectra", *J. Appl. Phys.* vol. 66, no. 9, p. 4049, 1989
10. M. F. Yan, J. B. Macchesney, S. R. Nagel and W. W. Rhodes, "Sintering of optical wave-guide glasses", *J. Mater. Sci.*, vol. 15, p. 1371, 1980
11. U. C. Paek, R. B. Runk, "Physical behavior of the neck-down region during furnace drawing of silica fibers", *J. Appl. Phys.*, vol. 49, no .8, p. 4417, 1978
12. R. Ulrich, S. C. Rashleigh and W. Eickhoff, "Bending-induced birefringence in single mode fibers", *Opt. Lett.*, vol. 5, no. 6, p. 273, 1980
13. M. Monerie, "Propagation in doubly clad single mode fibers", *IEEE J. Quantum Electron.*, vol. 18, no. 4, p. 535, 1982
14. H. Wehr and D. Wiechert, "Refractive index and density of fluorine doped silica prepared by the PCVD process", *Mat. Res. Bull.*, vol. 21, no. 5, p. 559, 1986
15. N. P. Bansal and R. H. Doremus, *Handbook of glass properties*, Academic Press, 1986
16. Q. Zhang, T. F. Morse, L. Reinhart and A. Kilian, "New temperature-sensing approach based on temperature shift of effective cutoff wavelength", to be published in SPIE proceedings, OE/FIBER'92, Boston, MA. 1992

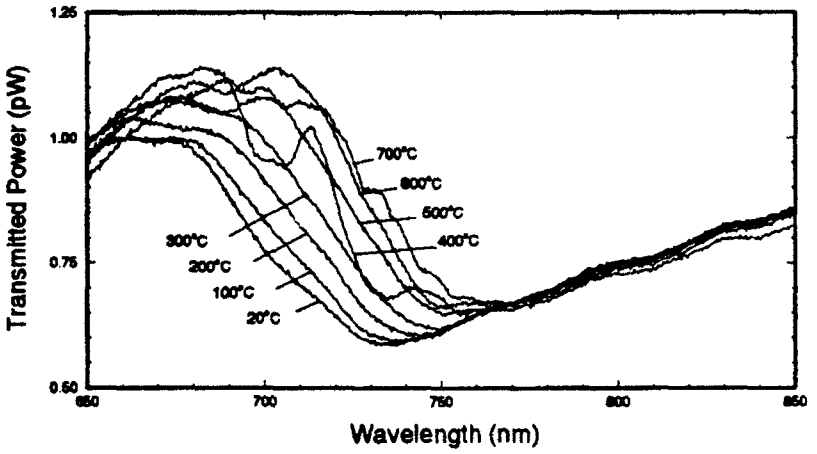

(a)

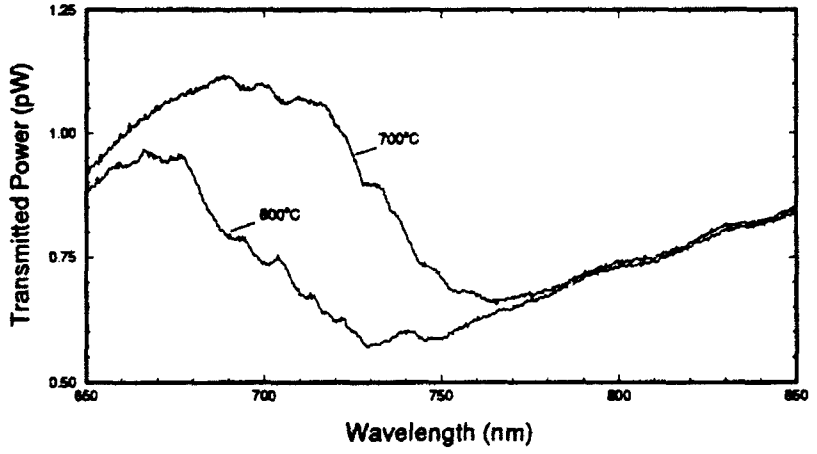

(b)

Fig.1 Transmission spectra of Fiber A near cutoff wavelength at different temperatures: (a) 20-700°C; (b) 700-800°C.

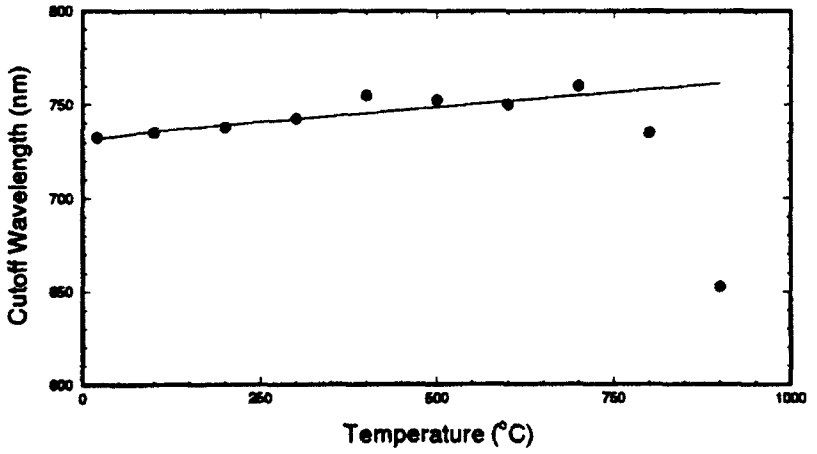

Fig.2 Cutoff wavelength shifts as a function of temperature.

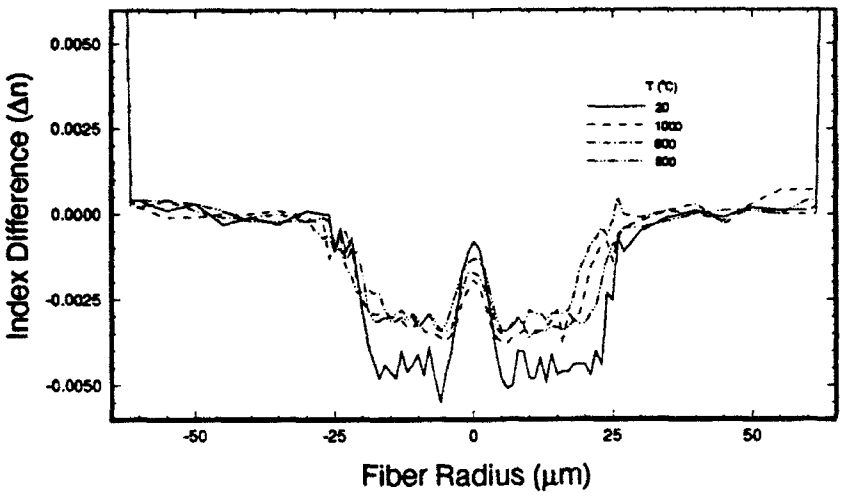

Fig.3 Refractive index profile of Fiber A due to different annealing temperatures.

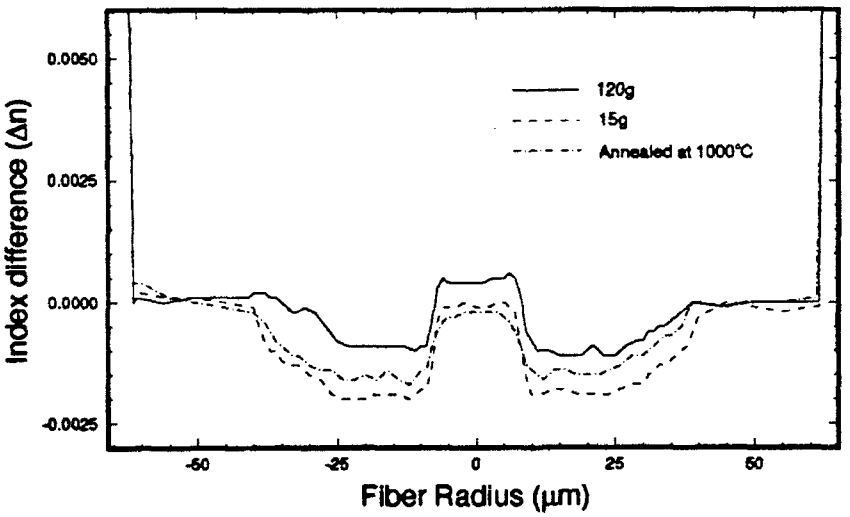

Fig.4 Refractive index profile of Fiber B drawn at low-tension and high-tension in comparison with that after annealing at 1000°C for 10 minutes.

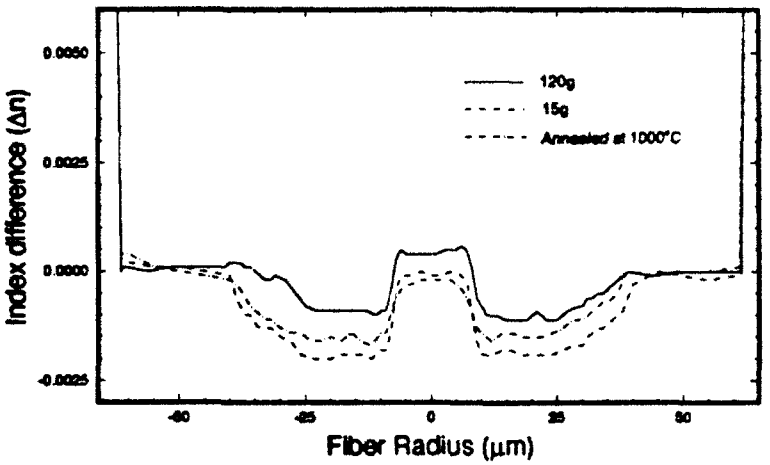

Fig.5 Refractive index profile of Fiber B drawn at low-tension and high-tension in comparison with that after annealing at 1000°C for 10 minute.

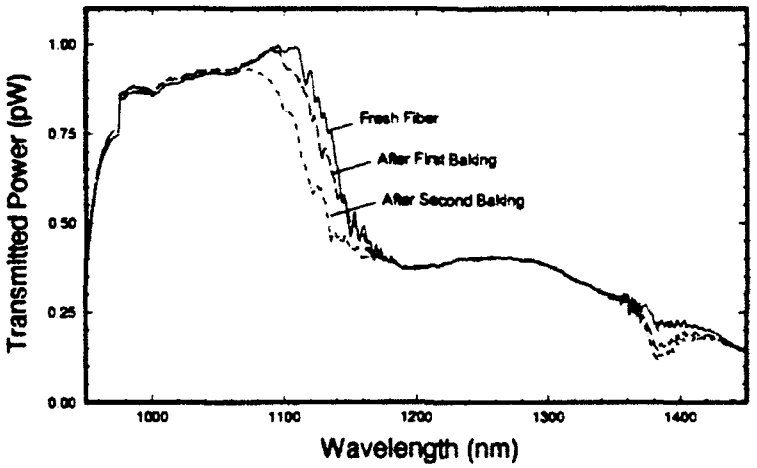

Fig.6 Shifts of transmission spectrum for Fiber C after baking at 1000°C for 30 minute.

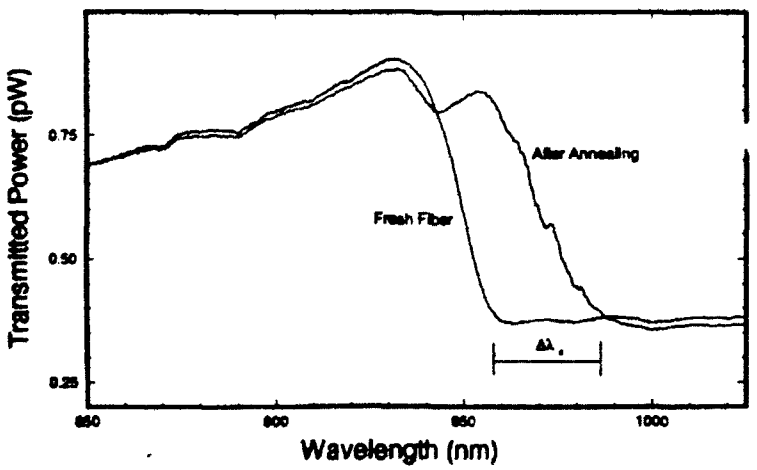

Fig.7 Shifts of transmission spectrum for Fiber D after annealing at 1000°C for 10 minute.

Proceedings
First International Conference on
Transport Phenomena in Processing
Edited by SELÇUK. İ. GÜÇERİ
March 22-26, 1992 Honolulu, HAWAII.

Reaction and Transport Kinetics during the Formation of Composite Materials by Chemical Vapor Infiltration

B. W. SHELDON, H.-C. CHANG AND T. F. MORSE

ABSTRACT

There are two important kinetic phenomena during isothermal chemical vapor infiltration: diffusion of the reactant gas into the preform and a deposition reaction that forms the matrix. The minimum infiltration time corresponds to the fastest deposition rate for which infiltration is relatively uniform. The criteria for achieving this optimum during the initial stage of isothermal CVI are considered with a relatively simple analysis based on the Thiele modulus, and with numerical solutions of the governing differential equations. These calculations make it possible to determine the optimum processing conditions for a given deposition chemistry and preform architecture.

INTRODUCTION

Chemical vapor infiltration (CVI) is an important method for producing ceramic and carbon matrix composites [1-4]. In this process, the matrix is formed by chemical vapor deposition (CVD) in the pore structure of a preform that typically consists of continuous carbon or ceramic fibers (i.e., the reinforcement phase). The most commonly used matrix material is SiC, however, any material that can be produced by CVD can, in theory, be used as a matrix. The preforms that are most commonly used for CVI are woven out of bundles (often called tows) of continuous fibers, such that the microstructure can be described on two different scales: the individual filaments that make up each bundle, and the individual bundles that are woven into the preform.

In isothermal CVI the precursor gases flow through the reactor and diffuse into a preform where they react to deposit the matrix. The infiltration kinetics are therefore controlled by diffusion and the deposition reaction. This process typically requires very long processing times, particularly for relatively thick composites. To reduce these times more sophisticated CVI techniques that utilize pressure and thermal gradients are currently being explored [3,4]. The primary processing objective of these CVI techniques is to achieve adequate infiltration in the shortest amount of time. As an example, the minimimization of the infiltration time during the initial stage of isothermal CVI is considered here, using both simple dimensionless analysis and numerical calculations.

Brian W. Sheldon, Han-Chieh Chang, and Theodore F. Morse, Division of Engineering, Brown University, Providence, RI 02912

MINIMIZING INFILTRATION TIMES

The preform structure that is described here consists of individual cloth layers (i.e., bundles) that are stacked together, as shown in Fig. 1. The bundles are treated as plates with a thickness of $2h$, in a preform of thickness $2H$. The initial stage is defined as the period when the individual bundles are infiltrated. This period ends when the bundles are overcoated such that further infiltration is not possible. With a constant deposition rate at the outer surface of a bundle, u_b, the initial stage ends at time t_i:

$$t_i = \frac{\theta_b r_f}{u_b} \tag{1}$$

where r_f is the fiber radius and θ_b is a parameter that depends on the fiber architecture.

The fiber bundles can be viewed as a set of randomly distributed, parallel cylinders, such that the initial surface area per unit volume in the bundles, S_{vob}, is:

$$S_{vob} = \frac{2(1-\varepsilon_{ob})}{r_f} \tag{2}$$

where ε_{ob} is the initial void fraction in a bundle. For this case, θ_b is given by [5]:

$$\theta_b(\varepsilon_{ob},\varepsilon_c) = -1 + \left[1 - \left(\frac{\varepsilon_{ob}}{1-\varepsilon_{ob}}\right)\ln\left(\frac{\varepsilon_c}{\varepsilon_{ob}}\right)\right]^{1/2} \tag{3}$$

where ε_c is the percolation threshold. Percolation limited diffusion is not considered here, and ε_c is set equal to 0.001.

The deposition rate was described as a first-order reaction. This assumption has also been used for other CVI modeling efforts [5-12]. The minimum infiltration time

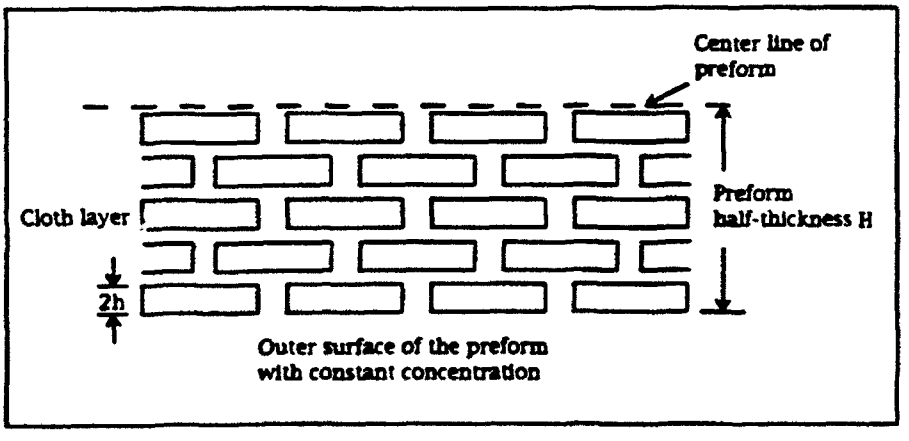

Figure 1. Schematic of the preform geometry that was used to model CVI. The shaded boxes represent fiber bundles, and the open regions between boxes represent porosity.

for a fiber bundle occurs at the fastest deposition rate where relatively uniform infiltration is possible. The maximum value can be estimated by considering the Thiele modulus, ϕ, which is commonly used to describe diffusion and reaction in porous materials [13,14]. During CVI ϕ varies with time, and, in most cases, with position in the sample. An isothermal, isobaric system can still be characterized with an initial value, ϕ_o. The infiltration of individual bundles has been analyzed with this approach, using a first-order deposition reaction that results in the following expression for ϕ_o [5]:

$$\phi_o^2 = \frac{(RT)\, u_b S_{vob}}{P_r V_s} \frac{(2h)^2}{D_{eob}} \tag{4}$$

where V_s is the molar volume of the deposited solid, T is the absolute temperature, and P_r is the reactant partial pressure at the external surface of the bundle or the preform. In general, the initial effective diffusivity, D_{eo}, is given by:

$$D_{eo} = \frac{\varepsilon_o}{\tau_o}\left[\frac{1}{D_M} + \frac{1}{D_K}\right]^{-1} \tag{5}$$

where τ_o is the initial tortuosity factor. The molecular diffusivity, D_M, depends on the diffusing species, and is typically approximated by:

$$D_M = K_M \frac{T^{3/2}}{P} \tag{6}$$

The Knudsen diffusivity, D_K, depends on the diffusing species and the pore structure. Methods for estimating D_K, τ_o, and the constant K_M are described elsewhere [5,14]. The additional subscript b will be used to denote diffusion inside of the bundles, and the additional subscript p refers to diffusion through the larger pores between bundles.

Nearly uniform infiltration occurs when diffusion is fast relative to the deposition rate, such that $\phi_o < \phi_{lim}$. Therefore, the maximum deposition rate where nearly uniform infiltration is possible corresponds to ϕ_{lim}. This also corresponds to the minimum infiltration time. Longer infiltration times occur when $\phi_o < \phi_{lim}$, and incomplete infiltration occurs when $\phi_o > \phi_{lim}$. When the rate limiting mass transport mechanism is diffusion into the preform (i.e. through the larger pores between bundles), the maximum deposition rate, $u_{MAX,p}$, corresponds to ϕ_{lim} and can be determined by rearranging Eq. (4):

$$u_{MAX,p} = \phi_{lim}^2 \left(\frac{V_s P_r D_{eop}}{2(RT)(1-\varepsilon_{ob})(1-\varepsilon_{op})}\right)\frac{r_f}{H^2} \tag{7}$$

An expression similar to Eq. (7) can be obtained for the case where the rate limiting mass transport mechanism is diffusion through the smaller pores inside of the bundles:

$$u_{MAX,b} = \phi_{lim}^2 \left(\frac{V_s P_r D_{eob}}{2(RT)(1-\varepsilon_{ob})}\right)\frac{r_f}{(2h)^2} \tag{8}$$

In Eq. (4) the characteristic distance h corresponds to a situation where the gases diffuse

into the bundle from both sides. In Eq. (8) the characteristic distance was taken as $2h$ which corresponds more closely to the case in which there is a significant concentration difference across the bundle, so that diffusion occurs from one side to the other. This is more appropriate for the limiting case based on Eq. (8) that is considered below.

First consider cases when the deposition rate at the outer surface of the preform, u_p, is less than or equal to $u_{MAX,p}$, such that C_p is uniform across the preform. Under most conditions, $u_{MAX,p} << u_{MAX,b}$ because $h << H$. Thus one approach to minimizing the infiltration time is to conduct the process with a uniform concentration across the preform, such that the minimum time corresponds to conditions where the deposition rate at the outer surface is $u_{MAX,p}$. When $u_p > u_{MAX,p}$ there are two additional regimes that can be considered. When u_p exceeds $u_{MAX,b}$ incomplete infiltration occurs in some or all of the bundles. There is also an intermediate regime:

$$u_{MAX,b} \geq u_p \geq u_{MAX,p} \tag{9}$$

The infiltration time in this regime will be shorter than when $u_p = u_{MAX,p}$. Under these conditions C_p is not uniform across the preform. Each bundle is infiltrated uniformly, however, the bundles near the outer surface of the preform are infiltrated first, and the bundles closer to the center are infiltrated later. Thus, the minimum time for the initial stage, t_{MIN}, corresponds to $u_p = u_{MAX,b}$. A simple estimate of t_{MIN} can be obtained by assuming that the bundle layers are infiltrated sequentially from the outer surface in towards the center, one layer at a time (e.g., the infiltration of the outermost layer is completed before the infiltration of the next outermost layer begins). In this case, t_{MIN} is the infiltration time for a single layer multiplied by the number of layers, n_b:

$$t_{MIN} \approx n_b \frac{\theta_b r_f}{u_{MAX,b}} = \frac{4RT}{\phi_{lim}^2 V_s P_r} \theta_b (1 - \varepsilon_{op})(1 - \varepsilon_{ob}) \frac{Hh}{D_{eob}} \tag{10}$$

In reality, the bundles towards the center of the preform will undergo some infiltration before the bundles towards the outer surfaces are completely infiltrated, thus the actual infiltration time is likely to be shorter than that described by Eq. (10). This approximation also ignores further deposition that occurs on the the outside of the bundles once they are overcoated (i.e., deposition into the large interbundle porosity). This will lead to slightly longer infiltration times than values of t_{MIN} that are estimated with Eq. (10). Numerical calculations are required to consider this behavior in more detail. These types of calculations are presented in the next section.

Equation (10) provides a convenient method for considering the effects of various parameters on the minimum infiltration time. The size of the preform and the bundles (H and h) both effect the value t_{MIN}, while the fiber size, r_f, does not. When Knudsen diffusion contributions are negligible, the times given by Eq. (10) have relatively simple relationships to temperature and pressure:

$$t_{MIN} \propto \frac{P}{P_r T^{1/2}} \tag{11}$$

This shows that t_{MIN} is a relatively weak function of temperature. The ratio P/P_r is the

moles of reactant per total moles of gas (i.e., a measure of the dilution). For the case of methyltrichlorosilane (MTS) in H_2 this is usually on the order of 0.1. With this ratio fixed, Eq. (11) shows that t_{MIN} is independent of the total pressure. The effects of Knudsen diffusion lead to a different temperature dependence that is still relatively weak. Knudsen diffusion effects also cause the value of t_{MIN} to increase with decreasing pressure, an effect which is only significant at relatively low pressures, and with relatively small pores. It is also important to note that t_{MIN} decreases as the dilution decreases (i.e., as P_r/P decreases). The approximate analysis presented here assumes that P_r/P is significantly less than one, which is often the case. The inverse relationship between t_{MIN} and P_r/P in Eq. (11) is less valid as this ratio approaches a value of unity.

Values of t_{MIN} that are calculated with Eq. (10) implicitly assume that the process variables T, P, and σ, and the deposition rate, u_{MAX}, can be chosen independently, however, in a real system the deposition rate is not independent of these variables (i.e., u is determined by T, P, σ, and the specific chemistry of the system). To treat this dependence, consider the ratio of the actual deposition rate and the maximum rate:

$$N_p = \frac{u_p}{u_{MAX,p}} = \frac{2\tau_{op}(1-\varepsilon_{op})(1-\varepsilon_{ob})}{\phi_{lim}^2 V_s \varepsilon_{op}} \frac{H^2}{r_f} A \exp\left(\frac{-E}{RT}\right)\left[\frac{P}{K_M T^{3/2}} + \frac{1}{D_K}\right] \quad (12)$$

$$N_b = \frac{u_p}{u_{MAX,b}} = \frac{2\tau_{ob}(1-\varepsilon_{op})(1-\varepsilon_{ob})}{\phi_{lim}^2 V_s \varepsilon_{ob}} \frac{(2h)^2}{r_f} A \exp\left(\frac{-E}{RT}\right)\left[\frac{P}{K_M T^{3/2}} + \frac{1}{D_K}\right] \quad (13)$$

where A and E describe the rate constant for the first-order deposition reaction.

To consider this analysis in more detail, the formation of SiC from MTS in H_2 was

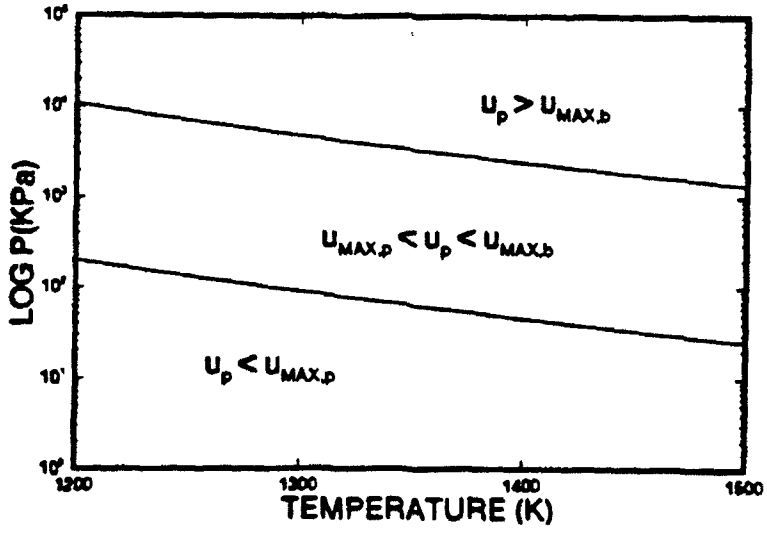

Figure 2. Conditions along the lower line correspond to Eq. (12) with $N_p = 1$ and conditions along the upper line correspond to Eq. (13) with $N_b = 1$.

used as a relevant example. Molecular diffusion was described with a value of K_m = 0.0107 cm^2 kPa/s/K$^{1.5}$ [5]. Knudsen diffusion was not dominant for the conditions considered here. Experimental data for SiC deposition from MTS yield values of A = 2900 cm^4/mol/s and E = 120 kJ/mol [15]. Although recent results show that this is an oversimplified description of the reaction kinetics [5], it is useful as an illustrative example. The value of ϕ_{lim} depends on the criterion for adequate infiltration and on the structure of the porous material. CVI into fiber bundles has been analyzed with detailed numerical calculations, using a variety of different methods of estimating D_e [5]. These calculations show that more than 90% of the initial porosity is infiltrated when $\phi_{lim}^2 <$ 0.1. This condition was used to analyze the infiltration of a preform with $2H$ = 3 mm, h = 100 μm, and r_f = 10 μm. The lines corresponding to N_p = 1 and N_b = 1 are shown in Fig. 2. The minimum infiltration time described by Eq. (10) corresponds to conditions that are on the upper line. For conditions above these lines ($N_p > 1$ and $N_b > 1$) infiltration on the appropriate length scale (i.e., h and H) is not uniform. For conditions below the lines the infiltration time is longer than the minimum.

NUMERICAL CALCULATIONS

An accurate description of microstructure evolution during infiltration requires numerical solutions. To simplify these calculations, ε_p was treated as a constant. This assumes that the larger pores between the bundles are unchanged during the initial stage. The gas-phase concentration in between the bundles, C_p, the concentration inside of the bundles, C_b, and ε_b were described with appropriate differential equaions:

$$\frac{\partial(\varepsilon_p c_p)}{\partial t} = \frac{\partial}{\partial Z}\left(\alpha_p \frac{\partial c_p}{\partial Z}\right) - \lambda \sum_{j=1}^{I} \beta_j c_{b,j} \tag{14}$$

$$\frac{\partial}{\partial X}\left(\alpha_b \frac{\partial c_b}{\partial X}\right) - \beta c_b = 0 \tag{15}$$

$$\frac{\partial \varepsilon_b}{\partial t} = -\frac{\beta}{V_s} C_0 c_b \tag{16}$$

The initial conditions (i.e., t = 0) are:

$$\varepsilon_b(X,0) = \varepsilon_{ob} \tag{17}$$

$$\varepsilon_p(Z,0) = \varepsilon_{op} \tag{18}$$

$$c_b(X,0) = c_p(Z,0) = 0 \tag{19}$$

For C_p, the boundary conditions at $Z = 0$ and $Z = 1$ are:

$$c_p(0,t) = 1 \tag{20}$$

$$\frac{\partial c_p}{\partial Z} = 0 \tag{21}$$

respectively. The dimensionless parameters used in these equations are:

$$c_p(Z,t) = \frac{C_p(z,t)}{C_0} \tag{22}$$

$$c_b(X,t) = \frac{C_b(x,t)}{C_0} \tag{23}$$

$$Z = \frac{z}{H} \tag{24}$$

$$X = \frac{x}{2h} \tag{25}$$

$$\alpha_p = \frac{D_p}{H^2} \tag{26}$$

$$\alpha_b = \frac{D_b}{(2h)^2} \tag{27}$$

$$\lambda = (1-\varepsilon_p)\frac{1}{I} \tag{28}$$

$$\beta = A\exp(-\frac{E}{RT})S_{wb}\frac{1}{V_s} \tag{29}$$

where x and z are distances into the bundle and preform respectively, and I is the number of grid points for each bundle. The deposition in the bundles was treated as a sink term for the preform calculation (see Eq.(14)). Equations (20) and (21) describe symmetric diffusion from opposite sides of the preform, where the surface concentration is constant. These equations were solved numerically using a finite difference scheme, where the values of C_p obtained by solving Eq. (14) were used as boundary conditions

for Eq.(15). The calculation was thus conducted by iterating between a solution for the preform (for C_p), and a series of calculations for the layers (for C_b). The procedure was halted when the external surface of all bundles reached ε_c (i.e., $\varepsilon_b = 0.001$).

The solutions in Fig. 3(a) correspond to conditions where $u_p = u_{MAX,p}$. In this case the porosity inside of the bundles is uniform across the sample at all times. This is consistent with the simple analysis in the previous section, which indicates that the reactant concentration in the gas-phase should be uniform across the preform under these conditions. The solutions in Fig. 3(b) correspond to conditions where $u_p = u_{MAX,b}$. (the value of P necessary to achieve this value is quite high, however, the calculation is still useful for illustrative purposes). In this case the infiltration of the individual bundles is relatively uniform, however, the bundles closer to the outer surface are infiltrated sooner. This is also consistent with the analysis in the previous section.

The infiltration times under different conditions are plotted in Fig. 4. Infiltration was assumed to be complete when the porosity at the outer surfaces of each bundle reached a value of $\varepsilon_b = 0.001$ (i.e. $\varepsilon_b = \varepsilon_c$). The deposition rate was altered by changing only the total pressure; this also corresponds to changing the value of ϕ_o. As expected, the total infiltration time decreases as the deposition rate increases.

DISCUSSION AND CONCLUSIONS

In general, the minimum infiltration time for the initial stage should occur with conditions that are between the two lines in Fig. 2. Physically, this corresponds to uniform infiltration of the bundles, and to nonuniformities in the large, interbundle pores that are acceptably small. Conditions close to or on the upper line will lead to shorter infiltration times, however, under these conditions there will be a porosity

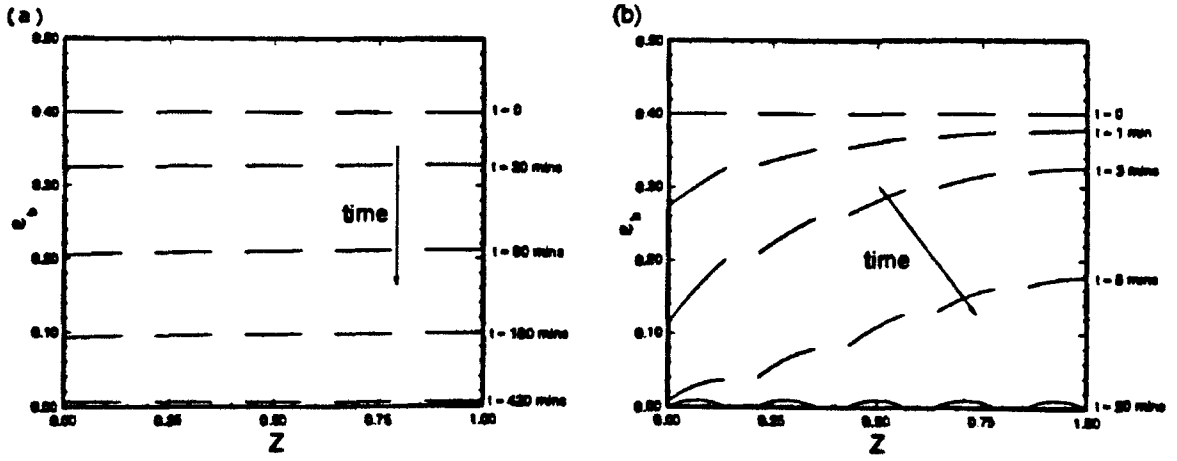

Figure 3. Porosity versus position in the preform for SiC deposition from MTS, with H = 1.5 mm, h = 100 μm, and r_f = 10 μm. Each set of five short lines corresponds to the five bundles that comprise the half-thickness of the preform.
(a) $u_p = u_{MAX,p}$: T = 1400 K; P = 45.3 kPa; P_r/P = 0.1
(b) $u_p = u_{MAX,b}$: T = 1400 K; P = 2446.3 kPa; P_r/P = 0.1

gradient in the large interbundle pores at the end of the initial stage (i.e., after all of the smaller interbundle pores are infiltrated). If this gradient is to large it will be impossible to achieve uniform infiltration during the final stage of CVI. This effect will be more severe in thicker samples. The lower boundary corresponds to conditions where this gradient will be nonexistent, but where infiltration also requires more time. Some nonuniformity across the preform can be tolerated during the initial stage, as long as the total amount of material that is deposited in the large pores fills a relatively small fraction of the total amount of this large-scale porosity.

For each of the two lines in Fig. 2 there is an optimum temperature at a given pressure (and vice versa). The dilution does not effect the position of these lines, although, as already noted, the dilution does have a significant effect on the absolute value of the minimum infiltration time (see Eq. 11). Equations (12) and (13) show that the position of the lines in Fig. 2 depends on both the deposition kinetics (A and E), and physical dimensions of the preform (r_f, h, H, ε_{ob}, and ε_{ip}). Thus a diagram like Fig. 2 can be obtained for a given deposition chemistry and a given preform architecture, and then used to determine the optimum processing conditions.

The numerical calculations are generally consistent with the Thiele modulus analysis that was used to create Fig. 2. At $u_p = u_{MAX,p}$ infiltration is uniform across the preform, and at $u_{MAX,b}$ infiltration proceeds from the outer surface towards the center. The bundles in the interior of the preform undergo some infiltration before the outer bundles are completely infiltrated. Thus, the numerical results that correspond to $u_{MAX,b}$ indicate a shorter infiltration time than Eq. (10). This comparison is shown in Fig. 4. The infiltration time that corresponds to $u_{MAX,p}$ and falls on the lower line in Fig. 2 is also shown in Fig. 4. In this case, the estimate obtained with Eq. (1) and the value of $u_{MAX,p}$ coincides with the numerical calculations.

To consider the final stage of infiltration, the calculations presented here must be extended to describe the infiltration of the larger porosity between bundles. As already discussed, the infiltration of these larger pores can also affect the initial stage of the process. Thus a model where ε_p varies will also be useful for considering these effects.

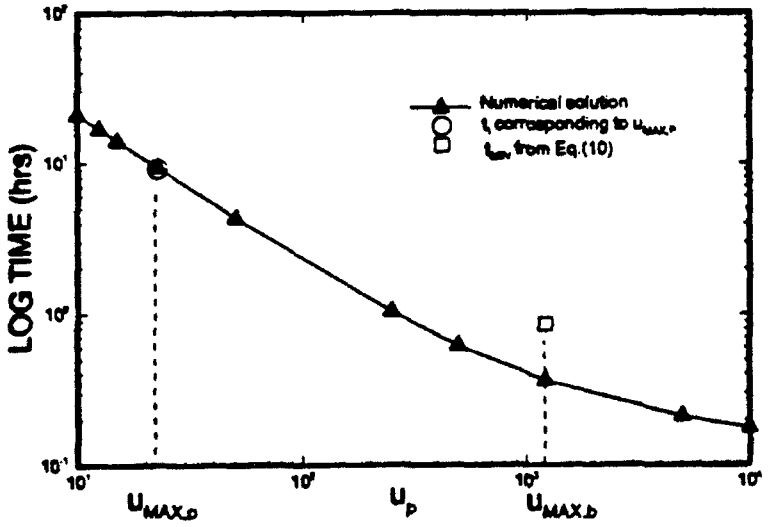

Figure 4. Infiltration time vs. u_p for the system described in Fig. 3, at T = 1400 K and P_i/P = 0.1. The deposition rate was varied by varying the total pressure, P.

REFERENCES

1. E. Fitzer and R. Gadow, "Fiber-Reinforced SiC", Am. Ceram. Soc. Bull. 65, 326 (1986).

2. P.J. Lamicq, G.A. Bernhart, M.M. Dauchier, and J.G. Mace, "SiC/SiC Composite Ceramics", Am. Ceram. Soc. Bull. 65, 336 (1986).

3. D.P. Stinton, A.J. Caputo, and R.A. Lowden, "Synthesis of Fiber-Reinforced SiC Composites by Chemical Vapor Infiltration", Am. Ceram. Soc. Bull. 65, 347 (1986).

4. T.M. Besmann, B.W. Sheldon, R.A. Lowden, and D.P. Stinton, "Vapor-Phase Fabrication and Properties of Continuous-Filament Ceramic Composites", *Science*, 253, 1104-9 (1991).

5. B.W. Sheldon and T.M. Besmann, "Reaction and Diffusion Kinetics during the Initial Stages of Isothermal Chemical Vapor Infiltration", *J. Am. Ceram. Soc.*, 74, 3046-53 (1991).

6. S.V. Sotirchos, "Dynamic Modelling of Chemical Vapor Infiltration", *AIChE J.* 37, 1365-78 (1991).

7. C.H.J. van den Brekel, R.M.M. Fonville, P.J.M. van der Straten, and G. Verspui, "CVD of Ni, TiN, and TiC on Complex Substrates", Proc. Electrochem. Soc. 81-7 (CVD-VIII), 142 (1981).

8. T.L. Starr, "Deposition Kinetics in Forced Flow / Thermal Gradient CVI", Ceram. Eng. Sci. Proc. 9, 803 (1988).

9. S.M. Gupte and J.A. Tsamopoulos, "Densification of Porous Materials by Chemical Vapor Infiltration", J. Electrochem. Soc. 136, 555 (1989).

10. N-H. Tai and T-W. Chou, "Modeling of an Improved Chemical Vapor Infiltration Process for Ceramic Composites Fabrication", J. Am. Ceram. Soc. 73, 1489 (1990).

11. G.Y. Chung, B.J. McCoy, J.M. Smith, D.E. Cagliostro, and M. Carswell, "Chemical Vapor Infiltration: Modelling Solid Matrix Deposition in Ceramic-Ceramic Composites", *Chem. Eng. Sci.* 46, 723-733 (1991).

12. Y.S. Lin and A.J. Burggraaf, "Modelling and Analysis of CVD Processes in Porous Media for Ceramic Composite Preparation", Chem. Eng. Sci. 46, 12, 3067-80 (1991).

13. E.W. Thiele, "Relation Between Catalytic Activity and Size of Particle", Ind. Eng. Chem. 31, 916 (1939).

14. C.N. Satterfield, Mass Transfer in Heterogeneous Catalysis, MIT Press, Cambridge (1970).

15. K. Brennfleck, E. Fitzer, G. Schoch, and M. Dietrich, "CVD of SiC-interlayers and their interation with carbon fibers and with multilayered NbN-coatings", Proc. Electrochemical Soc. 84-6, 649 (1984).

Overview of Optical Fiber Sensors Embedded in Concrete

A. Méndez and T. F. Morse
Laboratory for Lightwave Technology
Brown University, Providence, RI 02912

ABSTRACT

In this paper an analysis is presented on the use of embedded optical fiber sensors in concrete elements and structures for the non-destructive measurement of internal stress and strain as well as for the assessment of structural integrity. A discussion of the fundamental materials and micro-mechanical aspects regarding the fiber/matrix interaction is given. In addition, a summary of the experimental results obtained to date is made along with the applications sought for this new technology.

INTRODUCTION

The use of optical fiber sensors embedded within composites for the measurement of internal strain and the detection of structural damage in aerospace applications has proved to be an effective non-destructive evaluation (NDE) technique and become the subject of substantial research [1]. Recently however, the focus of the applications has also centered around the field of civil engineering with aims at exploring the possibilities of embedding, prior to curing, optical fiber sensors into reinforced concrete elements and structures such as buildings, bridges, dams and tanks for the NDE of structural integrity and the measurement of the internal state of stress. The first proposal on the application of optical fiber sensors embedded in concrete buildings and structures was given by Méndez et al. [2], who described the potential applications of this approach along with a study on the fundamental issues regarding its practical implementation. Subsequently, a small number of researchers in the U.S. and Europe have been working on different ways to measure stress and strain in concrete using optical fibers [3-15] as well as to determine the health condition in a building [16].

Since the infrastructure of civil engineering works around the world is in state of deterioration due to the aging of the materials, excessive use, overloading, weathering, lack of maintenance and proper inspection. It has become increasingly important in the last few years to determine the safety of a structure by the NDE of its strength and integrity. This assessment is essential for the repair, retrofit, rehabilitation, life extension or replacement of the structure in question. Furthermore, it would be very useful to develop means for the feedback and control of the state of health of a structure.

The field of civil engineering, although highly advanced in materials and structural analysis and design, is comparatively deficient in its evaluation techniques. Many of the methods used are destructive. Various non-destructive methods for testing concrete have been developed [17]. However, not all of these methods are very reliable and, in some instances, they can only be used on a comparative qualitative basis. NDE techniques being studied rely on the absorption,

transmission and scattering of X and γ rays; response to nuclear activation; electrical resistance; projectile penetration; mechanical and ultrasonic pulse velocity; vibration; magnetization and several others.

Optical fibers, because their small size and lightweight, offer the possibility to be embedded within cement or concrete without affecting their properties and used as sensitive, but rugged, transducers of mechanical perturbations. The basic principle behind embedded fibers to characterize the state of a composite material is that light sent through the fiber has either its intensity, phase, wavelength or polarization altered by changes in the mechanical and thermal states of the surrounding host. In this respect, fibers have the ability to provide high resolution temperature and strain measurements, detect the onset and growth of cracks, as well as to monitor creep and thermal stresses. In addition, the actual location of a fault can be determined by interrogating the back-reflected signal coming from the fiber, using optical time-domain reflectometry (OTDR) techniques. All this information can ultimately be used to provide "real-time" information on the state of a specific concrete element or structure by means of a built-in damage detection and evaluation system based on a grid of optical fiber sensors embedded within the structure during its construction.

In order to implement these ideas, a fundamental understanding of the factors involved in the embedding process in concrete is needed. In this paper, an analysis of the materials and micro-mechanical issues of the fiber/matrix interaction is presented. Different schemes for the internal measurement of stress and strain with fiber sensors will be described. In addition, a summary of the experimental results obtained to date will be given.

EMBEDDING OF OPTICAL FIBERS IN CONCRETE

In order to perform properly the function of internal strain/temperature sensor, several issues regarding the embedding of the optical fibers and the phenomena at the fiber/concrete interface must be investigated. For instance, the interfacial properties determine the efficiency of load transfer to the embedded fiber, as well as having a strong effect on the reliability and reproducibility of the sensor's response over time. Furthermore, an understanding of the micromechanics in the interphase region is of vital importance in the interpretation of what the sensor is measuring and how does this measurement relates to the measurand of interest in the composite.

In addition, the mechanical and chemical durability of the silica glass optical fibers in the harsh cement environment must be addressed. This presents two major problems. First, the introduction, without damage, of the fibers into the plastic, aggregate-filled and mechanically vibrated environment of the cement/concrete paste. Secondly, the water-rich and highly alkaline environment of a cement paste will have a tendency to attack glass fibers. Next, we will discuss some of these ideas in more detail.

- *Chemical Attack*

It is well known that water and hydroxyl ions react with the surfaces of glass fibers reducing their strength by promoting accelerated crack growth under stress [18]. However, water is only present in cement and concrete mixes during the first few days of curing, since most of it is lost by evaporation and chemical reaction. Furthermore, depending on its characteristics [19], concrete can be highly impermeable which explains in part why the reinforcing steel does not corrode once inside the concrete.

On the other hand, cement is strongly alkaline (with a pH of approximately 12) and will tend to corrode glass fibers (see Fig. 1). Fortunately, considerable research has been done on the use of glass fibers as a reinforcing material in portland cement [20]. These studies have led to the development of alkali-resistant glass fibers [21,22], like the so-called Cem-Fil fiber [23], characterized by having about 17% weight of zirconia (Z_rO_2) in its composition. Experimentally,

it has been demonstrated that polymeric coatings on the fibers improve their chemical durability [24,25]. Particularly interesting is the protection obtained by coating standard telecommunication silica-glass optical fibers with a polyetherimide coating [26].

• *Interfacial Bonding*

Although an adequate bond might develop between fibers and concrete due to curing shrinkage (caused by the loss of moisture with a decrease in volume of about 0.05 percent), as well as by the mechanical keying and constriction caused by the formation and growth of crystals of hydrated calcium aluminosilicates, it is still not clear whether or not a good bond exists between glass fibers and concrete for an efficient load transfer. Therefore, experimental results such as fiber pull-out tests are needed to determine the shear strength at the fiber/matrix interface.

The characteristics of the optical fiber coating play an important role as well. Good coating adhesion to both the concrete matrix and the fiber are necessary in order to prevent any delamination of the fiber from the coating, or worst yet, decoupling of the coated fiber from the concrete host. This is very important, for otherwise, any assessment made on the condition of the structure will be meaningless.

Some experimental studies on the coating performance of coated optical fibers embedded in epoxy resin revealed delamination at the coating/fiber interface in preference to the coating/epoxy resin interface [27].

• *Fiber Orientation and Coating Effects*

Assuming that a perfect bond exists between fiber and coating as well as between coating and concrete matrix, the only parameters that affect the response of the embedded sensor are the fiber orientation with respect to the applied load and the mechanical properties of the layered matrix/coating/fiber region.

Consider the two most general cases. When the embedded fiber runs parallel to to the direction of the applied strain and when the fiber is perpendicular to it. This in turn results in axial and radial deformations, respectively, of the fiber. Fig. 2 depicts the case of a fiber parallel to the applied load. Although a good bond is assumed at the interface, notice how the stress seen by the fiber varies as a function of position along its length. There is, however, a region in which the stress is uniform all along. The minimum distance for which this occurs is called the critical length (l_c) of an embedded fiber. Physically what this means is that, in order to develop a strain in the fiber equal to that of the surrounding host, the gage length of the embedded section must be at least as long as the critical length for a given set of radii and elastic moduli. Nanni et al. [5] have computed l_c to be approximately 20 times the fiber's diameter.

For the case of a fiber embedded with its axis perpendicular to the applied load (see Fig. 3), the actual strain present in the fiber is now dependent on the stiffness of the coating material as compared to that of the glass fiber. In other words, the fiber coating acts as a mechanical buffer that can drastically diminish the load transfer between the matrix and the fiber. The relation between strain in the fiber to strain in the concrete matrix is found to be [5]:

$$\epsilon_{fiber} = \epsilon_{concrete} \frac{2E_{coating}}{E_{fiber} + E_{coating}} \tag{1}$$

Therefore, for the perpendicular configuration, it becomes necessary to coat the fibers with hard coatings in order to insure adequate load transfer. Standard telecommunication-grade optical fibers are not suitable for this application since their soft primary coating is designed to absorb mechanical perturbations to prevent microbending losses.

• *Fiber Embedding and Placement*

One of the main difficulties associated with the practical implementation of these ideas consists in the introduction of the fibers into the uncured concrete mix. Furthermore, the placement of the fibers inside the concrete cannot be random, but rather it must comply with the requirements and objectives imposed by the type of measurement or detection one wishes to make with the embedded sensor.

Since about 70% of the total volume in a concrete mix is occupied by stone aggregates and other fillers, many obstacles will be encountered in the way of the fiber in any given direction. In addition, fibers will be subjected to severe mechanical abuse during the pouring process as a result of the pumping, vibrating and shoveling of fresh concrete. To overcome these difficulties different techniques for embedding fibers into concrete have been proposed [2]. In one of such techniques (see Fig. 4a), the optical fiber is protected by a metallic tube of a small diameter such as hypodermic stainless steel tubing. The tube is laid in the desired position within the formwork while concrete is poured on it. Once the filling operation has been completed, and before hardening starts, the tube is gently slid out leaving the fiber in place. This technique has the added advantage of promoting the formation of a smooth cement boundary at the surface of the fiber as a result of cement "bleeding". Fig. 4b illustrates a different approach where the sensing region of the fiber (gage length) is allowed to move freely inside a protective sleeve. Loads are transmitted to the fiber ends by means of sliding metallic fiber clamps. This technique bears resemblance to the load-transfer mechanism for an extrinsic Fabry-Perot strain sensor [15]. Fiber embedding experiments using cabled optical fibers protected by plastic jackets have also been tried [9]. However, it is not clear whether such approach will result in an adequate transfer of load to the fiber.

All of the above problems, along with the unfavorable conditions that in general prevail at most construction sites have led to the development of pre-fabricated fiber-optic sensing panels [4]. In this way, fiber sensors can be carefully protected and placed inside special panels or frames which are subsequently transported and installed on site.

As mentioned before, an adequate placement of the fiber sensors is crucial for their effective use. Sensor location is strongly dependent upon application. Thus, what it might be an appropriate placement for a strain sensor, it might not necessarily be so for a crack or curing sensor.

To understand this better, consider the nature and behavior of a reinforced concrete (RC) structure. A RC structure is a continuous frame in which all of its members are rigidly connected to one another. Said members experience deformations under the action of tensile and compressive forces produced by the loads that the structure must bear. Associated with these deformations are internal stresses and strains that differ in character and intensity upon their location in the structure as well as on the nature of the loads. However, because concrete is strong in compression but weak in tension, tensile stresses and strains are of greater concern. Thus, fiber-optic strain sensors should be placed running parallel to the steel reinforcement where the tensile stresses are to be found. Fibers should also be placed next to stirrups, which are steel bars used as reinforcement against diagonal tensile stresses resulting from the interaction between horizontal and vertical shear stresses in the concrete.

For the case of detection and monitoring of cracks, fibers should be loop around an actual crack, or in the potential site for the formation of one. In this way, the fiber can measure the displacement of the crack opening without sacrificing its own integrity (Fig 5a). This is applicable to regions in the structure where cracks are to be expected, but that their size must be monitored to be kept within safe limits. Conversely, there are instances where the sole presence of a crack is cause of alarm, as is the case in prestressed concrete elements. In this type of application, fibers must be placed perpendicular to the probable direction of crack growth as seen in Fig. 5b to detect their presence [4,8].

APPLICATIONS

The fundamental applications envisioned for this new technology are listed in Table 1 below. They can be grouped in three main areas, namely:

- Structural monitoring and damage evaluation
- Experimental stress analysis
- Management and control of systems and service installations

The first group explores the incorporation of single- and multi-mode fiber sensors within structural concrete elements such as beams, columns, arches, slabs and others, so that stress, strain, flexure, bending, curing, cracks and creep in concrete can be measured individually, as well as the deflection and bending of structures as a whole. In the next section, a summary of the experimental results obtained to date by various groups working in this field will be made.

Table 1. Applications of embedded optical fiber sensors in concrete

MATERIAL	STRUCTURAL	SERVICE INSTALLATIONS
strength	stress	heating
curing	strain	cooling
creep	shear	pressure
shrinkage	bending	electric currents
uniformity	deflection	security
voids and defects	cracks	fire alarm
modulus of elasticity	thermal stresses	elevators
steel corrosion	damage detection	telecommunications

In the field of experimental stress analysis, fibers would make sensitive and versatile sensors for the measurement of mechanical characteristics of structural members in experimental studies. This might be particularly useful with structures and members having complex shapes for which analytical solutions can be difficult to obtain. An answer can be obtained by measuring experimentally the state of stress in a model. Another example would be to use a grid of fiber strain sensors embedded in the runways of airports to evaluate the stresses on the pavement during the landing and take-off of airplanes. The 2-D stress mapping obtained in this fashion would be helpful in the redesign and maintenance of such pavements.

Furthermore, embedded fiber optic strain sensors would enable structural engineers to compare between measured and designed values of stress, bending moments and deflection. From this information more accurate design factors can be determined which would make structures safer and more economical to construct.

The third set of applications considers that building services and installations (such as heating, air conditioning, lighting, electricity distribution and consumption, security, fire alarms, etc.) can be operated more efficiently and economically using fiber optic sensors that monitor and measure the state of affairs of pertinent parameters. For instance, reading of the pressure, flow and temperature of water pipes could be used to regulate the temperature and distribution of running water by controlling valves, pumps and boilers as required. Similarly, the temperature in rooms, hallways and offices could be monitored and controlled automatically. Electric currents could be controlled and regulated according to demand. Fibers coated with special heat-sensitive coatings could be used as distributed heat sensors for use in fire

alarm systems. And the list goes on. In this fashion, integration of all the information supplied by a network of fiber and regular sensors into a single processing center within the same facility would result in a "smart building".

PREVIOUS WORK

As we mentioned before, the potential of fiber optic sensors for the non-destructive evaluation and monitoring of concrete structures has just begun to be appreciated. To date, only a small number of studies report research activity connected with this field. However, it is expected that this will change in the near future. Next, we will describe briefly the latests developments in the field by area of application.

• *Thermal Stresses and Curing of Concrete*

Concrete curing is always accompanied by the liberation of heat from the chemical reactions which bring about the hardening of the portland cement. This heat of hydration causes a rise in the internal temperature of concrete in comparison to the exterior surfaces. As cooling begins, the outermost layers rapidly gain both strength and stiffness. Any restraint of the fine contractions will result in tensile stresses. These effects are not critical in regular cast concrete structures, but they are a major consideration in massive concrete. Evidently in this latter case, large amounts of heat need to be dissipated during the curing process if flawless concrete members are desired. In this respect, embedded fiber optic temperature sensors would make possible the measurement of the internal temperatures in massive concrete, allowing the control of the cooling rate during the curing process.

The ideas outlined above have already been successfully implemented in practice by a construction company in Japan which reports monitoring concrete curing in a distribution tunnel using a commercially available fiber-optic distributed temperature sensor [6]. In addition, using a different approach, Huston et al. have monitored the curing of concrete by measuring the ligth transmission of embedded multimode optical fibers inside a test beam [9].

Furthermore, information on the dynamics of heat transfer for an entire building or structure (caused by the thermal stresses due to changes in ambient temperature such as freezing and thawing, wetting and drying or heating and cooling) could be obtained by a network of embedded temperature sensors situated in strategic locations.

Although not a curing sensor, a fiber optic refractive index sensor has been developed by Ansari et al. to detect the air-bubble content in entrained fresh concrete [7]. The fiber sensor detects changes in the reflected light intensity from a scanning probe tip as a consequence of the difference in refractive index between cement paste and air.

• *Crack Detection and Monitoring*

The presence of cracks in concrete is inevitable. Cracks are caused by the stressing of the steel reinforcement under normal load conditions, restrained drying shrinkage or by temperature-induced volumetric changes. The onset and growth of cracks can easily be detected by monitoring the intensity of the light transmission of strategically embedded fibers. While their location can be determined by means of OTDR techniques.

Rossi and LeMaou [4] report the detection of cracks in concrete using an embedded multimode ($100\mu core$) optical fiber, which has its coating material removed in several small sections. A drop in the fiber's light throughput was observed whenever a crack propagated across any of the uncoated fiber sections. The method was applied to monitor the presence of cracks at different locations within the shell of a motorway tunnel. During their embedding, fibers were protected by metallic tubes which were subsequently removed after the concrete pouring took place.

Crack opening displacements in concrete beam specimens were measured by Ansari [8] using circular fiber loops. The light transmission through the loop varied as a function of the transverse perturbation induced by the crack growth. However, it was concluded in this study that the main disadvantage of such approach is that the crack paths must be known a priori.

• *Bending, Deflection and Displacement*

Other mechanical effects of interest to civil engineers and architects are the deflections, bending and displacements of long-span members, frames and massive structures. In this area, Wolff and Miesseler [10] measured the elongation and tensile stresses present in a $53m$ long bridge by embedding optical fiber sensors inside the deck. A total of 8 optical fibers were used (4 placed in the upper and 4 in the lower side of the concrete slab). Measurement of the fiber's elongation over time revealed information regarding the effects of temperature and creep in the bridge.

A different approach proposed measuring the loads acting on a concrete bridge by means of multimode optical fibers embedded inside elastomeric bearings fitted between the bridge's deck and supports [12]. The magnitude of the loads are determined by the attenuation induced by the microbending loss in the fibers.

Displacements of the span joints in a concrete dam have been monitored using specially designed opto-mechanical arrangements [14]. In one of its configuration, out-of-limit displacements are detected by the loss in light transmission through a multimode fiber when pressed by a spring-loaded movable ram. A second configuration allowed measurement of the relative joint displacements from the attenuation changes resulting from bending a small fiber loop mechanically connected to the joints.

• *Stress and Strain Measurement*

Knowledge of the state of stress and strain in a structure is vital for the prediction of its behavior. Mechanical strains present, from which stresses can subsequently be inferred, can be determined with relative ease by embedding fibers within critical regions. Dimensional and/or refractive index changes in the fiber can then be used to measure the strain transferred to the fiber.

Different fiber sensors are suitable for this purpose [2]. Experimentally though, Nanni et al. [5] have measured compressive strains inside cement test cylinders by measuring the interference between the two polarization components of the light traveling through a birefringent fiber embedded parallel to the applied load. Similarly, for the case of a fiber embedded perpendicular to the load, polarization maintaining fibers were used. In this case, the interference is produced by the phase difference between the two orthogonal polarization modes induced by the stress acting on the fiber.

The birefringence effect has also been used to measure the internal strain inside a concrete column. Tardy et al. developed a fiber optic transducer consisting of an uncoated low birefringence single-mode fiber squeezed between two metallic ribbons [3]. The external load acting on the ribbon (plus the pre-load resulting from the ribbon's deflection) give rise to an induced birefringence that is easily measured by the interference obtained between the two polarization modes in the fiber. In this fashion, fiber sensors 14 cm long were sand-coated and embedded inside concrete specimens without special care. Sensor response during compression tests showed a relatively large induced birefringence as indicated by the reduced degree of polarization observed. Nonetheless, high sensitivity and a good agreement with theory were observed. This same technique has also been used to detect and measure the weight of vehicles in motion on a road [11].

Using an interferometric technique, Escobar et al. have measured strains during three-point flexural tests of concrete beams instrumented with surface-bonded and embedded single-mode fibers [13]. The results obtained demonstrated the feasibility of embedding optical fibers within concrete elements without having to change normal casting procedures.

Good linearity in the sensor's response was obtained, while no degradation in the fiber's response was observed after the casting process. Also, no detrimental aging effects were noticed due to the concrete environment for the teftzel-coated fibers after five years of embedding.

Kruschwitz et al. [15] describe the use of extrinsic Fizeau fiber interferometers attached to and embedded within concrete specimens. The Fizeau cavities are formed by the flat ends of two optical fibers closely space and aligned inside a glass capillary. Any displacement between the fiber ends, due to applied strains or temperature changes, varies the gap separation which can be measured by the spectral shift of the interference fringes in the cavity. Sensor heads of this type have been embedded inside reinforced concrete beams. Sensors were placed in the cement matrix and attached next to the rebar. Strains measured under mechanical loading revealed a five percent difference between strains in the matrix and the steel reinforcement. This difference is attributed to several factors such as slippage between host and sensor, non-parallel alignment or experimental errors. Furthermore, similar sensors were epoxy-bonded to the lower side of the deck of a concrete bridge to measure the strains produced by a moving truck at different points along the span.

A more basic approach has been used by Huston et al. who have used embedded multimode optical fibers, with and without plastic jackets, for the load-to-failure testing of a reinforced concrete beam [9]. In this scheme, the light transmission intensity in the fibers was monitored as a function of applied load. Experimental results indicate that the light intensity remains practically unaffected until a certain load is reached and the fiber breaks. At this point, the power intensity of the light is a function of the axial separation loss between the two fiber ends. Furthermore, it was observed that bare fibers were prone to breaking during the curing process.

- *Building Monitoring*

As we mentioned it before, a network of several fiber optic sensors embedded throughout different locations in a building could act as a "nervous" system for said structure, supplying information on its state of health. This combined with a computerized processing center could probably lead to a smart building capable of self interrogation and control.

The first step towards achieving some of the above ideas has been taken by Huston and coworkers who have embedded a variety of single- and multi-mode fiber optic sensors into a university campus building while it was under construction [16]. The fiber sensors are intended to measure vibration, wind pressures, in-service loading, concrete creep, temperature, detect cracks, etc. while interrogated by a microcomputer. The information obtained from such a sensor grid will be used to study and monitor the building's in-service performance and overal structural health.

SUMMARY

Fiber optic sensing technology offers the possibility of non-destructive, in-situ, measurement of stress, strain, temperature and deformation of elements and structures made of concrete. Novel applications in the analysis and evaluation of structural integrity as well as in the management and control of building services are envisioned.

The performance of embedded optical fiber sensors in concrete is affected by the mechanical and chemical durability of the glass fibers, interfacial bonding, fiber orientation and coating characteristics. An understanding of the material and micro-mechanical phenomena present at the interface region, as well as their connection to the measurand one wishes to measure in the host matrix, are essential in the development of durable sensors with accurate, reliable and repeatable response.

To date, only a small number of experiments using optical fibers in conjunction with concrete or cement are reported in the literature. Most of them focus on the measurement of stress/strain inside concrete elements using birefringent or microbend-sensitive fibers as well as Fabry-Perot cavities. Other sensors have been designed to detect the onset of

cracks, measure entrained air content in fresh concrete, weight vehicle traffic, determine displacements in bridges and dams, monitor thermal stresses and curing of massive concrete.

Nonetheless, experimental research is needed to investigate, among others, adequate embedding techniques, the long-term stability and durability of the fibers inside concrete, coating adhesion to fiber and matrix, micro-mechanics of load transfer as well as practical measurement schemes. In addition, proper interfacing and collaboration is needed between researchers in the fields of fiber optics and civil engineering.

Although new and very young, this technology offers interesting possibilities for NDE applications and certainly promises to enhance the fields of fiber optics, smart structures and civil engineering.

ACKNOWLEDGEMENTS

This work was supported by NSF under grants MSS-8904872, Solid-Geo Mechanics Program and MSS-901793, Non-Destructive Evaluation Program. The authors wish to thank Prof. F. Méndez for helpful discussions.

REFERENCES

1. Udd, E., "Overview of Fiber Optic Applications to Smart Structures", Review of Progress in Quantitative Nondestructive Evaluation, Plenum Press, 1988.

2. Méndez, A., Morse, T. F. and Méndez, F., "Applications of Embedded Optical Fiber Sensors in Reinforced Concrete Buildings and Structures", SPIE Proceedings, Vol. 1170, Fiber Optic Smart Structures and Skins II, pp. 60-69, September 1989.

3. Tardy, A., Jurczyszyn, M., Caussignac, J. M., Morel, G. and Briant, G., "High sensitivity Transducer for Fibre-Optic Pressure sensing to Dynamic Mechanical Testing and Vehicle Detection on Roads", Springer Proceedings in Physics, Vol. 44, Optical Fiber Sensors, H. J. Arditty, J. P. Dakin and R. Th. Kersten, Eds., pp. 215-221, 1989.

4. Rossi, P. and LeMaou, F., "New Method for Detecting Cracks in Concrete Using Fiber Optics", Materials and Structures, Research and Testing (RILEM), Vol. 22, No. 132, pp. 437-442, November 1989.

5. Nanni, A., Yang, C. C., Pan, K., Wang, J. and Michael, R., "Fiber-Optic Sensors for Concrete Strain/Stress Measurement", ACI Mat. Jor., Vol. 88, No. 3, pp. 257-264, 1991.

6. "Fiber Optics and Curing Concrete", Photonics Spectra, January 1990, p. 22.

7. Ansari, F. and Chen, Q., "Fiber-Optic Refractive-Index Sensor for Use in Fresh Concrete", Appl. Op., Vol. 30, No. 28, pp. 4056-4059, 1991.

8. Ansari, F., "Real-Time Monitoring of Concrete Structures by Embedded Optical Fibers", in Nondestructive Testing of Concrete Elements and Structures, Proceedings of the ASCE, San Antonio, TX, April 1992, pp. 49-59.

9. Huston, D., Fuhr, P., Kajenski, P. and Snyder, D., "Concrete Beam Testing with Optical Fiber Sensors", ibid., pp. 60-69.

10. Wolff, R. and Miesseler, H., "Monitoring of Prestressed Concrete Structures with Optical Fiber Sensors", Proc. 1st European Conference on Smart Structures and Materials, Glasgow, 1992, pp. 23-29.

11. Teral, S., "Vehicle Weighing in Motion with Fiber Optic Sensors", ibid., pp. 139-142.

12. Caussignac, J. M., Chabert, A., Morel, G., Rogez, P. and Seantier, J., "Bearings of a Bridge Fitted with Load Measuring Devices Based on an Optical Fiber Technology", ibid., pp. 207-210.

13. Escobar, P., Gusmeroli, V. and Martinelli, M., "Fiber-Optic Interferometric Sensors for Concrete Structures", ibid., pp. 215-218.

14. Holst, A. and Habe;, W., "Fiber-Optic Intensity-Modulated Sensors for Continuous Observation of Concrete and Rock-Fill Dams", ibid., pp. 223-226.

15. Kruschwitz, B., Claus, R. O., Murphy, K. A., May, R. G. and Gunther, M. F., "Optical Fiber Sensors for the Quantitative Measurement of Strain in Concrete Structures", ibid., pp. 241-244.

16. Huston, D., Fuhr, P., Kajenski, P., Ambrose, T. and Spillman, W., "Installation and Preliminary results from Fiber Optic Sensors Embedded in a Concrete Building", ibid., pp. 409-411.

17. Malhotra, V. M., Testing Hardened Concrete: Nondestructive Methods, American Concrete Institute, Monograph No. 9, 1986.

18. Wang, T. T., Vazirani, H. N., Schonhorn, H. and Zupko, H. M., "Effects of Water and Moisture on Strengths of Optical Glass (Silica) Fibers Coated with a UV-Cured Epoxy Acrylate", J. Appl. Polmr. Sci., Vol. 23, pp. 887-892, 1979.

19. Fintel, M., Editor, Handbook of Concrete Engineering, Van Nostrand Reinhold, 1985.

20. ACI Committee 544, "State-of-the-Art Report on Fiber Reinforced Concrete", ACI Report No. 544-1R-82, 1982.

21. Majumdar, A. J., "Glass Fiber Reinforced Cement and Gypsum Products", Proc. Roy. Soc. Lon., No. A 319, 1970, pp. 69-78.

22. Majumdar, A. J. and Ryder, J. F., "Reinforcement of Cements and Gypsum Plasters by Glass Fibers", Science of Ceramics, Vol. 5, 1970, pp. 539-564.

23. Proctor, B. A., "Glass Fibre Reinforced Cement", Physics in Technology, Vol. 6, 1975, pp. 28-32.

24. Golosova, L. V. and Varlamov, V. P., "The Interface in Portland Cement Matrix Reinforced with Fiber Glass with Long Hardening Times", Inorg. Matt., Vol. 20, No. 12, 1984, pp. 1782-1785.

25. Datta, A. B., Gupta, A. P. and Paul, A., "Alkaline Durability of Glass Fibre Containing S_iO_2, PbO and Al_2O_3", J. Matt. Sci., Vol. 21, 1986, pp. 2633-2642.

26. Kuwabara, T. et al., "Polyetherimide Coated Optical Silica Glass Fiber with High Resistance to Alkaline Solution", OFS '89 Conference, Houston, TX, paper WA4.

27. Haaksma, R., Cehelnik, M. and Kerkhoff, J., "An Investigation of Optical Fiber Coating Performance in Embedded Sensing Applications", Mat. Res. Symp. Proc., Vol. 172, pp. 71-77, 1990.

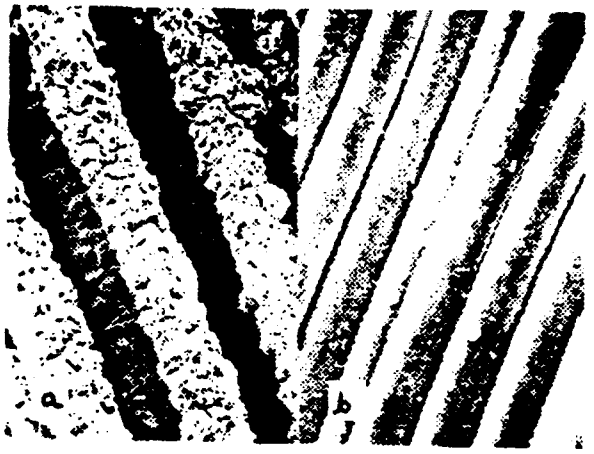

Figure 1 : SEM pictures of a) Corroded glass fibers and b) Alkali-resistant fibers, after exposure to a cement environment. (Photo courtesy of Fiberglass UK Ltd.)

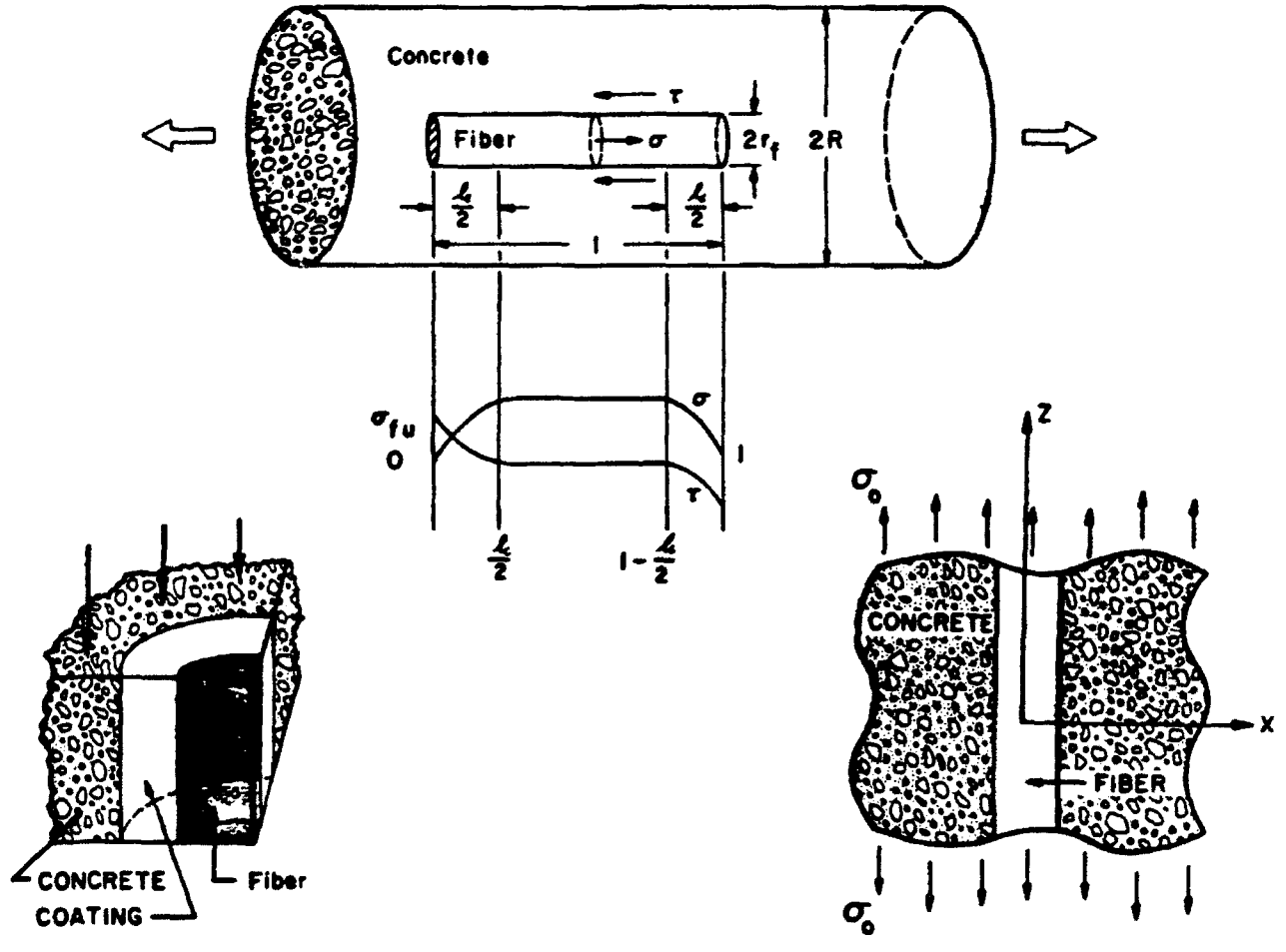

Figure 2 : Schematic of an optical fiber embedded with its axis parallel to the applied load.

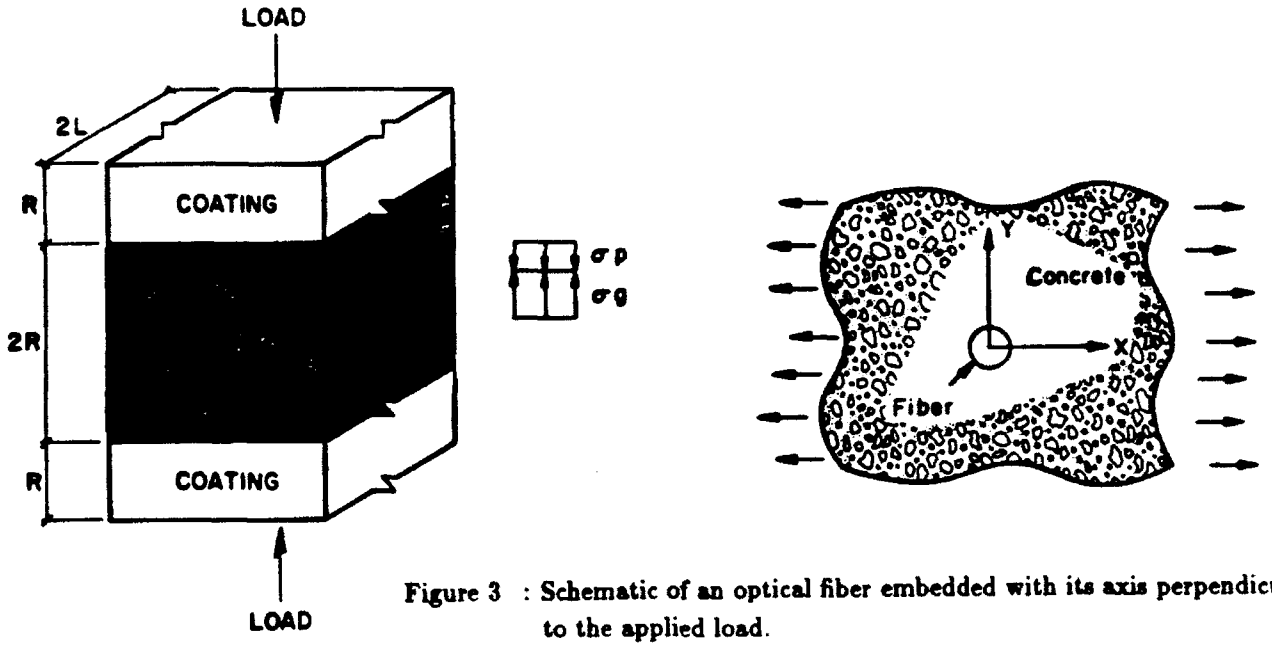

Figure 3 : Schematic of an optical fiber embedded with its axis perpendicular to the applied load.

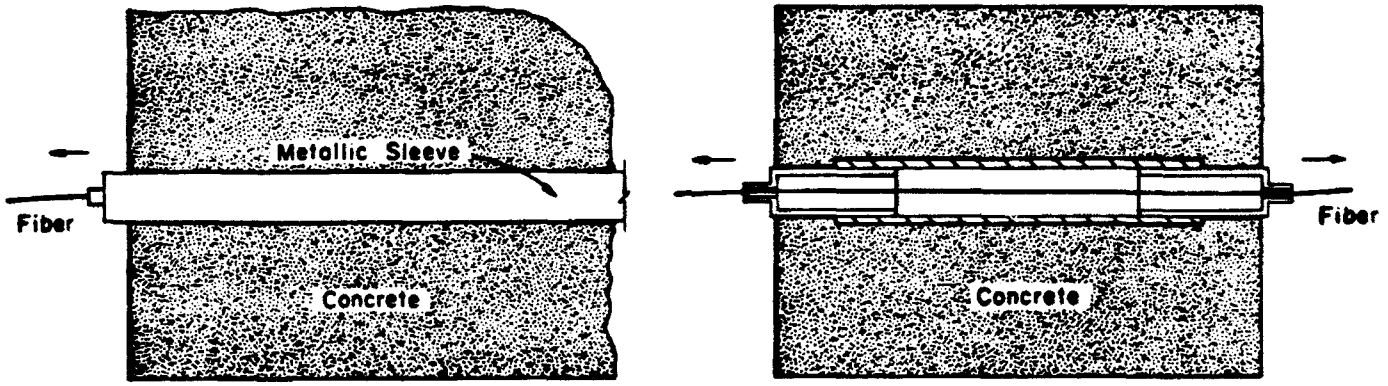

Figure 4. : Fiber embedding methods.

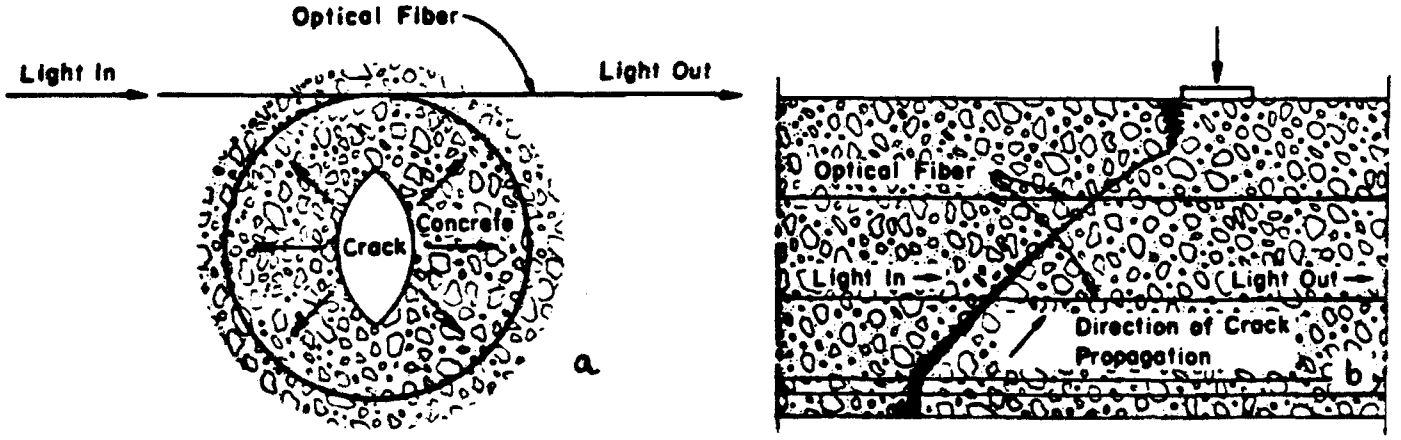

Figure 5. : Optical fiber sensorplacement for a) Crack aperture growth and b) Crack onset detection.

Fiber Optic Electric Field Micro-Sensor

A. Méndez, T. F. Morse
Laboratory for Lightwave Technology
Brown University, Providence, RI 02912

K. A. Ramsey
Batelle Memorial Institute, Columbus Division
Columbus, OH 43201

Abstract

A new method and apparatus are presented by which electric fields (AC and DC) can be measured in high voltage (HV) environments above ground using a variable gap, Fabry-Perot micro-cavity transducer which is mounted on the tip of a multimode optical fiber. By constructing the Fabry-Perot cavity as a conductive Faraday cage, external electric fields can be detected by the electrostatic forces they exert on the top surface of the cavity where a flexible, corrugated, silicon diaphragm is incorporated. Under the action of the electrostatic forces, the diaphragm deflects varying the gap of the cavity which is measured as a change in the backreflected light. To make the device insensitive to bending and transmission losses in the fiber, a dual wavelength referencing technique is employed. Thus, the magnitude of the electric field can be related to a change in the intensity ratio at two different wavelengths.

The sensor is characterized by being small, lightweight, unobtrusive, accurate and immune to electromagnetic interference (EMI), temperature or pressure effects.

DC electric fields in the range of 0 to $300 KV/m$ have been successfully measured. The minimum field intensity detected was of the order of $40 KV/m$. This relatively low sensitivity is due to the high stiffness of the diaphragm arising from the high boron-diffusion. However, higher sensitivities are possible by thinning the diaphragm, increasing the radius, reducing the boss ratio or decreasing the corrugation depth.

Introduction

With the strong dependence that today's society has on electricity, the safe, reliable and efficient generation, transmission and distribution of electric power has become of vital importance. Furthermore, in order to monitor, control and meter properly electric energy an extensive number of measurements are necessary within a given power network. This is confirmed by a recent study which indicates that electric power utilities, along with gas and water utilities, are the most measurement intensive sectors of the U.S. economy [1]. In this context, the measurement of electric fields in high voltage, high power equipment is of fundamental importance to the power industry. Knowledge of the local electric fields, both AC and DC, present in generators, transformers, power lines or any other HV component is essential in the understanding of their operation and behavior, as well as in the verification of new or modified designs. In addition, defective, malfunctioning or degraded equipment can be detected by continuously monitoring the changes in the electric fields being generated.

Moreover, recent concerns over the biological effects of electromagnetic radiation [2,3] have motivated studies on the electric fields generated by power and transmission lines. All this has promoted the development of new, efficient and economical sensors and sensing technologies. Existing electric field meters typically have conductive parts which cause field distorsion. For this reason, fiber optic sensors have received special attention by power utilities over the last few years [4-6]. However, present work on the use of optical fibers for the measurement of electric fields relies almost exclusively on the use of the Pockels and the piezoelectric effects [7-12].

Electrostatic Forces

There are 3 fundamental mechanisms for the measurement of electric fields: electrostatic induction, electrophysical phenomena (such as the pockels and the piezoelectric effects) and electrostatic forces. Methods based on electrostatic induction rely on the accurate measurement of the current resulting from the time variation of the charges induced on a metallic body immersed in the field, and thus are not suitable for use with fiber optics. Sensors based on electro-optic effects are usually bulky and suffer from detrimental temperature effects. Electrostatic force effects, on the other hand, are more amenable to be used with optical fibers and, although they go as the square of the electric field, they can be effectively used in schemes where adequate linearization is possible. The physical principle behind them is explained below.

Whenever a conductor is placed into an electric field, the free electrons in the material rearrange themselves in such a way as to render its interior field-free. This electron arrangement gives place to an induced charge on the surface of the conductor. However, the net charge in the body remains zero. The Coloumbic attraction between the induced surface charge and the external electric field, E_o, develops an electrostatic force density f_s which acts normal to the surface of the conductor, for otherwise the charges would move along the surface contradicting the assumption of an equipotential surface. The magnitude of f_s is given by [13]:

$$f_s = \frac{\epsilon_0}{2} E_{surf}^2 \tag{1}$$

where E_{surf} is the intensity of the field right at the surface of the conductor*. Notice that the direction of f_s is always pointing away from the surface, regardless of the sign of the field. Such forces are very weak, and when acting on objects exert negative pressures of the order of a few pascals.

Principle of Operation

By combining the concept of a Faraday cage with an optical interferometer it is possible to measure this low pressure, since the transmissivity (or reflectivity) of a Fabry-Perot cavity is extremely sensitive to changes in the length of the cavity, which in this case can be caused by a pressure differential acting upon a movable mirror arrangement at one end of the cavity. Fiber optic sensors based on this principle have been successfully demonstrated [14,15]. In addition, flat silicon diaphragms have been used in the past as pressure transducers [16]. These flat diaphragms, however, exhibit non-linear behavior for small thicknesses and uneven deflection across their radius. These problems can be corrected by the introduction of corrugations in the plane of the diaphragm which linearize its response making it move in a piston-like fashion [17].

Fig. 1.1 depicts the Fabry-Perot cavity (FPC) design which is formed by a suspended, thin and corrugated silicon diaphragm bonded to a glass substrate. A metallic film on the surface of the silicon diaphragm acts as one of the cavity mirrors, while a thin, partially transmitting, aluminum film on the substrate acts as the other. This structure is then mounted on the tip of a 100/140 μm multimode optical fiber onto which a GRIN lens has been previously attached, as illustrated in Fig. 1.2. In this manner, light traveling in the core of the fiber will be collimated into the cavity, and the back-reflected light will be re-launched into the optical fiber.

---

*The magnitude and distribution of E_{surf} is the result of the superposition of the applied field E_o plus the field resulting from the induced charges E_i. Hence, the magnitude of E_{surf} is a function of position and is strongly dependent on the geometry of the conductive body.

The reflectance of a Fabry-Perot will be a function of spacing, index of refraction, mirror reflectivities and wavelength. Assuming that the mirrors are lossless, the reflected intensity is given as the following [18]:

$$\frac{I_r}{I_o} = \frac{4\sqrt{R_1 R_2}sin^2(\frac{2\pi h}{\lambda})}{(1-\sqrt{R_1 R_2})^2 + 4\sqrt{R_1 R_2}sin^2(\frac{2\pi h}{\lambda})} \tag{2}$$

with

$$h = h_o + \delta h \tag{3}$$

where R_1 and R_2 are the mirror reflectivities, h_o is the height of the unperturbed cavity, and δh is the deflection of a bossed, corrugated membrane given by the expression [19]:

$$\delta h = \frac{\epsilon 3 P a^4}{16 E' t^3} \tag{4}$$

where

$$\epsilon = \frac{8(1-r^4)}{(q+3)(q+1)}\left(1 - \frac{8qr^4(1-r^{q-1})(1-r^{q-3})}{(q-1)(q-3)(1-r^4)(1-r^{2q})}\right) \tag{5}$$

and for the case of shallow sinusoidal corrugations:

$$q = \sqrt{1 + 1.5\frac{H^2}{t^2}} \tag{6}$$

where P is the differential pressure, a the membrane radius, r the boss to diaphragm radius ratio, $E' = E \setminus (1-\nu^2)$ is the plate modulus of elasticity, t the thickness, H the corrugation depth and q the corrugation quality factor.

Since the cavity is formed by a highly-doped silicon well and a metallic film, both good conducting materials at low frequencies, the structure acts as an ultra thin faraday cage, the interior of which contains no electric fields. Thus, a net electrostatic force will be exerted on the top surface of the silicon diaphragm when exposed to an external electric field[†]. As the gap in the cavity increases, under the influence of the negative electrostatic pressure induced by the field, the intensity of the backreflected light into the fiber changes accordingly. Hence, the reflected light spectrum associated with the cavity shifts to longer wavelengths for increasing magnitudes of electric field. The spectral shift of the interferometer peak can be interrogated using an LED, which translates the cavity's spectral shifts into intensity variations of the LED output spectrum thus yielding a spectrally modulated envelope.

To make the sensor immune to variations in light intensity due to bending or transmission losses, as well as any possible degradation of the light source, a dual-wavelength referencing technique is used (see Fig. 1.3). Light from an LED source is launched into the multimode fiber and coupled into the cavity by the GRIN lens. Inside the cavity, each wavelength experiences a different amount of reflection due to the spectral dependence characteristics of the Fabry-Perot. The backreflected light is then split in two beams by means of an optical fiber coupler. Specific wavelengths are selected out of the LED's broad spectrum by narrow bandpass optical filters, and their intensities measured using optical detectors. In this fashion, the magnitude of the electric field is related to a change in the intensity ratio at these two wavelengths, with the added advantage that the reading obtained will be independent of any transmission losses since both signals undergo the same effects along their path.

The pressure in the cavity chamber is equalized to that of the ambient by vent holes that communicate to the surrounding environment, thus there is no net differential pressure acting on the diaphragm. Furthermore, because the sensor is protected by a glass cap, it is possible to be used in harsh environments such as that present in an oil-filled transformer.

[†]The electrostatic pressure generated by the field might not necessarily be uniform across the diaphragm depending on the probe orientation. However, the net pressure acting on the diaphragm will always be the same for identical operating conditions.

Electrostatic Analysis

Since the sensor is designed for the measurement of electric fields in and around HV environments, it is of vital importance to know what are the effects that it introduces into the field. To answer this question numerical calculations were performed using ELECTRO [20]. ELECTRO is a software program for the calculation of two-dimensional (including rotational symmetric), static or quasi-static electric fields using the boundary element method.

Static, 2-D analyses[‡] were performed for three different probe orientations: $\alpha = 0°, 45°$ and $90°$, assuming that a uniform electric field E_0 prevailed before the introduction of the cavity. This is achieved by defining a constant potential across a given distance in the program.

Calculation of the electric field distribution in the neighborhood of the cavity (Fig. 1.4) reveals that the perturbation of the field vanishes at a distance equivalent to half the cavity length away from the center. Furthermore, according to Fig. 1.5*a* which is a graph of the electric field intensity along the cavity, and Fig. 1.5*b* which depicts the field across the cavity, the field on the surface of the diaphragm is practically equivalent to E_0. However, inside the cavity it drops to zero, as a consequence of the Faraday-Cage effect. Inside the pyrex substrate the field has a value of about one fifth the magnitude of E_0, which is in good agreement with the fact that the permittivity in this medium is five times greater than that of air.

Another important aspect is the variation of E_{surf}. As seen from Fig. 1.5a, the field is practically uniform across the diaphragm, but increases sharply at cavity points A,B,E and F reaching values in excess of 10 times E_0. This is a result of the edge effects which give rise to a concentration of the field lines on the sharp edges or points of the cavity as illustrated in Figs. 1.6*a* and 1.6*b*. This problem is even more severe for values of α greater than zero, as the potential field is distorted resulting in higher field intensities. Because of this non-uniform distribution of E_{surf}, the design of the diaphragm makes use of corrugations that allow only the deflection of the inner portion of the diaphragm, where E_{surf} is more uniform at $\alpha = 0$. The corrugations also help prevent any edge effects from producing any high magnitude forces on the diaphragm, due to the mechanical isolation between the diaphragm and the rest of the cavity.

In addition, to minimize the magnitude of the high fields associated with the edge-effects of the cavity, a curved glass cap is used to cover and protect the entire probe. The dielectric sheath helps to smooth the field lines around the probe as seen from Fig. 1.7*a*, thus reducing the intensity of the electric field in the exterior periphery of the cover, while maintaining E_{surf} on the diaphragm practically unaffected (see Fig. 1.7*b*).

Fabrication of a Prototype

The fabrication process for the prototype sensing probe involved three tasks. Namely, the fabrication of silicon diaphragms, the deposition of mirror coatings and assembly of the FOC and finally, the attachment of the assembled FPC to the end of a especially terminated optical fiber.

The corrugated diaphragms were fabricated using standard photolithographic and silicon micromachining techniques [21]. First, a small octagonal recession $1.7\mu m$ deep and slightly larger than the diaphragm itself is made on the epi side of a (100) silicon wafer using a KOH solution. Afterwards, a series of grooves, $5\mu m$ deep, are plasma etched on the surface of the wafer. These channels will define the top side of the corrugations. A heavy diffusion of boron is then introduced to act as an etch-stop for a wet anisotropic etch on the backside of the wafer. Since the boron diffusion follows the contour of the epitaxial features on the wafer, a deep etching on the backside of the wafer will result in a thin, corrugated, diaphragm with a thickness dependent on the depth of the boron diffusion. The small vent holes on the diaphragm are obtained by blocking the diffusion of boron with a SiO_2 mask, thus allowing the etch to attack the silicon all the way through in these regions.

[‡] Although the problem entails a 3-D object, it is possible to reduce it to the 2-D case due to the rotational symmetry of the circular cavity.

boss ratio or decreasing the corrugation depth.

No corona or discharge effects were observed in the course of the field tests, and repeatable results were obtained in almost all cases, except for a few occasions for which the damping effects altered the response of the sensor.

Acknowledgements

This work was supported by the Electric Power Research Institute, Palo Alto, CA, under grant RP-8004-05.

The authors wish to thank Mr. Jan Stein of EPRI, for all his support throughout the entire project, as well as Prof. B. Patterson for numerous helpful discussions and L. Reinhart for his invaluable assistance.

References

1. DonVito, P.A., "Estimates of the Costs of Measurements in the U.S. Economy", Nat. Bur. Stand., Planning Report 21, 1984.
2. Carstensen, E. L., *Biological Effects of Transmission Line Fields*, Elsevier, 1987.
3. Fitzgerald, K., Morgan, G., and Nair, I., "Electromagnetic Fields: The Jury's Still Out", IEEE Spectrum, August 1990, pp. 22-35.
4. Erikson, D.C., "The Use of Fiber Optics for Communications, Measurement and Control within High Voltage Substations", IEEE Trans. Pwr. App. Sys., Vol. PAS-99 No. 3, pp. 1057-1063, 1980.
5. Kirkham, H., Jonhston, A., Lutes, G., Daud, T. and Hyland, S., "Power System Applications of Fiber Optics", Jet Propulsion Laboratory Report # 84-28, Pasadena, CA, 1984.
6. Tenesse Valley Authority, "Research Planning Study of Fiber Optic Sensors", Electric Power Research Institute final report # ER-6428, 1989.
7. Hamasaki, Y. et al., "OPSEF: An Optical Sensor for Measurement of High Electric Field Intensity", Elect. Lett., Vol. 16 No. 11, pp. 406-407, 1980.
8. Donalds, L.J. et al., "Electric Field Sensitive optical Fibre Using Piezoelectric Polymer Coating", Elect. Lett., Vol. 18 No. 8, pp. 327-328, 1982.
9. Mermelstein, M.D., "Optical-fiber Copolymer-film Electric field Sensor", Appl. Opt., Vol. 23 No. 7, pp. 1006-1009, 1983.
10. Bohnert, K.M., and Nehring, J., "Fiber-Optic Sensing of Electric Field Components", Appl. Opt., Vol. 27 No. 23, pp. 4814-48-18, 1988.
11. Huang, S.J., and Erickson, D.C., "The Potential Use of Optical Sensors for the Measurement of Electric Field Distribution", IEEE Trans. Pwr. Dev., Vol. 4 No. 3, pp. 1579-1585, 1989.
12. Vohra, S.T., Bucholtz, F., and Kersey, A.D., "Fiber-Optic DC and Low-Frequency Electric Field Sensor", Opt. Lett., Vol. 16 No. 18, pp. 1445-1447, 1991.
13. Lorrain, P., Corson, D. and Corson, F., Electromagnetic Fields and Waves, Third Edition, W. H. Freeman and Company, New York, p.110., 1988.
14. Lieberman, R. A. and Blonder, G. E., "An Improved Interferometric Pressure Optrode", SPIE Proc., Vol. 838, pp. 49-59, 1987.
15. Mitchell, G. L., "A Review of Fabry-Perot Interferometric Sensors", Springer Verlag proceedings in Physics, Vol. 44, Optical Fiber Sensors, pp. 450-457, 1989.

16. Saaski, E.W., Hartl, J.C., Mitchell, G.L., "A Fiber Optic Sensing System Based on Spectral Modulation", ISA Proceedings, paper #86-2803, 1986.

17. Jerman, J. H., "The Fabrication and Use of Micromachined Corrugated Silicon Diaphragms", Sens. Act. A21-A23, pp. 988-992, 1990.

18. Born, M. and Wolf, E., Principles of Optics, Pergamon Press, New York, 1984.

19. Haringx, J. A., "The Rigidity of Corrugated Diaphragms", Appl. Sci. Res., Vol. A2, pp. 299-325, 1950.

20. ELECTRO is a Copyright of Integrated Engineering Software Inc., Winnipeg, Manitoba, Canada R3B 1Y6.

21. Petersen, K. E., "Silicon as a Mechanical Material", Proc. IEEE, Vol. 70, No. 5, pp. 420-457, 1982.

22. Wallis, G. and Pomerantz, D. I., "Field Assisted Glass-Metal Sealing", J. Appl. Phys., Vol. 40, No. 10, pp. 3946-3949, 1969.

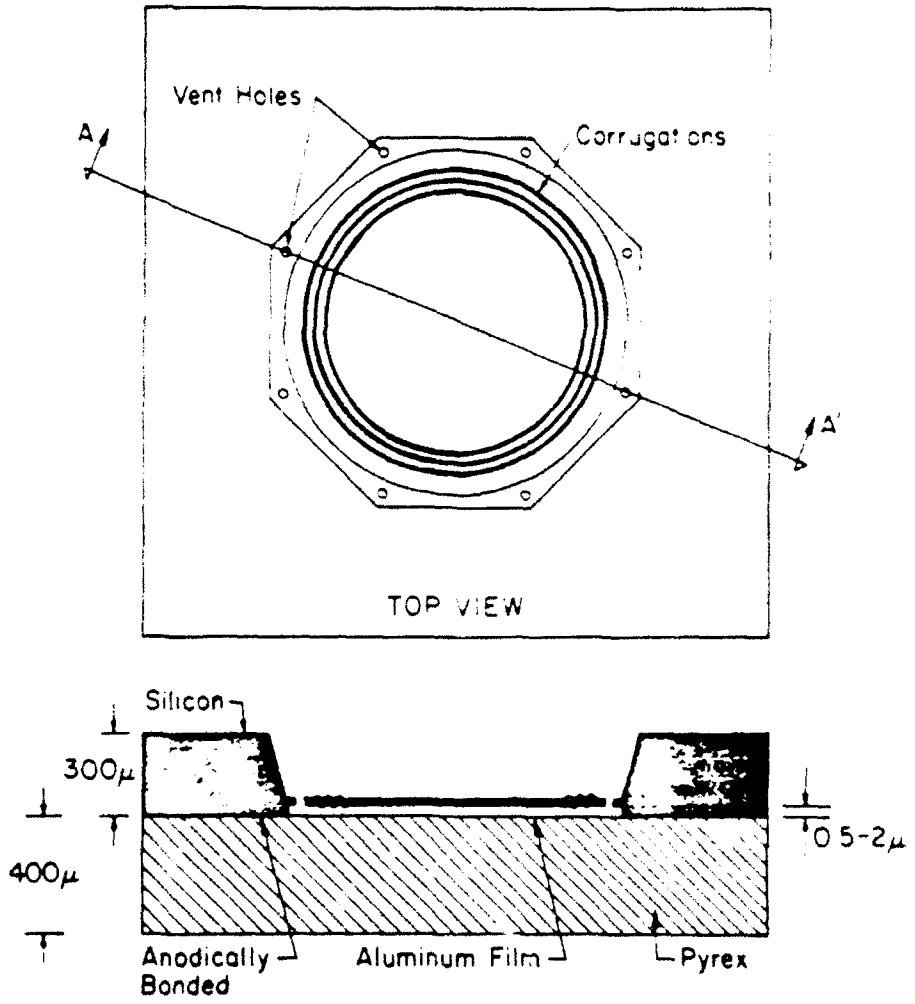

Figure 1.1: Fabry-Perot microcavity a) top-view, and b) cross-section

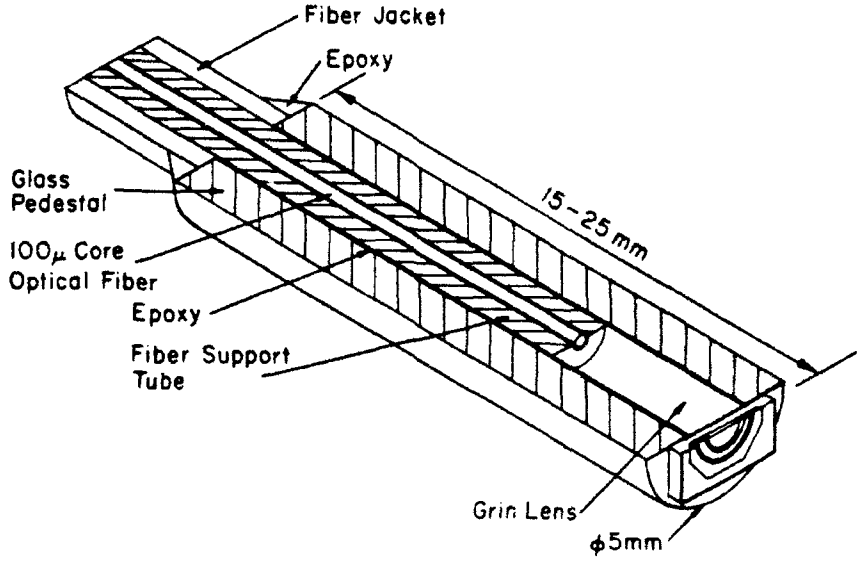

Figure 1.2: Mounting of sensor cavity on an optical fiber

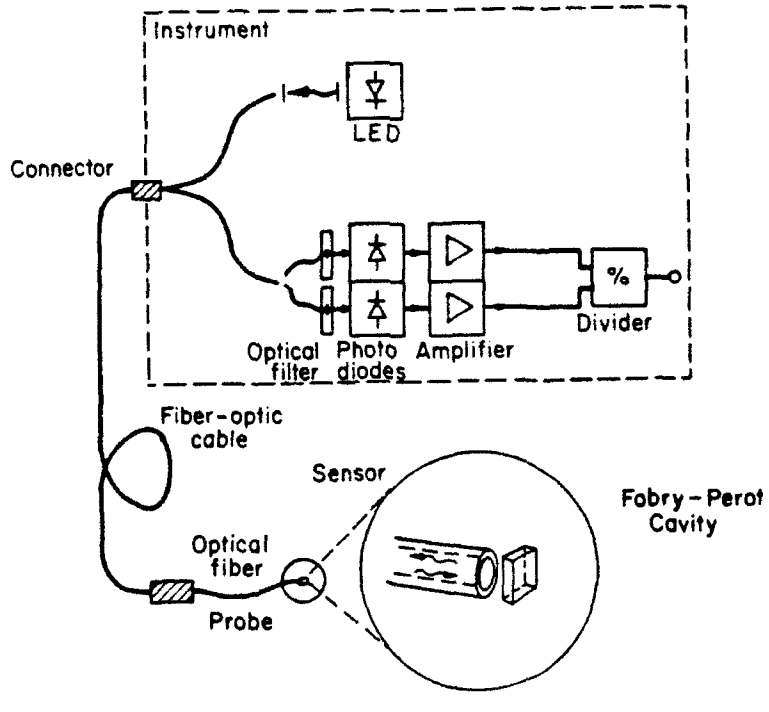

Figure 1.3: Sensor system schematic

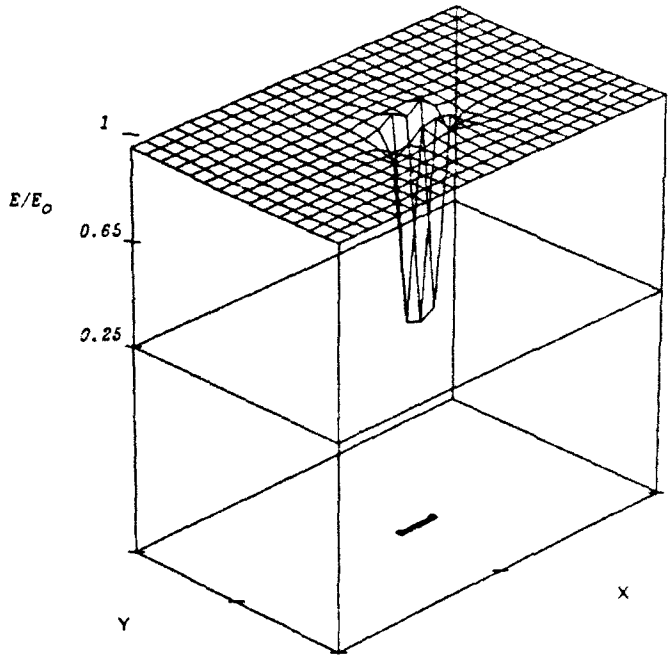

Figure 1.4: Electric field distribution away from the cavity

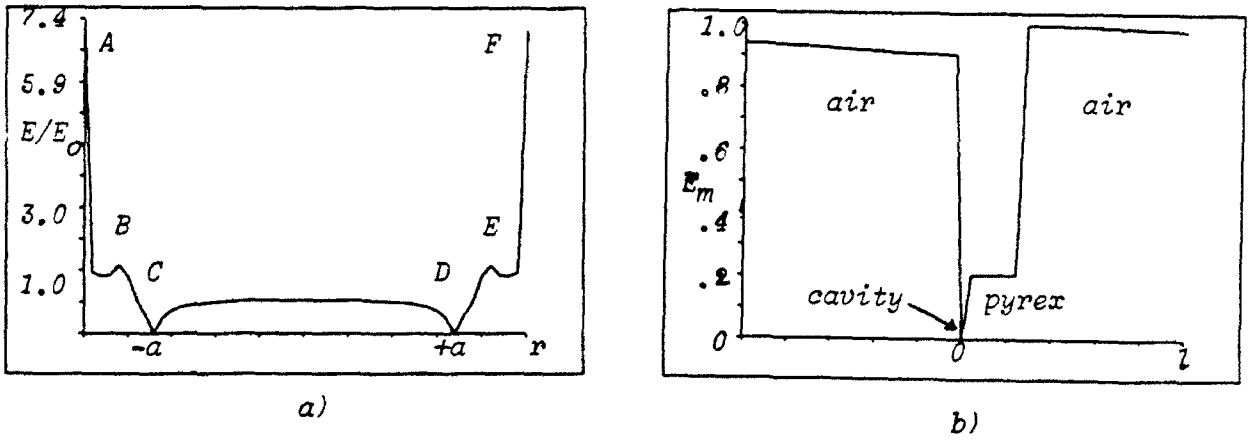

Figure 1.5: Electric field intensity, a) along the cavity and, b) across the cavity

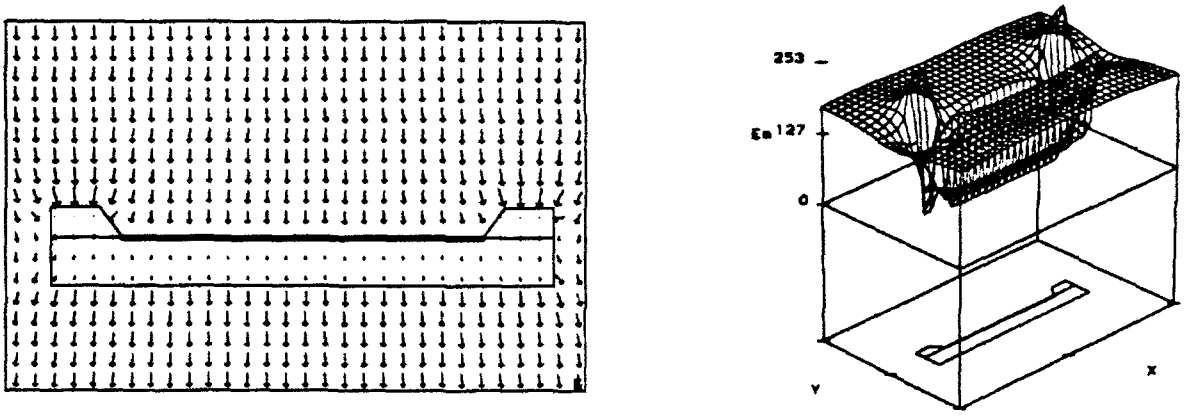

a) b)

Figure 1.6: a) Electric field arrow plot and b) Electric field distribution for $\alpha = 0°$

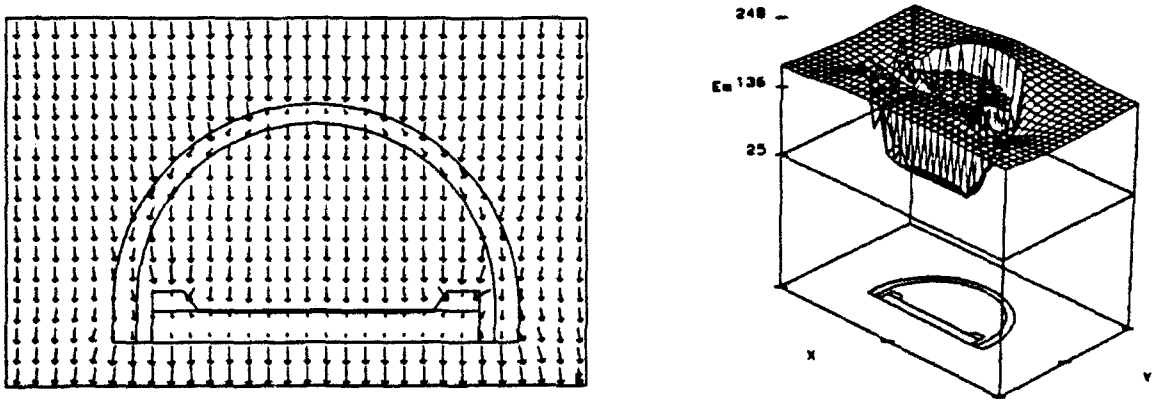

a) b)

Figure 1.7: a) Electric field lines for covered sensor and b) Surface electric field for covered sensor

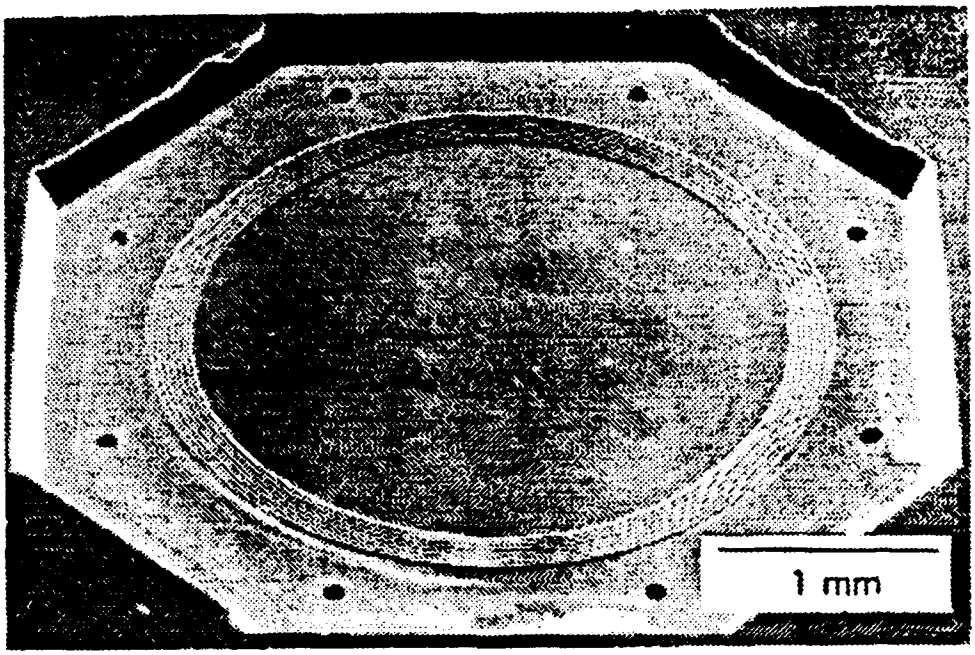

Figure 1.8: SEM perspective of silicon diaphragm.

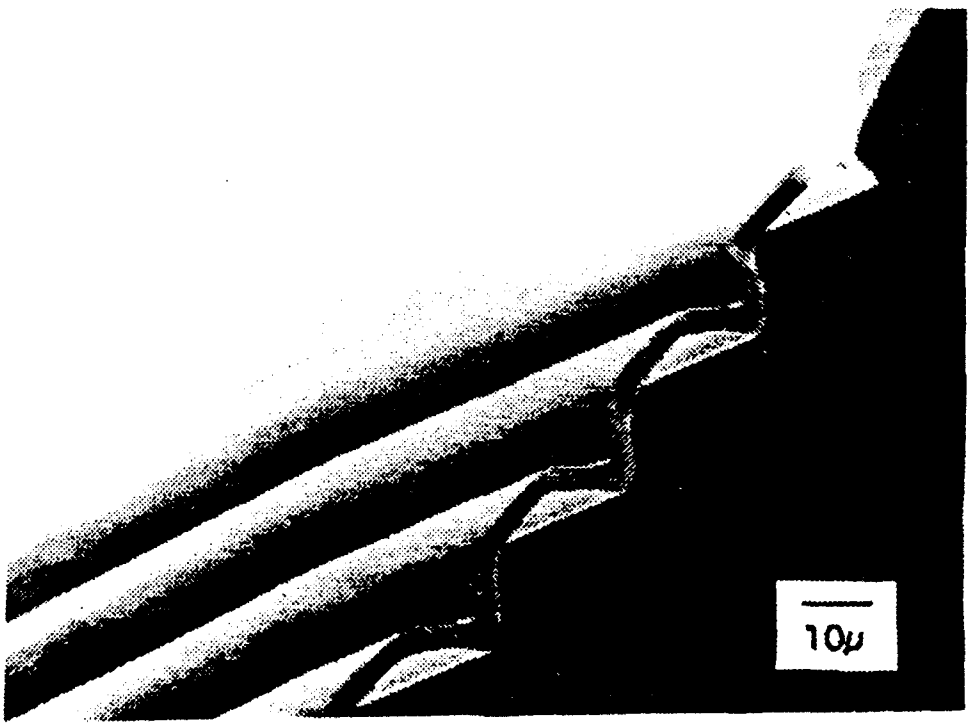

Figure 1.9: Detail of the corrugations.

The aspect of the final product can be appreciated in Fig. 1.8, which shows an SEM picture of the back-side view of the silicon diaphragm. Notice how well defined the structural features are, such as the corrugations and the vent holes, as well as the smooth, shiny, finish of the silicon. The diaphragms appear translucent, with an orange-red color. Fig. 1.9 shows an SEM picture of the cross-section of the diaphragm, where the depth and smoothness of the grooves that define the corrugations can clearly be appreciated. The diaphragms had a diameter of $3.2mm$, a boss ratio of 0.8, thickness of $3.5\mu m$, corrugation depth of $4.5\mu m$, corrugation width of $20\mu m$ and vent holes of $100\mu m$ in diameter.

The FPC is formed by bonding together a mirrored diaphragm with a metallized pyrex substrate. Since this arrangement has to be conductive all around for it to act as a Faraday cage as well as partially transmitting so that light can be coupled in and out of the cavity, it becomes necessary to have two distinct metal layers on the same glass substrate, each one with a different thickness. A thin (60Å), partially-transmitting, Al film on the center and a thick (1000Å), highly-conductive one, extending from the limits of the inner film out to the limits of the cavity.

For this application pyrex microscope cover slips, $1x1cm$ square, $300\mu m$ thick and polished flat to $5\lambda/in.$ were used. Pyrex glass is used because its coefficient of thermal expansion matches that of silicon and because it is suitable for the bonding process used in this work. However, any other sodium-bearing glass could be used. Cavities are bonded together using the anodic bonding technique [22]. The final assembly of the cavities requires mounting the bonded miniature FPC on the tip of an optical fiber, and the attachment of a GRIN lens, as seen in Fig 1.2.

Results

To determine the performance of the sensor under the effects of an external electric field, measurements of the reflected intensity were made for a probe placed inside and electric-field test cage especially built for this purpose. The test cage consisted of two parallel metallic plates separated by dielectric rods. The assembly was supported $1m$ above the ground and placed at least one meter away from any conducting surfaces. The plates were connected to the terminals of a $30KV$ DC power supply. In addition, sharp edges and corners were coated to prevent any possible corona effects. With this arrangement it was possible to generate uniform DC electric fields in the 0 to $300KV/m$ range.

Measurements made with probes under DC fields of up to $300KV/m$ showed no signs of electric discharge or corona effects. Reflected intensity measurements for different intensities of applied electric field were obtained using an arrangement similar to the one depicted in Fig. 1.3. Light from a white-light source is launched into one arm of a fused fiber coupler connected to the fiber probe, and the reflected light from the cavity is measured through the opposite arm of the fiber coupler by means of an optical spectrum analyzer. Fig. 1.11 shows the spectra for the reflected intensity with no field applied and with a field of $300KV/m$. Notice that the spectral shift in the resonance signature is towards longer wavelengths, which indicates that the cavity spacing is increasing as a function of field intensity as expected.

The operation of the sensor was determined using an LED emitting at $850nm$ source instead of white light. Measured spectra at different applied field intensities are shown in Fig. 1.12. Notice again that the cavity's diaphragm does indeed deflect under the influence of the external field and that this deflection brings upon a change in the reflected spectrum of the LED. As expected, the relative intensity changes of the detected power increase as the square of the electric field. Furthermore, $40KV/m$ was the minimum field for which a deflection was observed. This is attributed to the residual stress present in the diaphragm due to the heavy boron-doping used in its fabrication. Diaphragms fabricated using a stress-free process such as the electrochemical etching process, will result in sensors with increased sensitivity.

Conclusions

A novel electric field sensor using a combination of Faraday cage and a micro Fabry-Perot interferometer mounted on the tip of an optical fiber has been demonstrated.

Electric fields in the range of 0 to $300KV/m$ were successfully measured. The minimum intensity detected was of the order of $40KV/m$. This relatively low sensitivity is due to the high stiffness of the diaphragm arising from the high boron-diffusion. However, higher sensitivities are possible by thinning the diaphragm, increasing the radius, reducing the

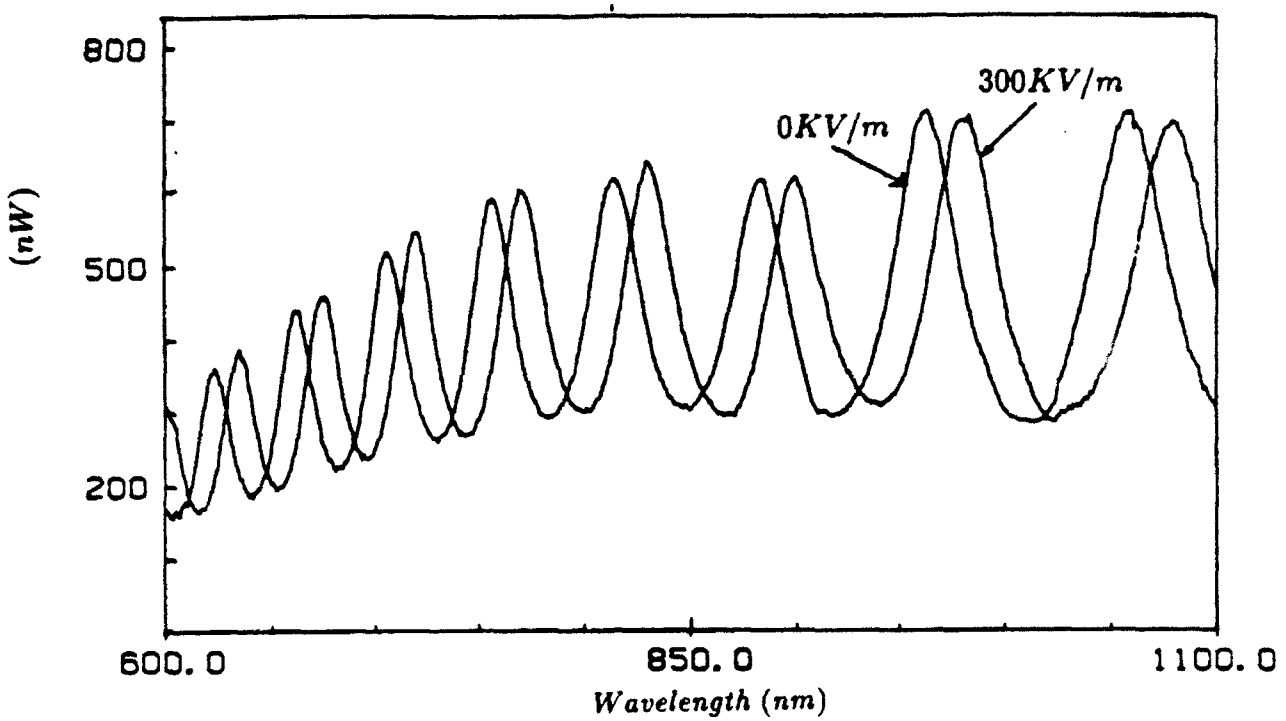

Figure 1.10: Reflected intensity with no field and with a field of $300KV/m$

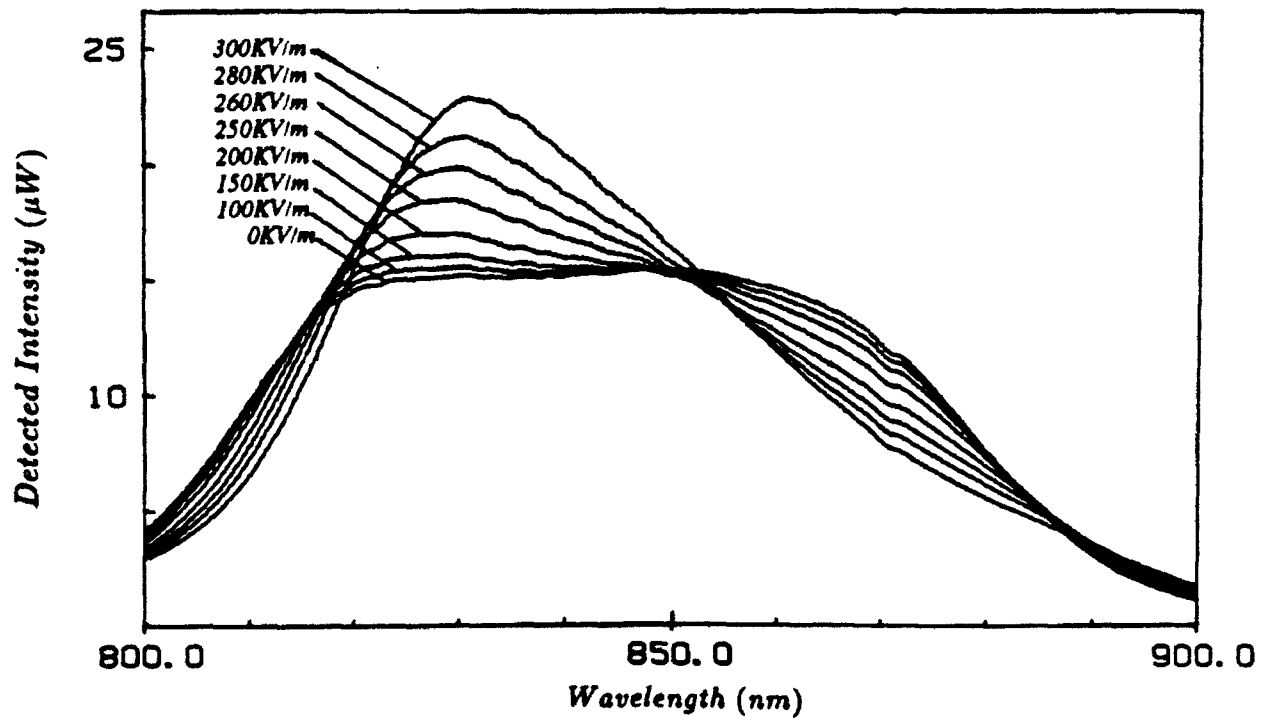

Figure 1.11: Measured reflected spectrum for different intensities of electric field.

Micromachined Fabry-Perot Interferometer with Corrugated Silicon Diaphragm for Fiber Optic Sensing Applications

A. Méndez and T. F. Morse
Laboratory for Lightwave Technology
Brown University, Providence, RI 02912

K. A. Ramsey
Batelle Memorial Institute
Columbus, Ohio 43201-2693

ABSTRACT

A new design for a miniature Fabry-Perot Interferometer (FPI) mounted on the tip of an optical fiber for sensing applications is presented. The Fabry-Perot Cavity (FPC) is formed by a micromachined corrugated silicon diaphragm anodically bonded to a pyrex substrate. In this way, this device takes advantage of the sensitivity and selectivity of an optical interferometer combined with the small size, lightweight and EMI immunity properties of optical fibers to create compact, lightweight and almost entirely dielectric sensors for the measurement of pressure, acceleration, sound, electric and magnetic field, etc. in remote, dangerous or inaccessible places. A discussion on the operation and fabrication of the FPC is given, along with experimental results obtained in its application as an electric field sensor.

INTRODUCTION

Since the reflectivity (or transmissivity) in a FPI is a unique function of the mirror separation, the medium's refractive index, and the wavelength of operation, it is possible to use it as a sensitive and selective transducer for a variety of physical measurands. Thus, by changing the cavity gap by the action of an external agent such as pressure or temperature, while keeping the other parameters constant, it is possible to obtain a shift in the fringe spectrum of the cavity. In the present case, this function is accomplished by a deformable, thin and corrugated silicon diaphragm. Therefore, under the influence of an external measurand, the central portion of said diaphragm (which acts as a cavity mirror) deflects, effectively changing the gap size and with it the intensity of the light reflected or transmitted by the cavity. Furthermore, the use of a corrugated diaphragm has also the advantage of increasing the range of linear deflection, improve the parallelism between the cavity mirrors as well as isolate the cavity from case stresses.

Several FPI utilizing thin *Si* diaphragms have been described in the past [1-5]. Most of them were used either as narrow band-pass filters for WDM applications in fiber optic systems, or as pressure transducers. Furthermore, fiber optic sensors based on modulating the backreflected light coming from a FPI attached to them have been investigated [6]. Sensors for the measurement of pressure [7-9], temperature [10] and refractive index [11] have been successfully developed.

SPIE Proceedings, Vol. 1793, No. 16, Integrated Optics and Microstructures, Boston, MA, 1992.

There are two basic types of operation for these sensors depending on the size of the cavity gap [12]. Large-cavity sensors ($> 5\mu m$) have a multi-cycle operation and thus rely on fringe counting techniques for the determination of the measurand. And short-cavity sensors ($< 5\ \mu m$) having a spectral width comparable to a single fringe. Thus, any shifts of the resonance peak can be directly related to the magnitude of the parameter of interest. Obviously, the former type experience large mirror separations of the order of several μm, while the latter require displacements of less than a μm. The FPC used in this work is of the shallow-cavity type because its compatibility with a simpler detection scheme as opposed to the cumbersome and ambiguous fringe counting circuits associated with a large-cavity FPI.

Fig. 1 depicts the Fabry-Perot cavity (FPC) design. The cavity is formed by a suspended, thin and corrugated silicon diaphragm bonded to a glass substrate. A metallic film on the surface of the silicon diaphragm acts as one of the cavity mirrors, while a thin, partially transmitting, aluminum film on the substrate constitutes the other. The structure is mounted on the tip of a 100/140 μm multimode optical fiber onto which a GRIN lens has been previously attached (see Fig. 2).

The operation of a fiber sensor using one such FPI is very simple. As the gap separation in the cavity changes under the influence of the measurand, the intensity of the backreflected light into the fiber changes accordingly. The spectral shift of the interferometer peak can be interrogated using an LED which translates the cavity's shifts into intensity variations of the LED light spectrum, thus yielding a spectrally modulated envelope. To make the sensor immune to variations in light intensity due to bending or transmission losses, as well as any possible degradation of the light source, a dual-wavelength referencing technique is used (see Fig. 3). In this fashion, two specific wavelengths are selected out of the LED's broad spectrum by narrow bandpass optical filters, and their intensities are measured using optical detectors. The magnitude of the measurand is thus related to a change in the intensity ratio at these two wavelengths.

Next, we will discuss the operation and fabrication of the FPI used in this work, along with a summary of the results obtained in its implementation as a fiber-optic electric field sensor.

ANALYSIS OF OPERATION

- *The Fabry-Perot Interferometer*

A FPI is an optical resonator cavity consisting of two, partially transmitting, parallel mirrors separated a distance d (see Fig. 4). When a collimated, monochromatic, beam of light I_0 is incident upon the cavity at an angle θ, a series of multiple reflections of the transmitted beam will take place within the cavity. Outside the cavity, a series of beams of diminishing amplitudes emerge on each side of the mirrors. These output beams interfere constructively with one another, resulting in a net reflected light intensity I_r in the direction of the light source, and a net transmitted intensity I_t, directed away from the source. The ratio of the reflected intensity *to the incident intensity can be obtained by the superposition of the fields for each beam, which results in [13]:

$$\frac{I_r}{I_0} = \frac{(\sqrt{R_1} - \sqrt{R_2})^2 + 4\sqrt{R_1 R_2}\sin^2(\frac{\delta}{2})}{(1 - \sqrt{R_1 R_2})^2 + 4\sqrt{R_1 R_2}\sin^2(\frac{\delta}{2})} \tag{1.1}$$

where R_1 and R_2 are the mirror reflectivities, and δ is the phase difference between two successive beams:

$$\delta = \frac{4\pi}{\lambda} nd\cos\theta \tag{1.2}$$

*Since our sensor design is based on the reflected intensity, we will focus our attention on I_r alone. However, a similar analysis can be made for the case of I_t.

where n is the index of refraction of the medium between the mirrors, d is the cavity spacing, θ the incidence angle, and λ the wavelength of the light in vacuum.

The behavior of $\frac{I_r}{I_0}$ as a function of phase difference δ is shown for different values of $R = \sqrt{R_1 R_2}$ in Fig. 5. The spectrum consists of a series of resonant reflection peaks that occur whenever the cavity spacing equals an integer multiple of $\frac{\lambda}{2}$ of the incident light. Hence, according to eq. 1.1, I_r will be a maximum whenever $\delta = m\frac{\pi}{2}$ with $m = 1, 2, 3, ...$, and a minimum whenever $\delta = m\pi$. The parameter m is known as the interference order and is an indication of how many fringes have occurred from a zero cavity spacing up to a spacing d. It is defined by:

$$m = \frac{\delta}{2\pi} = \frac{2nd\cos\theta}{\lambda} \tag{1.3}$$

Notice from Fig. 5 that the reflection peaks are more pronounced and narrower whenever R is large, while they become broad and almost sinusoidal in shape for small R. Furthermore, High values of R result in peaks with a greater modulation depth, as opposed to cavities with low values of R. The modulation depth or contrast c is a measure of the ratio between the maximum and the minimum reflected intensities as given below:

$$c = \frac{I_{rmax}}{I_{rmin}} = \left(\frac{1+\sqrt{R_1R_2}}{1-\sqrt{R_1R_2}}\right)^2 \tag{1.4}$$

The separation between peaks, $\Delta\lambda$, is known as the free spectral range (FSR) of the cavity, and is given by:

$$\Delta\lambda = \frac{\lambda^2}{2nd\cos\theta} \tag{1.5}$$

Each peak possesses a bandwidth, $\Delta\lambda_{\frac{1}{2}}$, at full width half maximum (FWHM) of:

$$\Delta\lambda_{\frac{1}{2}} = \frac{2\lambda}{\pi m}\arccos\left(\frac{1-\sqrt{R_1R_2}}{2(R_1R_2)^{\frac{1}{4}}}\right) \tag{1.6}$$

It is important to note that the width of the peaks depends only upon R, while their position is determined by the mirror separation d and λ. Therefore, both the spectral range and the bandwidth can be tailored independently of each other. The ratio between $\Delta\lambda$ and $\Delta\lambda_{\frac{1}{2}}$ is known as the Finesse, F, of the cavity.

Since the cavity design employs semi-reflective metallic coatings for mirrors, which inevitably absorb light, the expression for I_r is no longer accurate and has to be modified to take into account the effects of mirror absorption and the phase retardations incurred upon reflection. The modified expression for I_r has the form [14]:

$$\frac{I_r}{I_0} = \frac{(\sqrt{R_1} - g\sqrt{R_2})^2 + 4g\sqrt{R_1R_2}\sin^2\left(\frac{\delta+\phi_2-\phi_1^R+\phi_T}{2}\right)}{(1-\sqrt{R_1R_2})^2 + 4\sqrt{R_1R_2}\sin^2\left(\frac{\delta+\phi_2+\phi_1^L}{2}\right)} \tag{1.7}$$

with

$$g = \left|R_1\exp^{j(\phi_1^L+\phi_1^R)} + T_1\exp^{2j\phi_T}\right| \tag{1.8}$$

where g is a parameter that represents the amount of light not absorbed by the front mirror (1-A); ϕ_1^R is the phase change upon reflection from the front mirror for a beam traveling away from the source; ϕ_1^L is the phase change upon reflection from mirror 1, for a beam traveling towards the source; ϕ_2 is the phase change upon reflection from the rear mirror, and ϕ_T is the phase change introduced upon crossing the first mirror. These parameters can be computed using the following expressions [13]:

$$\phi_1^R = \arctan\left(\frac{2k_{Al}\, n_{glass}}{n_{Al}^2 + k_{Al}^2 - n_{glass}^2}\right) \tag{1.9}$$

$$\phi_1^L = \arctan\left(\frac{2k_{Al}\, n_{air}}{n_{Al}^2 + k_{Al}^2 - n_{air}^2}\right) \tag{1.10}$$

$$\phi_2 = \phi_1^L \tag{1.11}$$

$$\phi_T = \phi_{glass-Al}^T + \phi_{Al-air}^T + \beta_{Al} \tag{1.12}$$

$$= \arctan\left(\frac{-k_{Al}}{n_{glass} + n_{Al}}\right) + \arctan\left(\frac{k_{Al}\, n_{air}}{n_{Al}^2 + k_{Al}^2 n_{Al} n_{air}}\right) + \frac{2\pi n_{Al} t_{Al}}{\lambda} \tag{1.13}$$

where n and k are the refractive index and extinction coefficient, respectively, for a given medium (aluminum film, glass or air). The effect of these additional phase terms is equivalent to an increase $\frac{\phi\lambda}{2\pi}$ in the optical spacing of the cavity. In addition, the maxima of the spectrum will decrease due to the absorption in the metal films.

• *Deflection of a Corrugated Diaphragm*

Since a corrugated Si diaphragm is used to transduce the measurand of interest into a mechanical deflection which subsequently will change the gap separation of the FPC, it becomes necessary to discuss the behavior of flat and corrugated diaphragms both in the linear and nonlinear regimes.

A diaphragm may be viewed as a spring element which deflects by the application of a load. The resistance to loading is due to bending, tensile forces, and pre-stresses in the diaphragm. The deflection at the center of a flat circular plate is given as [15]:

$$\frac{Pa^4}{Et^3} = \frac{16}{3(1-\nu^2)}\left(\frac{y}{t}\right) + \frac{8}{3(1-\nu^2)}\left(\frac{y}{t}\right)^3 \tag{1.14}$$

where P is the applied pressure, y the deflection, t the diaphragm thickness, a the diaphragm radius, E is Young's modulus and ν is Poisson's ratio.

Notice that Eq. 1.14 has both a linear and a nonlinear deflection terms. When the applied load is entirely supported by bending, the resulting deflection is linear. If, on the other hand, a portion of the applied load is resisted by a restoring force caused by stretching of the diaphragm, then the center deflection becomes nonlinear. The nonlinear behavior is noticeable in thin plates for which, when the deflection is larger than about half the thickness, the middle surface becomes appreciably strained giving rise to tension forces in the diaphragm. Furthermore, the deflection of flat diaphragms is not uniform across its radius, but rather the medium plane changes into the shape of a surface of revolution with characteristically defined inflection points.

In order to obtain a linear response for a greater range of deflection, a series of corrugations are incorporated on the surface of the diaphragm. A corrugated diaphragm is made by forming concentric convolutions or corrugations on the plane of a thin flat plate. The profile of the corrugations has little influence on the performance characteristics of the diaphragm and may even have different shapes such as sinusoidal, trapezoidal, triangular, rectangular or toroidal. However, the stiffness and the range of linear deflection may be altered by the depth and number of the corrugations.

In general, the introduction of corrugations increases the range of linear deflection at the expense of increasing considerably the rigidity of the diaphragm. Therefore, in order to obtain a deflection comparable to an equivalent flat

diaphragm (same thickness, material and radius), an increase in the applied load will be necessary. However, if the deflection of a flat diaphragm is compared to that of a corrugated one of the same flexibility (not necessarily the same radius or thickness) the corrugated one displays a greater range of linear deflection.

The load-deflection relation for a corrugated diaphragm is given as [16]:

$$\frac{Pa^4}{E't^4} = A_p\left(\frac{y}{t}\right) + B_p\left(\frac{y}{t}\right)^3 \tag{1.15}$$

with

$$A_p = \frac{2(q+3)(q+1)}{3(1-\frac{\nu^2}{q^2})} \tag{1.16}$$

$$B_p = \frac{32}{q^2-9}\left(\frac{1}{6} - \frac{3-\nu}{(q-\nu)(q+3)}\right) \tag{1.17}$$

and for sinusoidal corrugations

$$q = \left(\frac{s}{l}\right)\sqrt{1+\frac{H^2}{t^2}} \tag{1.18}$$

where $E' = \frac{E}{(1-\nu)}$ and q is the corrugation quality factor, H the corrugation depth, s the corrugation arc length and l the spatial period (see Fig. 6). The value of q is a figure of merit that determines the deflection characteristics of the diaphragm. A high value of q implies a long range of linear displacement, as well as a high rigidity. Low values of q indicate a performance approaching that of a flat diaphragm for which $q = 1$. Furthermore, for the case of shallow corrugations, the corrugation period l has little effect since $\frac{s}{l} \approx 1$.

At times it is desirable to have a small flat region, or center boss, in the diaphragm. This is particularly useful in structures like actuators and movable mirrors (as with the present case). Small deflections of a bossed, corrugated, diaphragm were developed by Haringx [17] who expressed them as follows:

$$y = \epsilon\frac{3Pa^4}{16E't^3} \tag{1.19}$$

with

$$\epsilon = \frac{8(1-r^4)}{(q+3)(q+1)}\left(1 - \frac{8qr^4(1-r^{q-1})(1-r^{q-3})}{(q-1)(q-3)(1-r^4)(1-r^{2q})}\right)\left(\frac{s}{l}\right) \tag{1.20}$$

where r is the boss to diaphragm radius ratio (R_b/a). The parameter ϵ is known as the coefficient of reduction and physically represents the stiffening that a comparable flat diaphragm has acquired by the introduction of corrugations. In other words, the magnitude of ϵ ranges from one to zero. Hence, diaphragms with large inner rims and deep corrugations are extremely rigid. Conversely, smaller inner rims combined with shallow corrugations result in more flexible diaphragms.

Corrugated silicon diaphragms have been successfully fabricated and used in applications such as pressure sensors, micro-actuators and interferometers [18,19]. Typically, corrugations have been produced by etching grooves in the surface of a silicon wafer and then diffusing an etch-stop. The process is completed when the corrugations are defined by a deep etching on the opposite side of the wafer.

• *Dynamic Response*

The principal factors which govern the dynamic response characteristics of the sensor are the stiffness of the diaphragm, and the stiffness and damping resistance of the air-filled space inside the FPC.

When the diaphragm deflects it sets in motion the thin film of air inside the cavity. This airflow introduces forces that modify the mechanical stiffness and resistance coefficients of the cavity, which control the response of the transducer. This situation is very similar to that encountered in a condenser microphone. Therefore, the theory behind the dynamic properties of thin air films have been previously investigated to asses their impact on the performance of condenser microphones [20].

As the sensor's diaphragm moves, air is forced radially out of the cavity [†] resulting in a resistive force (due to the viscosity of the air) which opposes the motion of the diaphragm. In addition, there is a simple compression of the entrapped air which results in an elastic restoring force on the diaphragm. At very low frequencies, the air is able to flow out of the gap, and consequently the dominant mechanism is due to frictional forces introduced by the large airflow while the elastic forces due to air compression are negligible. Conversely, at high frequencies, there is little flow and hence larger compressive forces, while the resistive forces are minimal. The frequency-dependent magnitudes of the total damping resistance c, and stiffness k_a of the air film can be calculated from the following expressions [20]:

$$c(\omega) = \frac{2\pi a P_a}{\omega \alpha d}\left[\frac{bei(\alpha a)\ bei'(\alpha a) + ber(\alpha a)\ ber'(\alpha a)}{ber^2(\alpha a) + bei^2(\alpha a)}\right] \tag{1.21}$$

$$k_a(\omega) = \frac{\pi a^2 P_a}{d}\left[1 - \frac{2}{\alpha a}\frac{ber(\alpha a)\ bei'(\alpha a) - ber'(\alpha a)\ bei(\alpha a)}{ber^2(\alpha a) + bei^2(\alpha a)}\right] \tag{1.22}$$

with

$$\alpha = \frac{12\nu\omega}{P_a d^2} \tag{1.23}$$

where P_a is the atmospheric pressure, a is the radius of the diaphragm, d the cavity spacing, and ν the air viscosity. As before, for frequencies near zero K_a vanishes, while c simplifies to the following:

$$c = \frac{3}{2}\frac{\pi\nu a^2}{d^3} \tag{1.24}$$

The actual response of the sensor is obtained by modeling it as a second-order system with frequency-dependent damping and stiffness. In this fashion, when a force $F\cos(\omega t)$ acts on the diaphragm, the resulting displacement can be determined from the equation of motion for the system that is,

$$m\ddot{x} + c\dot{x} + (k_a + k_d) = F\cos(\omega t) \tag{1.25}$$

where k_d is the stiffness of the diaphragm. The net displacement amplitude X can be obtained by solving Eq. 2.95, obtaining the following expression [21]:

$$X = \frac{F}{\{(k_a + k_d) - m\omega^2\} + jc\omega} \tag{1.26}$$

[†] This airflow is free to escape the cavity through a series of minute vent holes provided on the rim area of the diaphragm. The vent holes are also used to maintain the cavity at atmospheric pressure, thus avoiding any pressure differentials from introducing any errors on the measurements, except in the case of a pressure transducer where their use might be precluded.

Under static conditions ($\omega = 0$), k_a is negligible and, although the airflow damping resistance c might reach high values, its actual contribution to the system as a whole is zero, so that the static deflection simply becomes

$$X_{st} = \frac{F}{k_d} \tag{1.27}$$

At high frequencies the response of the system is highly dependent on the air's damping and stiffness effects. The detrimental influence of these effects can be minimized by facilitating the flow of the entrapped air film by means of holes or deep channels on the surface of the cavity substrate.

Another important aspect of the dynamic response behavior of this system, is its temporal transient response which describes how the system reacts to and follows a unit-step input. The unit-step response $x(t)$ for this system has the form:

$$x(t) = 1 - \frac{\exp(-\zeta\omega_n t)}{\sqrt{1-\zeta^2}} \sin\left(\omega_d t + \arctan\frac{\sqrt{1-\zeta^2}}{\zeta}\right) \tag{1.28}$$

where

ω_n = natural frequency of the system $\left(\sqrt{\frac{k_d}{m}}\right)$

ω_d = damped natural frequency of the system $(\omega_n\sqrt{1-\zeta^2})$

ζ = damping ratio $\left(\frac{c(\omega)}{c_{cr}} = \frac{c(\omega)}{2m\omega_n}\right)$

Eq. 1.28 above indicates that the transient step-response of this type of system consists of either free or damped oscillations at a frequency ω_d. That is, if $\zeta = 0$, the system oscillates at its natural frequency ω_n. However, if the linear system has any amount of damping, the oscillations occur a a much lower frequency than ω_n, decaying exponentially in time. For the case of an overdamped system ($\zeta > 1$), the oscillations are non-existing and the response of the system varies exponentially with time. The time required for the output response to reach and stay within a given range of the initial value is known as the settling time τ_s. For overdamped systems, $\tau_s \approx \frac{6}{\zeta\omega_n}$ for a 2% tolerance band.

FABRICATION

A wide variety of corrugated Si diaphragms having different radii, boss-ratio, thickness and number of vent holes, were fabricated using standard photolithographic and silicon micromachining techniques [22-24]. Next, we will describe the fabrication process in more detail.

First, a small circular recess $1.7\mu m$ deep is etched on the epi side of a n-type, (100) Si wafer, using a solution of KOH:DI:IPA (900gm:900ml:360ml) at 80^0C for 2.5 minutes (see Fig. 7a). Subsequently, a series of concentric grooves, $5\mu m$ deep, are plasma-etched using a gas mixture of $CF_4 : O_2$ (10:1) at a pressure of approximately $400mT$ and $300W$ of power. These grooves will define the top side of the corrugations (see Fig. 7b).

A thick ($1.2\mu m$) thermal oxide layer is grown on the wafer to mask against the boron diffusion and to allow the patterning of the back side for the deep anisotropic etching. This oxide mask is photolithographically patterned to define circles of $100\mu m$ in diameter around the periphery of the recess. These oxide dots will block the subsequent boron diffusion, thus allowing the etch to attack the silicon all the way through in these regions. At this point, a heavy boron diffusion is introduced at a temperature of 1175^0C to act as an etch-stop. The diffusion time varied from 25 minutes (for a $3\mu m$ thickness), to 33 minutes ($3.5\mu m$), up to 1 hour ($5\mu m$). After the boron diffusion, the wafers are briefly etched in

a solution of HF:DI (1:1) to remove the borosilicate glass that developed from the diffusion (see Fig. 7c).

To complete the processing, a deep etching on the backside of the wafer is made using an EDP solution (ethylene-diamine, pyrocatechol and water) at 110^0C for 5 hours. Since the boron diffusion follows the contour of the epitaxial features on the wafer, a thin, corrugated, Si diaphragm with a thickness dependent on the depth of the boron diffusion will be obtained after the backside etching is completed (see Fig. 7d). Finally, the wafers are thoroughly rinsed and the remaining oxide layer removed in buffered HF.

The final aspect of the diaphragms can be appreciated in Fig. 8, which shows SEM photographs of different versions of corrugated diaphragms, including one with a central mesa. Notice how well defined the structural features are, as well as the smooth shiny finish of the silicon. The diaphragms appear translucent with an orange-red color. They are also straight and taut due to the heavy boron doping and, for the most part, they seem relatively rugged. However, they easily shatter or break if punctured or touched abruptly.

The FPC were formed by bonding together a mirrored diaphragm with a metallized pyrex substrate. For this application, $1cm$ square pyrex microscope cover slips, $300\mu m$ thick and polished flat to $5\lambda/in$, covered with a thin ($60\mathring{A}$), partially transmitting film, were used. Cavities were permanently bonded using the anodic bonding technique [25]. The bonded FPC were mounted on the tip of a multimode fiber ($100/140\mu m$) where a GRIN lens was previously attached to, as depicted in Fig. 2.

EXPERIMENTAL RESULTS

The reflected intensity spectra for assembled FPI was measured using an arrangement similar to the one depicted in Fig. 3. Light from a white-light source was launched into one arm of a fused fiber coupler connected to the fiber probe, and the reflected light from the cavity is measured through the opposite arm of the fiber coupler by means of an optical spectrum analyzer. Fig. 9a shows a typical spectrum in the 600 to $1100nm$ range for an undeflected FPC with a $5\mu m$ gap and $R_1 = 0.2$ and $R_2 = 0.8$. The spectrum is characterized by smooth and well defined interference cycles. However, there is a broadening effect that results in "rounder" aspect of the minima regions, which is not characteristic of typical FPC spectra. This effect is a consequence of the phase changes introduced by the metallic films upon reflection that modify the characteristics of the reflected intensity as confirmed by the calculated reflection spectrum shown in Fig. 9b. Obtained using Eq. 1.7 and the same cavity parameters.

Another important aspect observed in the course of these measurements, was the sensitivity of the alignment between the FPC and the GRIN lens. It was noticed that in some instances optical interference was not observed for the cavity when a GRIN lens was used. This can be attributed to either a "run-away" effect in the cavity (where the multiple reflected beams do not interfere properly with one another because of spatial shifts introduced by skews rays), or by improper re-launching of the light back into the fiber due to a fiber misalignment with respect to the GRIN lens, or perhaps due to lack of parallelism between the mirrors over the area of the GRIN lens ($1.8mm$ in diameter). This latter explanation seems to be a plausible one, since in experiments relying exclusively on the coupling between the multimode fiber and the cavity, interference was observed with an adequate amount of reflected intensity.

To demonstrate the proof-of-principle of the FPC, a novel electric field sensor was constructed using a combination of a Faraday cage and the miniature FPI described here. By constructing the FPC as a conductive Faraday cage, external electric fields can be detected by the electrostatic forces they exert on the top surface of the cavity's diaphragm. Thus, as the gap in the cavity increases, under the influence of the negative electrostatic pressure induced by the external field, the intensity of the backreflected light into the fiber will change accordingly (consult reference [26] for more details on the operation of this sensor).

Measurements of reflected spectra were made with a probe placed inside and electric-field test cage consisting of two parallel metallic plates separated by dielectric rods and connected to the terminals of a variable $30KV$ DC power supply.

Reflected intensity spectra, for different intensities of applied electric field, were obtained using an LED emitting at $850nm$ as a source. Measured spectra at different applied field intensities are shown in Fig. 10. Notice that the cavity's diaphragm does indeed deflect under the influence of the external field and that this deflection brings upon a change in the reflected spectrum of the LED. Furthermore, $40KV/m$ was the minimum field for which a deflection was observed. This is attributed to the residual stress present in the diaphragm due to the heavy boron-doping used in its fabrication. Diaphragms fabricated using a stress-free process such as the electrochemical etching process, will result in sensors with increased sensitivity.

CONCLUSIONS

A new design for a miniature FPI mounted on an optical fiber for sensing applications has been demonstrated. The present device combines optical fibers with silicon micromachining techniques to render a new family of fiber optic sensors that offer small size, lightweight, EMI immunity as well as high sensitivity for the detection of a variety of measurands.

The optical and mechanical characteristics of the FPI have been analyzed in some detail, and their potential application demonstrated in the form of an electric field sensor. DC electric fields in the range of 0 to $300KV/m$ have been successfully measured. The minimum field strength detected was of the order of $40KV/m$. This relatively low sensitivity is due to the high stiffness of the diaphragm arising from the high boron-diffusion. However, higher sensitivities are possible by thinning the diaphragm, increasing the radius, reducing the boss ratio or decreasing the corrugation depth.

ACKNOWLEDGEMENT

The authors wish to thank S. Cho for helpful discussions on silicon micromachining.

REFERENCES

1. Guckel, H. et al., "Electromechanical Devices Utilizing Thin Si Diaphragms", Appl. Phys. Lett., Vol. 31, No. 9, pp. 618-619, 1977.

2. Jerman, J. H. and Mallinson, S. R., "A Miniature Fabry-Perot Interferometer Fabricated Using Silicon Micromachining Techniques", Technical Digest of the 1988 IEEE Solid-State Sensors Workshop.

3. Jerman, J. H., Clift, D. J. and Mallinson, S. R., "A Miniature Fabry-Perot Interferometer with a Corrugated Silicon Diaphragm Support", Sen. Act., Vol. A 29, pp. 151-158, 1991.

4. Halg, B., "A Silicon Pressure Sensor with an Interferometric Optical Readout", Proc. Transducers '91 Conf., San Francisco, CA, June 1991, pp. 682-684.

5. Raley, N. F., Ciarlo, D. R., Koo, J., Beiriger, B., Trujillo, J., Yu, C., Loomis, G., and Chow, R., "A Fabry-Perot Microinterferometer for Visible Wavelengths", Technical Digest of the 1992 IEEE Solid-State Sensor and Actuator Workshop, June 1992, Hilton Head, SC.

6. Cox, E. R. and Jones, B. E., "Fibre Optic Colour Sensors Based on Fabry-Perot Interferometry", Proc. First International Conference on Optical Fiber Sensors, London, England, 1983.

7. Lieberman, R. A. and Blonder, G. E., "An Improved Interferometric Pressure Optrode", SPIE Proc., Vol. 838, pp. 49-59, 1987.

8. Dakin, J. P., Wade, C. A. and Withers, P. B., "An Optical Fibre Sensor for the Measurement of Pressure", Fiber and Int. Opt., Vol. 7, pp. 35-40, 1988.

9. Wolthuis, R. A., Mitchell, G. L., Saaski, E., Hartl, J. C. and Afromowitz, M. A., "Development of Medical Pressure and Temperature Sensors Employing Optical Spectrum Modulation", IEEE Trans. Bio. Eng., Vol. 38, No. 10, pp. 974-981, 1991.

10. Beheim, G., Fristch, K., Tabib Azar, M., "Silicon-Etalon Fiber-Optic Temperature Sensor", SPIE Proc., Vol. 1169, pp. 504-511, 1989.

11. Saaski, E. W., Mitchell, G. L., Hartl, J. C., "Wide Range Sensing of Liquid Refractive Index", Proc. Optical Fiber Sensors '86 conf., paper FAA 5-1, pp. 361-364, 1988.

12. Mitchell, G. L., "A Review of Fabry-Perot Interferometric Sensors", Springer Verlag proceedings in Physics, Vol. 44, Optical Fiber Sensors, pp. 450-457, 1989.

13. Born, M. and Wolf, E., Principles of Optics, Pergamon Press, New York, 1984.

14. Hadley, L. N., and Dennison, D. M., "Reflection and Transmission Interference Filters", J. Opt. Soc. Am., Vol. 37, No. 6, pp. 451-465, 1947.

15. Timoshenko, S. and Woinowsky-Krieger, S., Theory of Plates and Shells, McGraw Hill, New York, 1959.

16. DiGiovanni, M., *Flat and Corrugated Diaphragm Design Handbook*, Marcel Dekker, Chapter 23, 1982.

17. Haringx, J. A., "The Rigidity of Corrugated Diaphragms", Appl. Sci. Res., Vol. A2, pp. 299-325, 1950.

18. Mallon, J. R. and Kurtz, A. D., "Transducer Apparatus Employing Convoluted Semiconductor Diaphragms", U.S. *Patent 4,467,656, 1984.*

19. Jerman, J. H., "The Fabrication and Use of Micromachined Corrugated Silicon Diaphragms", Sens. Act., A21-A23, pp. 988-992, 1990.

20. Crandall, I. B., "The Air-Damped Vibrating System: Theoretical Calibration of the Condenser Transmitter", Phys. Rev., Vol. 11, pp. 449-460, 1918.

21. Rule, E., Suellentrop, J. and Perls, T. A., "Second-Order Instrumentation Systems with Frequency-Dependent Stiffness and Damping", J. Acoust. Soc. Am., Vol. 31, pp. 457-462, 1959.

22. Petersen, K. E., "Silicon as a Mechanical Material", Proc. IEEE, Vol. 70, No. 5, pp. 420-457, 1982.

23. Delapierre, G., "Micro-Machining: A Survey of the Most Commonly Used Processes", Sens. Act., Vol. 17, pp. 123-138, 1989.

24. Bassous, E., "Fabrication of Novel Three-Dimensional Microstructures by the Anisotropic Etching of (100) and (110) Silicon", IEEE Trans. Elect. Dev., Vol. ED-25, No. 10, pp. 1178-1185, 1978.

25. Wallis, G. and Pomerantz, D. I., "Field Assisted Glass-Metal Sealing", J. Appl. Phys., Vol. 40, No. 10, pp. 3946-3949, 1969.

26. Méndez, A., Morse, T. F. and Ramsey, K., "Fiber Optic Electric-Field Microsensor", Proc. SPIE, Vol. 1795, No. 17, Fiber Optic and Laser Sensors X, Boston, MA, 1992.

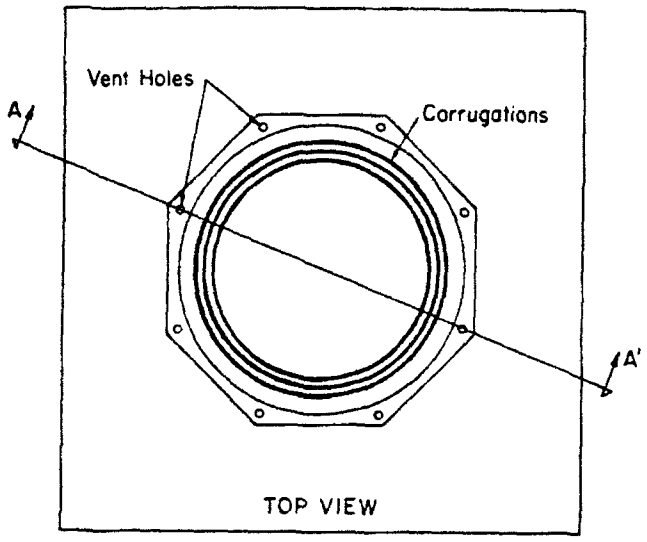

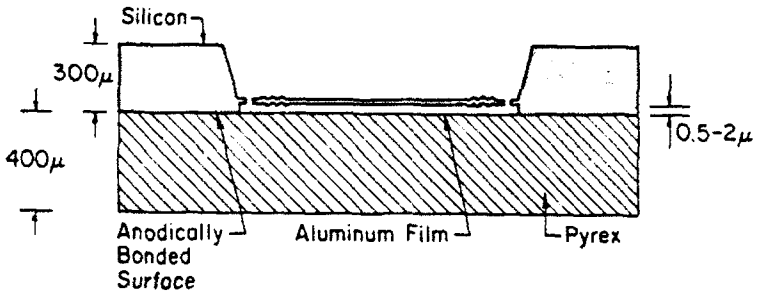

Figure 1: Fabry-Perot microcavity

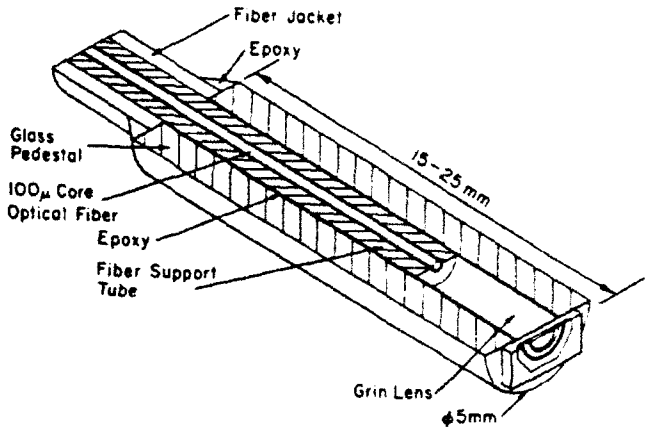

Figure 2: Mounting of sensor cavity on an optical fiber

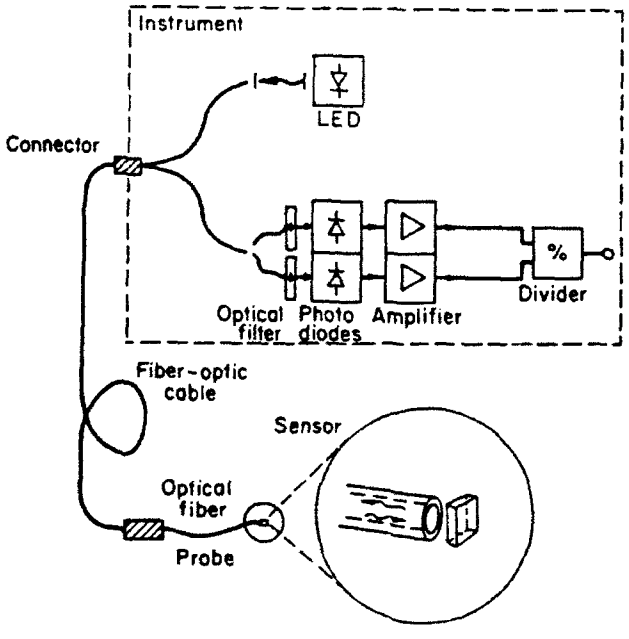

Figure 3: Sensor system schematic

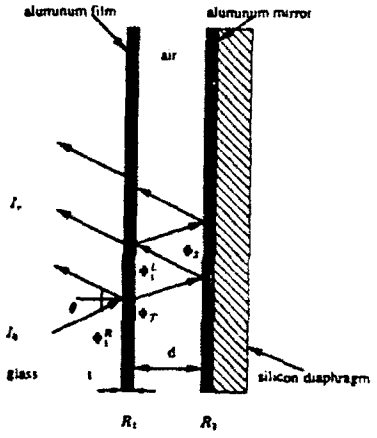

Figure 4: Fabry-Perot interferometer

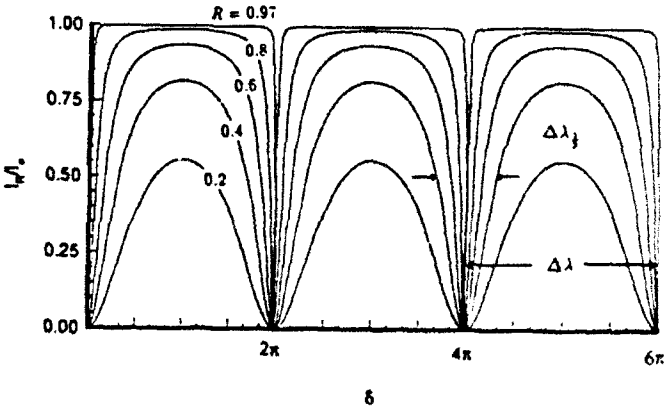

Figure 5: Fabry-Perot cavity reflected spectrum

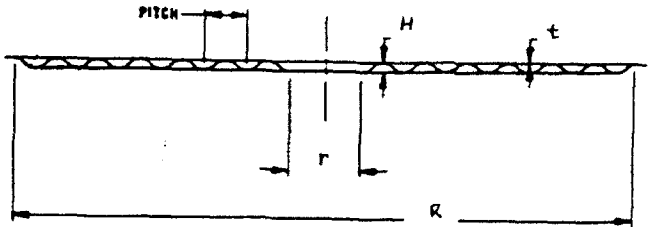

Figure 6: Profile of a corrugated diaphragm

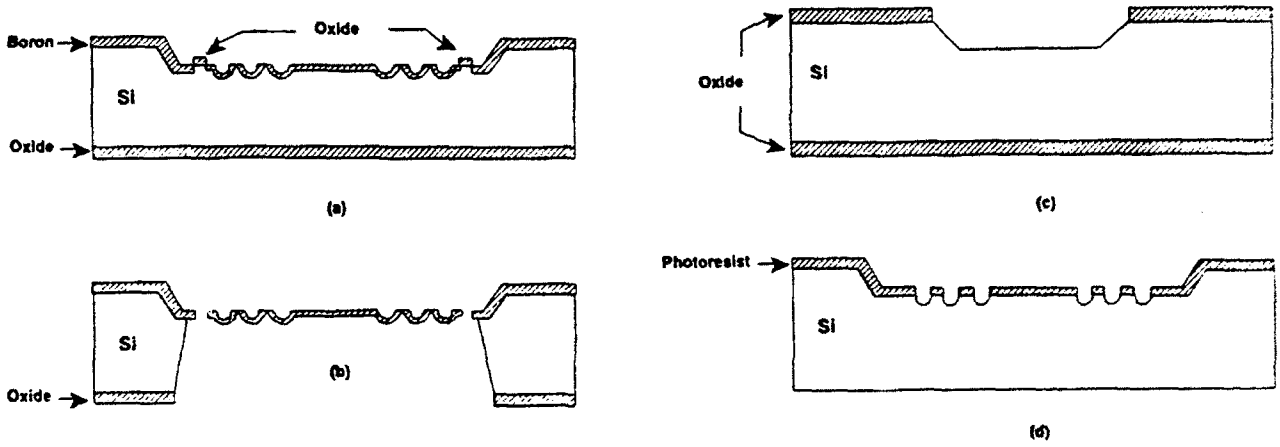

Figure 7: Micromachined corrugated silicon diaphragm fabrication process

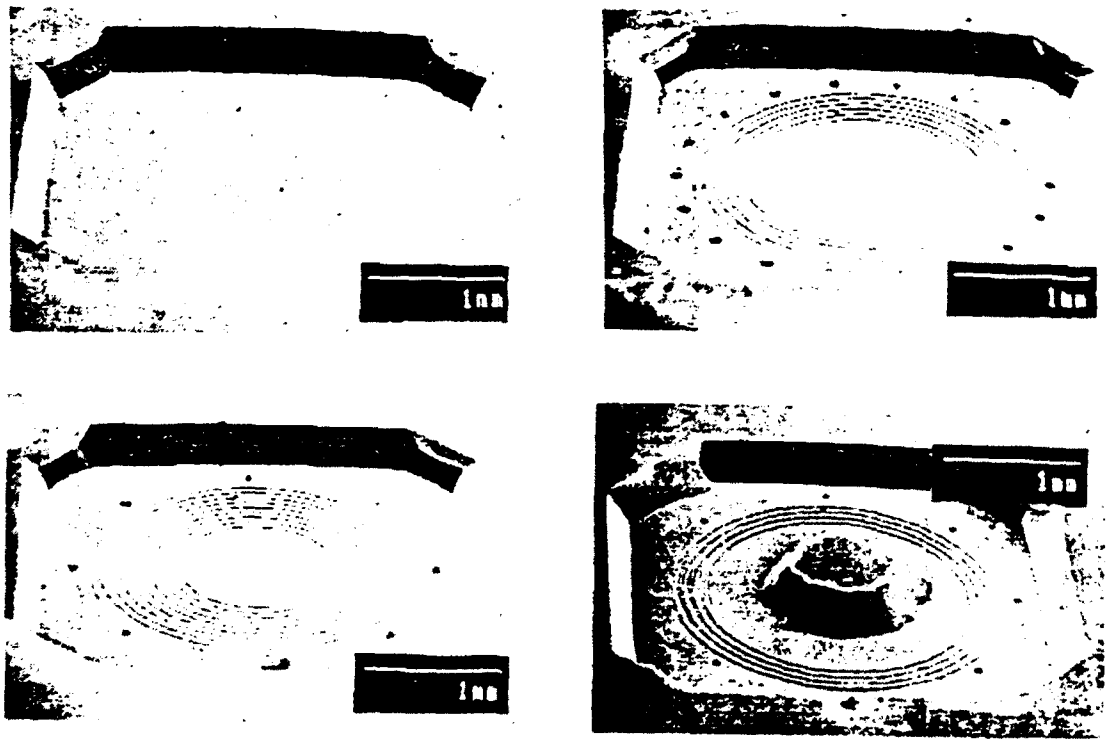

Figure 8: SEM photographs of various micromachined silicon diaphragms

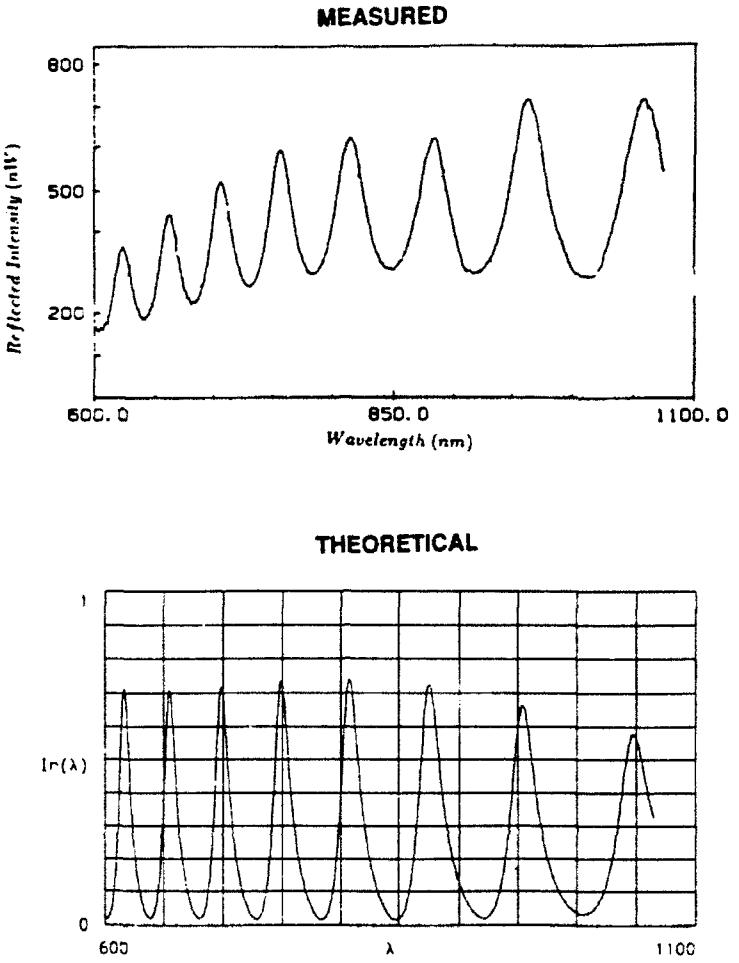

Figure 9: a) Measured FPC reflected spectrum and b) Calculated reflected spectrum using Eq. 1.7

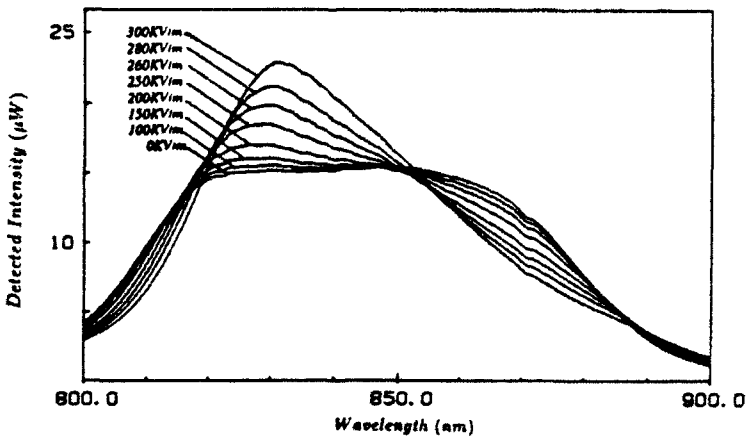

Figure 10: Measured reflected spectra for different intensities of electric field.

Journal of Non-Crystalline Solids 149 (1992) 229–242
North-Holland

JOURNAL OF NON-CRYSTALLINE SOLIDS

Spectroscopic analysis of a Eu-doped aluminosilicate optical fiber preform

Kyunghwan Oh [a], T.F. Morse [b], L. Reinhart [b], A. Kilian [b] and W.M. Risen Jr. [c]

[a] Department of Physics, [b] Division of Engineering, Laboratory for Lightwave Technology and [c] Department of Chemistry, Brown University, Providence, RI 02912, USA

Received 1 November 1991
Revised manuscript received 8 June 1992

An optical fiber whose core is an aluminosilicate glass doped with Eu^{+2} and Eu^{+3} ions has been made using modified chemical vapor deposition and a novel aerosol delivery technique. The UV–visible absorption of the preform has been studied in the 200–700 nm range as well as the excitation and emission spectra between 250 and 720 nm. Three broad UV absorption bands with maxima at 255, 302 and 316 nm have been observed. The relative intensities of fluorescence and the transition probabilities from the $^5D_0$ levels of Eu^{+3} in the preform were compared with those of phosphate, silicate and germanate glasses. For Eu^{+2} emission, a linear relation between excitation and maximum emission wavelength has been observed as excitation wavelength increases beyond 375 nm. Infrared absorption spectra were also analyzed for the preform.

1. Introduction

We have fabricated a Eu-doped preform and fiber using modified chemical vapor deposition (MCVD) in conjunction with a novel aerosol delivery technique [1]. Several other methods have been developed to incorporate rare earth ions in optical fiber cores due to the low vapor pressure of rare earth compounds. These are solution doping [2,3] and volatile halide methods [4]. We believe the aerosol delivery technique [1] possesses several advantages, i.e., ease of application, minimal use of precursors (20–30 ml), efficient structuring of the radial index profile as well as low OH^- content.

Recently, photosensitivity [5,6] and second harmonic generation [7] were observed in Ge-free rare earth-doped fibers. A Eu-doped fiber has shown an index change of 10^{-5} when irradiated by a KrF excimer laser (249 nm) [5]. Photosensitivity has been mainly observed in germanosilicate fibers using laser irradiation at 488 nm and 245 nm [8,9]. Even though the mechanism of this phenomenon is not completely understood, the index change has been attributed to photo bleaching of the strong GeO absorption band at 244 nm [10]. Photosensitivity has been also reported in Eu^{+3}-doped bulk glasses at the 465 nm Ar ion laser line resonantly tuned to $^7F_0 \rightarrow {}^5D_2$ transition of the ion [11]. This phenomenon was explained in terms of a structural change caused by thermal relaxation between $^5D_2$ and $^5D_0$ levels of the Eu^{+3} ion.

The origin of photosensitivity in the UV of this germanium-free Eu-doped fiber cannot be explained either by mechanisms present in germanosilicate fibers or by that of Eu^{+3}-doped glasses. We anticipate that spectroscopic studies of our Eu-doped fiber preform and a comparison with germano-silicate glasses will lead to a better understanding of photosensitivity.

In the following, we describe the fabrication and characterization of a Eu-doped aluminosilicate preform and fiber. Spatially resolved UV–visible absorption spectra of the preform and the

Correspondence to: Dr T.F. Morse, Laboratory for Lightwave Technology, Division of Engineering, Brown University, 182 Hope Street, Providence, RI 02912, USA.

attenuation spectra of the fiber have been measured to aid in understanding the origin of UV photosensitivity of the fiber. The excitation and emission spectra of the preform were measured to analyze valence states of Eu ions and their spectroscopic characteristics in the glass. The site symmetry of the glass structure around the Eu^{+3} ion in the preform was also inferred from the spectra, and the structure of the glass made by MCVD with an aerosol delivery technique was compared with those of glasses made by melting. Detailed IR spectra were taken to study the glass structure of the preform by vibrational mode analysis.

2. Fabrication and sample preparation

The fabrication process cited above is shown schematically in fig. 1. Twelve cladding layers were formed by conventional MCVD using $SiCl_4$ and $POCl_3$ on a Heraeus Amersil Heralux tube. The two core layers were formed using only aerosol deposition. An organometallic solution, described below, was nebulized with a 1.5 MHz transducer and transported with He as a carrier gas into an MCVD substrate tube. The composition of the organometallic solution was as follows: 8.0 ml TEOS (tetraethyl orthosilicate), 3.0 ml $Al(OBu)_3$ (aluminium-tri-*sec*-butoxide), 0.4 ml $PO(OBu)_3$ (tributyl-phosphate), 0.3 g $Eu(tmhd)_3$ (2,2,6,6-tetramethyl-3,5-heptanedionate europium) dissolved in 5 ml Cl_3BrC (bromo-trichloromethane) and 12 ml MEA (methoxy-ethyl-acetate). The formation of a very fine white powder was observed at a relatively low temperature around 350°C (measured at the outside of the substrate tube). The powder was a multicomponent oxide soot produced from metallic precursors. The organic rest left the reaction zone as vapor. As the temperature increased above 350°C, carbon formation caused by the pyrolysis of the organic rest darkened the oxides. The formation of amorphous multicomponent oxides from these precursors was observed at relatively low temperature in the absence of oxygen. A high temperature reaction was chosen to increase thermophoretic efficiency, and the removal of carbon and OH^- was carried out as follows. The soot was dehydrated at 1200°C on the MCVD lathe and using oxygen and the carbon was burned to CO_2 at 1350°C. The removal of carbon in the glass was confirmed by IR spectra discussed below. The soot was then sintered with two passes of the torch with the temperatures at 1500°C and 1900°C. Finally, the substrate tube was collapsed into a fiber preform at 2100°C. A detailed de-

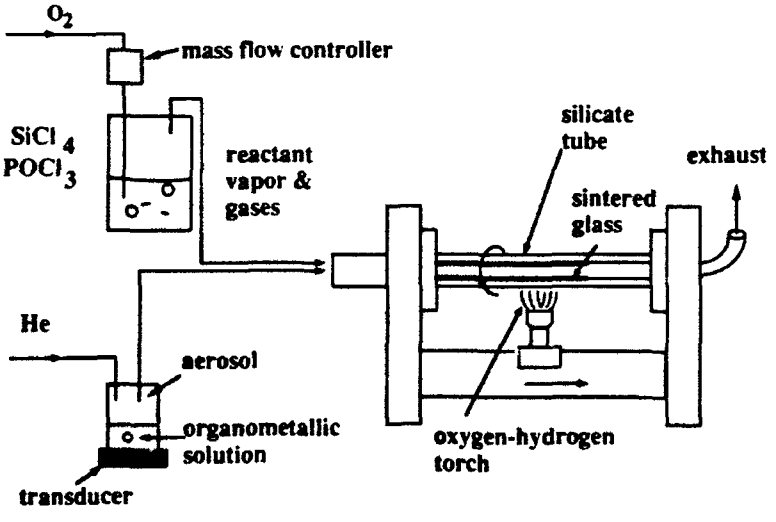

Fig. 1. Schematic of MCVD with an aerosol delivery technique.

scription of the process has been published elsewhere [1].

The preform diameter was 14.2 mm with a core diameter of 1 mm. A section of preform was cut longitudinally into a slab and polished for spectroscopic measurements. The final sample size was $15 \times 14.2 \times 0.55$ mm^3 with a 1 mm wide core. The remainder of the preform was drawn into 122 μm fiber with a core diameter of 8.6 μm. The difference between the core and the cladding indices was $\Delta n = 0.0025 \pm 0.0001$, and the index profile of the fiber is shown in fig. 2. The composition of the core was determined by wavelength dispersive X-ray microprobe analysis, and the average weight percent is given as follows: 93.74% SiO_2, 4.9% Al_2O_3, 0.7% P_2O_5, ≈ 0.1% Eu_2O_3, ≈ 0.5% EuO. The analysis provided the total concentration of all europium ions. The concentration of Eu_2O_3, (Eu^{+3}) was determined separately by comparing the emission and excitation spectra of the preform with those of a Eu^{+3}-doped alkaline silicate glass provided by J.T. Kohli of Schott Glass Technology. This Eu^{+3}-doped alkaline silicate glass had a composition in weight percent as follows: 0.99% Eu_2O_3, 2.99% LiO_2, 7.23% Na_2O, 4.71% K_2O, 84.08% SiO_2.

3. Data and results

3.1. UV–visible absorption spectra

The energy levels of Eu^{+2} and Eu^{+3} ions in crystals are shown in fig. 3. For the Eu^{+2} ion, the $4f^7 \leftrightarrow 4f^65d^1$ transitions are electric dipole allowed, producing blue–green fluorescence with a broad bandwidth and high luminescence output [12].

In Eu^{+3}, the transitions are within the 4f shell and produce orange–red luminescence. These are allowed magnetic dipole transitions and forced electric dipole transitions [13]. The dark circles indicate the levels from which emission occurs and less probable transitions are shown as open circles. In Eu^{+2} ions, the $4f^65d^1$ level is split into e_g and t_{2g} levels by a cubic crystal field [14]. The Eu^{+3} ion energy levels are shown and include a charge transfer state (CTS) as well as $f \leftrightarrow f$ transitions. In the case of oxide glass hosts, the CTS is caused by an electron jumping from surrounding oxygen atoms to a partly filled f shell of the Eu^{+3} ion [13].

The spatially resolved absorption spectra of the preform sample were measured in the 200–700 nm range with a Perkin–Elmer 552 UV–VIS

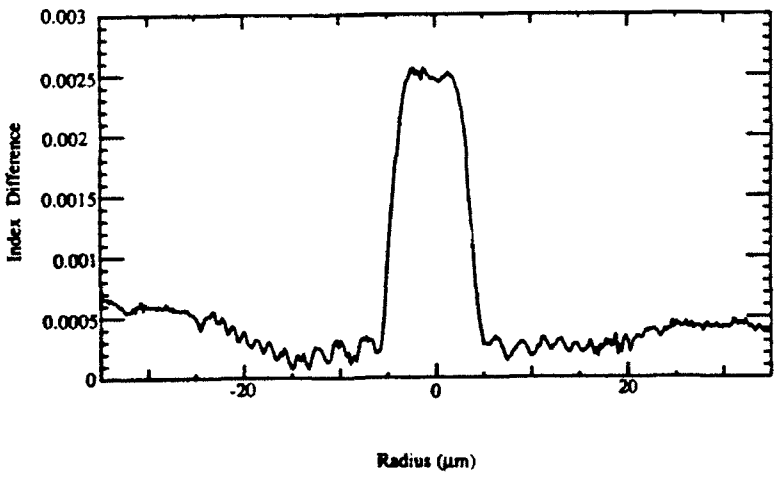

Fig. 2. Refractive index profile of the Eu-doped fiber.

spectrophotometer and the results are shown in fig. 4. The spectra were taken from both the core center and the core–cladding interface using a micropositioner to translate the sample. At the center of the core, two absorption bands centered at 255 nm and 302 nm were observed as well as a 316 nm band at the shoulder of the 302 nm band. As the probed position was moved toward the core–cladding interface, the resolution of the three UV peaks increased; however, their intensities decreased. Because of the small absorption length (0.55 mm) of the sample, the weak absorption bands of Eu^{+3} in the visible range were not detected and are not shown in fig. 4. However, these were apparent in the fiber where the attenuation was measured using a cut-back method (from 10 to 3 m) with an optical spectrum analyzer (Ando AQ6312B). In this measurement, the absorption peaks of Eu^{+3} were well resolved. The spectrum in fig. 5 is consistent with the excitation spectra in fig. 6. Based on the reported data [14], the 255 and 316 nm bands are assigned

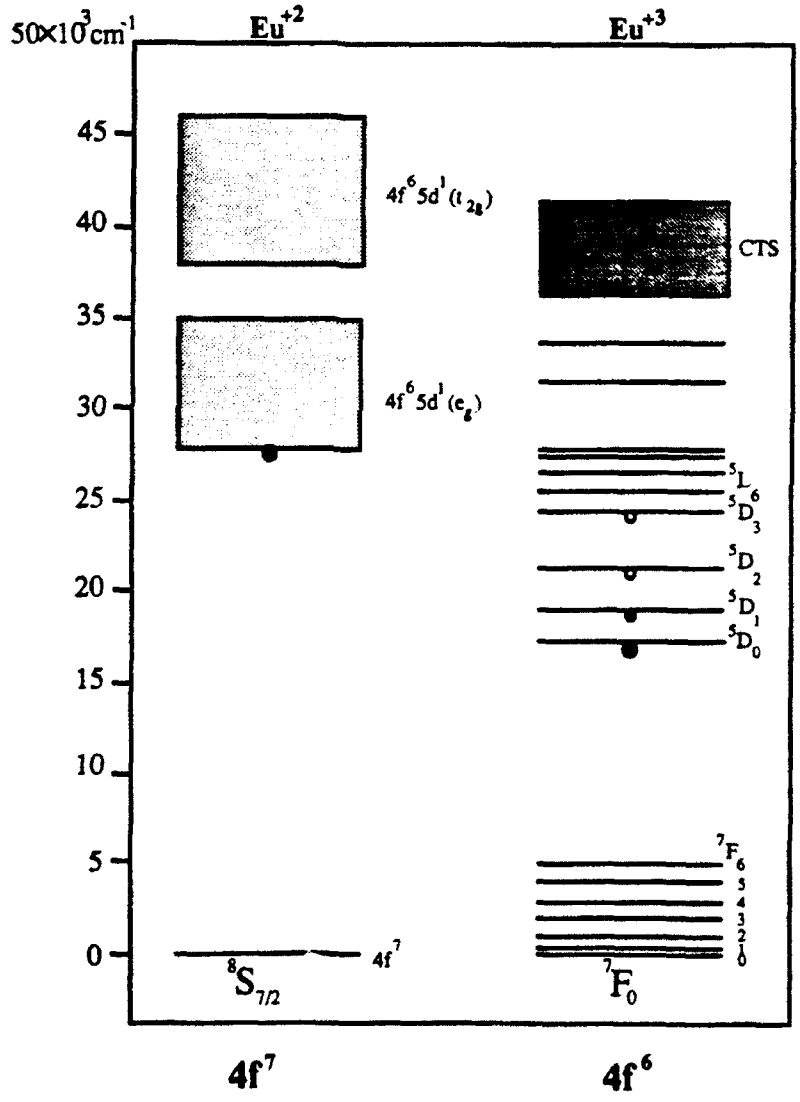

Fig. 3. Energy levels of Eu ions in crystals as reported in ref. [12]. Here CTS is the charge transfer state.

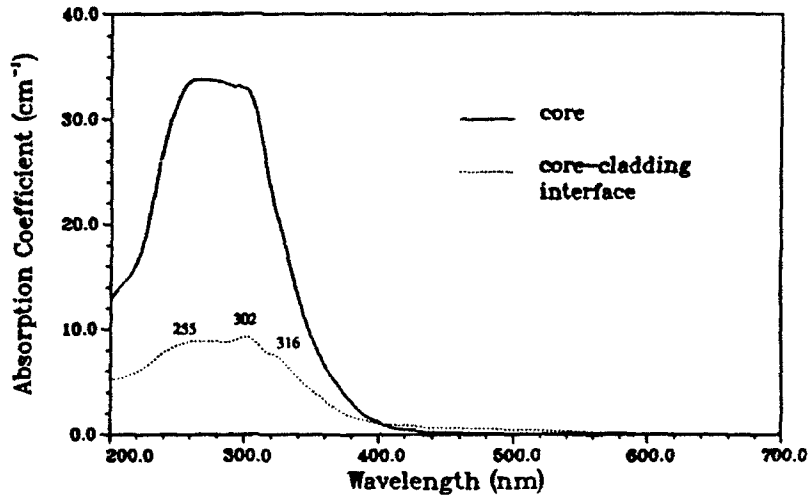

Fig. 4. Absorption spectra of the core and the core–cladding interface of the preform described in the text, in the 200–700 nm region.

to the $4f^7 \rightarrow 4f^6 5d^1(t_{2g})$ and $4f^7 \rightarrow 4f^6 5d^1(e_g)$ transitions of Eu^{+2} respectively. The 302 nm band is associated with energy transfer from Eu^{+2} to Eu^{+3} based on the observation in the excitation spectra discussed in the following sec

3.2. Excitation and emission spectra

The excitation and emission spectra of the perform core were measured using a Spex DM3000F monochromator with a Xenon lamp whose minimum bandwidth is 0.36 nm. The excitation spectra were monitored with emission at 422 nm and 616.5 nm, which correspond to the $4f^6 5d^1(e_g) \rightarrow 4f^7$ transition of Eu^{+2} and the $^5D_0 \rightarrow {}^7F_2$ transition of Eu^{+3}. The results are shown in fig. 6. For the excitation spectrum of Eu^{+2} ion, the $4f^7 \rightarrow 4f^6 5d^1(e_g)$ transition band centered at 316 nm was observed. The Eu^{+3} excitation spectrum showed another broad absorption band cen-

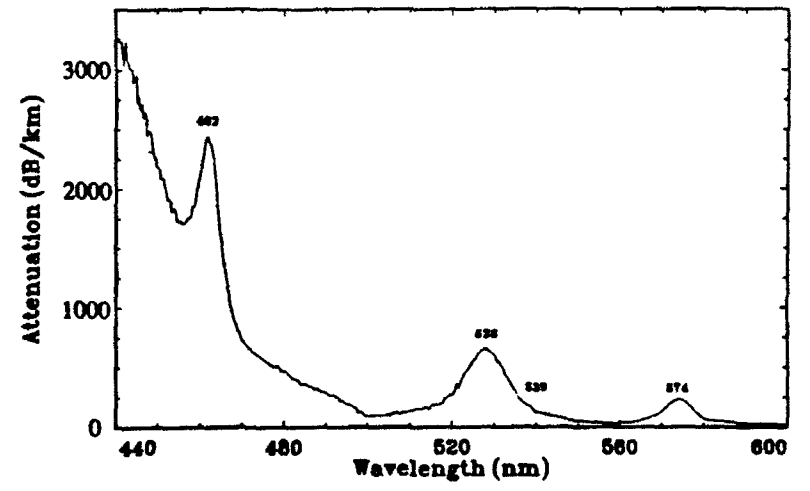

Fig. 5. Attenuation spectrum of the fiber drawn from the preform, the spectrum of which is shown in fig. 4.

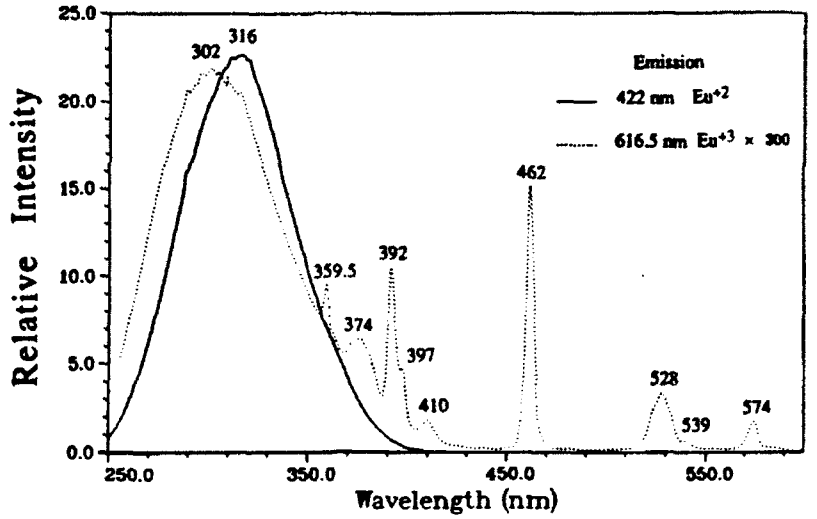

Fig. 6. Excitation spectra of Eu ions in the preform. Note that the maximum of the $4f^6 5d^1(e_g) \rightarrow 4f^7$ emission band at 422 nm was monitored for Eu^{+2} ions and that of the $^5D_0 \rightarrow {}^7F_2$ emission band at 616.5 nm was monitored for Eu^{+3} ions.

tered at 302 nm in addition to sharp f → f transitions.

We also have measured the excitation spectrum for a Eu^{+3}-doped alkaline silicate glass provided by Schott Glass Technology. This glass had a Eu^{+3} concentration of 0.99 wt%, and Eu^{+2} ions were not present. The excitation spectra were taken for the emission at 610 nm, the maximum in the $^5D_9 \rightarrow {}^7F_2$ transition of Eu^{+3} in this glass. The excitation spectra of Eu^{+3} ions permitted a comparison of both glasses so that the study of the behavior of Eu^{+3} in the presence of Eu^{+2}

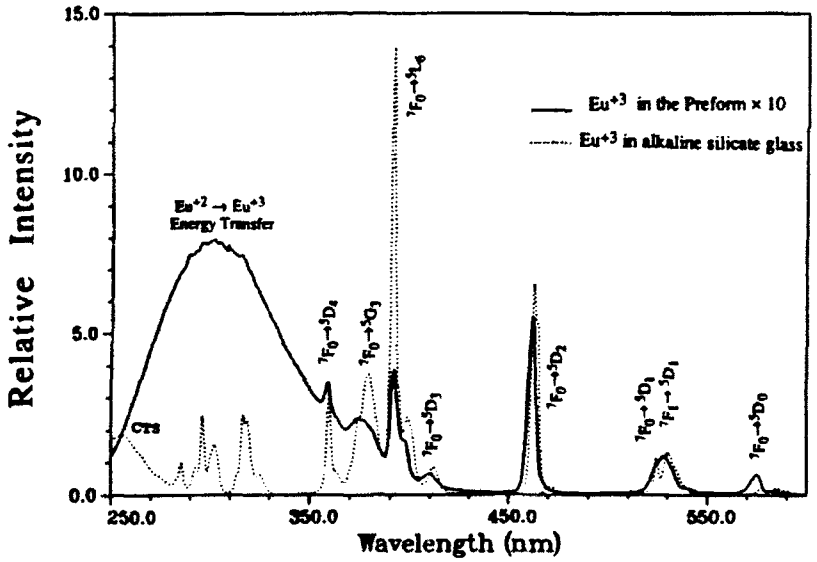

Fig. 7. Comparison of excitation spectra of Eu^{+3} ion in the preform and an alkali silicate glass. Here the maximum of the $^5D_0 \rightarrow {}^7F_2$ emission was monitored. It occurred at 616.5 nm in the preform and 610 nm in the alkali silicate glass.

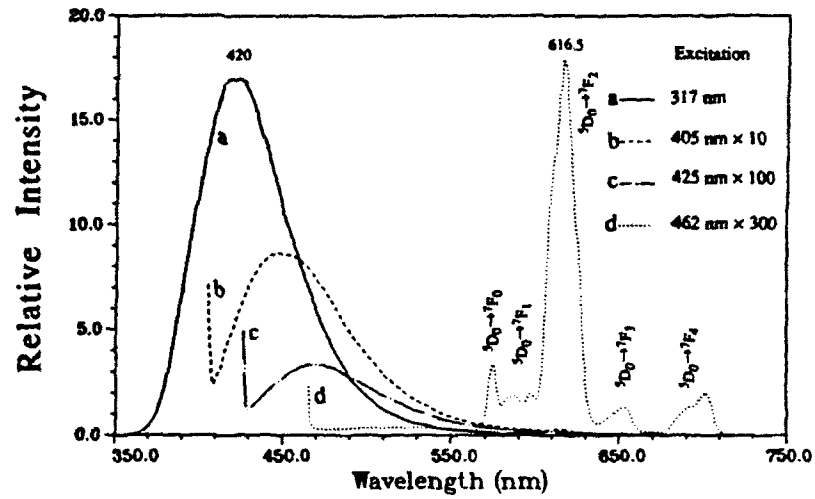

Fig. 8. Emission spectra of the preform when excited at 317 nm (———, a), 405 nm (- - - -, b), 425 nm (– – –, c) and 462 nm (· · · · · ·, d), where the emission at $\lambda > 570$ n is due to the Eu^{+3} ions and the main emissio.. band in the 350–570 nm region is due to Eu^{+2} ions.

ions may be carried out. The excitation spectra of Eu^{+3} in both preform and the alkaline silicate glass are shown in fig. 7. The broad band near 302 nm was observed in the preform; however, in the alkaline silicate, this was absent. The band at 302 nm in the preform appeared to be a superposition of sharp UV lines of Eu^{+3} superimposed on the broad $4f^7 \rightarrow 4f^6 5d^1(e_g)$ band of Eu^{+2}. The efficiency of UV excitation for the $^5D_0 \rightarrow ^7F_2$ transition of Eu^{+3} in the preform increased and we believe this resulted from the presence of Eu^{+2} in the preform. Similar observations have been reported for Pb^{+2} and Eu^{+3} co-doped glasses [15]. These were attributed to energy transfer from the sensitizing ion Pb^{+2} to Eu^{+3}. This leads us to believe that energy transfer from Eu^{+2} to Eu^{+3} was responsible for the 302 nm band, which is a new energy transfer mechanism. We have not yet determined whether the transfer is radiative or non-radiative and variation of the

Table 1
Assignment of radiative transitions

Absorption (nm)		Emission (nm)	
Eu^{+2}			
$4f^7 \rightarrow 4f^6 5d^1(t_{2g})$	255	$4f^6 5d^1(e_g) \rightarrow 4f^7$	420
$4f^7 \rightarrow 4f^6 5d^1(e_g)$	316		
Eu^{+3}			
Energy transfer $Eu^{+2} \rightarrow Eu^{+3}$	302	$^5D_1 \rightarrow ^7F_1$	528, 539
$^7F_0 \rightarrow ^5D_4$	359.5	$^5D_0 \rightarrow ^7F_0$	574.5
$^7F_0 \rightarrow ^5G_3$	374	$^5D_0 \rightarrow ^7F_1$	583, 587.5, 597
$^7F_0 \rightarrow ^5L_6$	392, 397	$^5D_0 \rightarrow ^7F_2$	610, 616.5, 625
$^7F_0 \rightarrow ^5D_3$	410	$^5D_0 \rightarrow ^7F_3$	653.5
$^7F_0 \rightarrow ^5D_2$	462	$^5D_0 \rightarrow ^7F_4$	692, 702
$^7F_0 \rightarrow ^5D_1$	524		
$^7F_1 \rightarrow ^5D_1$	528, 539		
$^7F_0 \rightarrow ^5D_0$	574		

concentration of Eu ions is being studied to determine the dominant contribution.

Emission spectra are shown in fig. 8 with excitation wavelengths at 317, 405 and 425 nm for Eu^{+2} and at 462 nm for Eu^{+3}. As the excitation wavelength for the Eu^{+2} ion increased from 317 nm to 405 and 425 nm, the peak wavelength of emission also increased. This behavior is discussed below. The assignments of the radiative transitions are summarized in table 1.

3.3. IR spectra

Vibrational spectroscopy may be used to obtain information on the effects of glass composition and different processing techniques [16]. In this study, IR absorption spectra of a preform fabricated by MCVD using an organometallic aerosol delivery technique were measured and vibrational modes were analyzed. Transparent pellets were made from mixed powder of 98 wt% KBr and 2 wt% preform core. The absorption spectra were measured using a Perkin–Elmer 1600 FT IR spectrophotometer in the infrared region between 200 and 2000 cm^{-1}. The spectrum is shown in fig. 9. The absorption bands of the preform centered at 465, 800, 1060, and 1130 cm^{-1} were measured, consistent with the intrinsic bands of the silica tetrahedra [17].

In the fabrication process, carbon was present in the glass and additional processing, described above, was needed to eliminate it. Vibrational modes of carbon-containing compounds in such a system would occur in the infrared at, for example [18]: C–H stretching (2940-2855 cm^{-1}), H–C–H symmetric bending (1470 cm^{-1}) and asymmetric bending (1385 cm^{-1}), and Si–O–C bending (1100-1050 cm^{-1}). These bands would be sharp compared with the bands of the silica glass network, so trace amounts of carbon compounds should be detected in the IR spectra as a superposition of sharp carbon peaks on broad silica bands. No such peaks were observed and we believe carbon compounds were eliminated from the glass matrix.

For a multi-component glass, the vibrational modes of non-bridging bonds can be detected near 900 cm^{-1} as a consequence of different oxygen coordination numbers for the cations [19]. In the aluminosilicate glass perform investigated here, there was only a weak band around 920 cm^{-1}, and aluminium ions, acting as network formers, were found to have a coordination number of four, as in the SiO_4 tetrahedra.

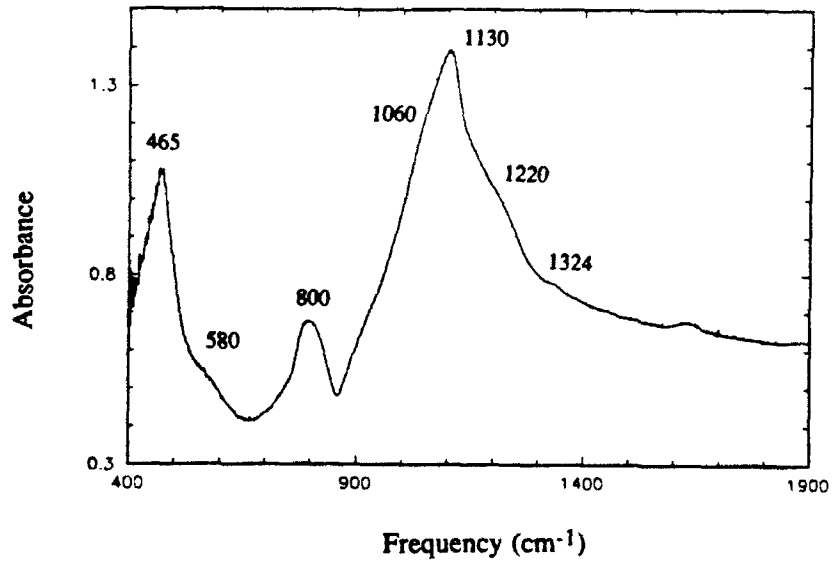

Fig. 9. IR absorption spectrum of the core of the preform described in the text.

AD-A261 488 RESEARCH SUPPORT FOR THE LABORATORY FOR LIGHTWAVE TECHNOLOGY(U) BROWN UNIV PROVIDENCE RI DIV OF ENGINEERING T F MORSE 31 DEC 92 AFOSR-TR-93-0102 2/2

UNCLASSIFIED AFOSR-90-0062 NL

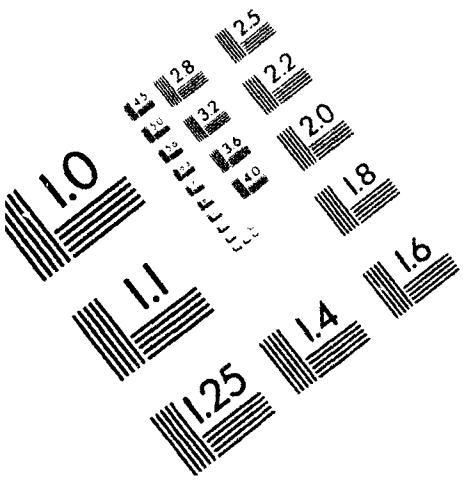

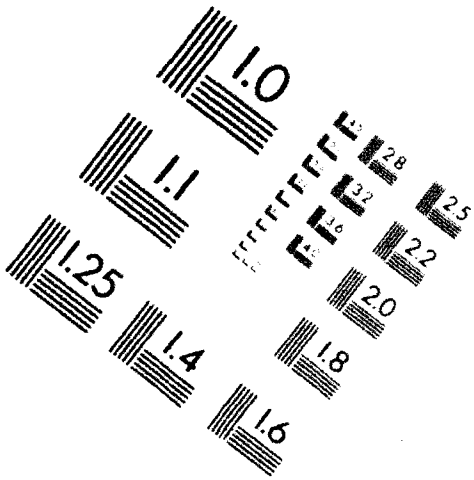

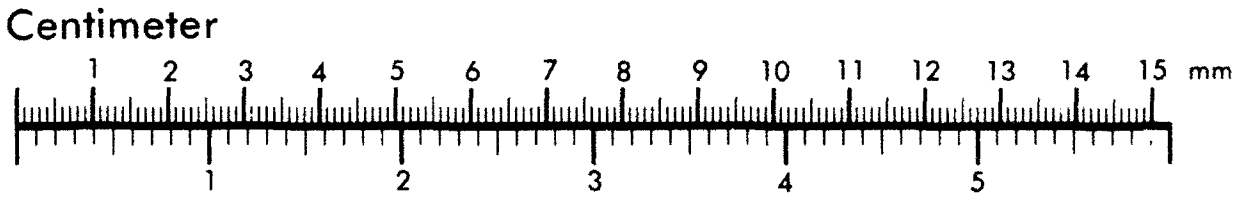

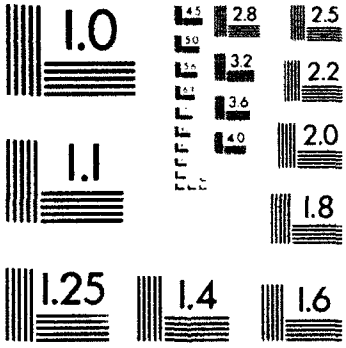

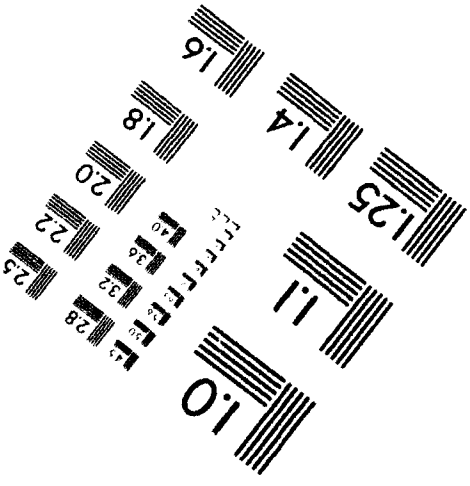

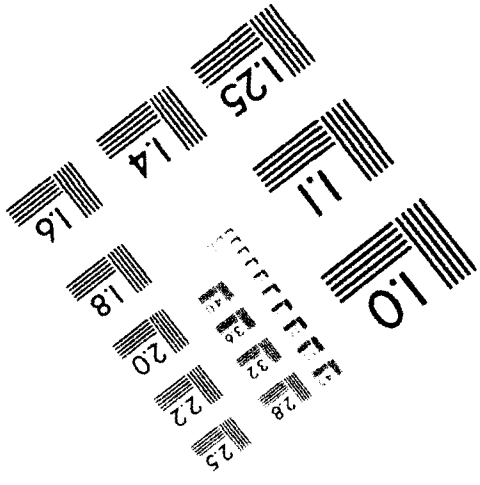

Table 2
Assignment of vibrational modes

IR bands (cm^{-1})	Assignment
465	$\nu 4$ (TO) Si–O–Si bending
580	$\equiv Si^{+}\ ^{-}O–Si\equiv$ defects
800	ν_1 (TO) Si–O stretching
1060, 1130	ν_3 (TO) Si–O stretching
1220	asymmetric stretch of SiO_4 unit in the chain influenced by the bonding configuration relative to Eu ion
1324	P=O bond stretching

The ligand field of rare earth ions can affect the neighboring bonding configuration of the glass network and such changes in the IR and Raman bands have been reported by Sun and Risen [20] for Pr^{+3} and Dy^{+3} ions in phosphate glasses. We noted a similar phenomenon, in that an additional band near 1220 cm^{-1} was observed at the shoulder of a Si–O stretching band centered at 1130 cm^{-1}. This band was believed to be caused by an asymmetric stretching of SiO_4 unit influenced by the bonding configuration relative to Eu ions.

A weak band centered at 580 cm^{-1} was observed. According to Bates et al. [21], this was due to electronic defects similar to Si E′ centers represented as $\equiv Si^{+}\ ^{-}O–Si\equiv$.

In addition to these bands, a weak band near 1324 cm^{-1} was assigned as the P—O bond stretching mode in accordance with reported data [17]. A very weak OH vibrational mode was found near 1600 cm^{-1}. The spectral positions of the bands and their assignments are given in table 2.

4. Discussion

A comparison of UV-photorefractivity between the same Eu-doped aluminosilicate fiber and Ge-doped fibers has been reported by Hill et al. [22]. The magnitude and spectral dispersion of the index change were reported to be nearly identical for both the Eu-doped aluminosilicate and the Ge-doped fiber for measurements made under the same experimental conditions. In fig. 4, the strong UV absorption band near 255 nm has been assigned as the $4f^7 \rightarrow 4f^6 5d^1(t_{2g})$ of Eu^{+2} ions and photorefractivity was observed in this band by using KrF excimer laser at 249 nm. This relation between UV absorption bands and photosensitive wavelength range has been observed in germanosilicate fibers [10], which suggested that the GeO absorption band was responsible for photorefractivity of the fibers.

In this Eu^{+2}/Eu^{+3}-doped fiber, there was no germanium present and only the doped ions could be related to the UV-photosensitivity. Based on similarities in the UV absorption spectra and photorefractivity between this Eu-doped fiber and Ge-doped fibers, we speculate that the photorefractivity in the Eu-doped fiber is related to the Eu^{+2} ion.

It was found that the fabrication process provided a Eu^{+2} rich environment in the fibers studied. Attempts to control the oxidation state of Eu ion by variation of the precursors have met with some success. The formation of different oxidation states for the Eu ions and their spatial distribution in the preform is not fully understood. We have also used nitrate salts in an aqueous solution instead of organometallic precursors. The nitrates were chosen to investigate the role of carbon in the organometallic soots as a reducing agent. The precursors were provided by a solution of 0.9 g $Al(NO_3)_3 \times 9H_2O$, 0.5 g $Eu(NO_3)_3 \times 6H_2O$ and 2.0 g Aerosil 200 in 48 ml H_2O and 2 ml HNO_3. Aerosil 200 is an extremely fine SiO_2 powder with a surface area of 200 m^2/g. It was dispersed in the solution using an 1.5 MHz ultrasonic bath. The HNO_3 was added to hydrolyze the surface of the powder and thus keep the viscosity low. The deposition and collapse cycle were run in a pure O_2-atmosphere in order to make an oxidizing condition to favor of Eu^{+3} ions. During the sintering cycle at up to 1900°C, we observed a weak red thermoluminescence from the perform which was attributed to Eu^{+3}. When the temperature was increased to 2100°C, the thermoluminescence started to shift towards the blue color. After the first collapse-pass at 2100°C the fluorescence had entirely the blue color of Eu^{+2}. From these experimental observations, we concluded that the Eu^{+3} was less stable under the collapse conditions. The conditions under which the glass was deposited did not influence

Table 3
Comparison of $^5D_0 \rightarrow {}^7F_J$ Transitions of Eu^{+3}

Transitions	Max λ (nm)	RA [a]	RI [b]	RI (P_2O_5)	RI (SiO_2)	RI (GeO_2)
$^5D_0 \rightarrow {}^7F_0$	574.5	0.71	1.70	0.036	0.130	0.110
$^5D_0 \rightarrow {}^7F_1$	597.0	1.00	1.00	1.000	1.000	1.000
$^5D_0 \rightarrow {}^7F_2$	616.5	7.91	9.15	3.000	4.255	6.666
$^5D_0 \rightarrow {}^7F_3$	653.5	0.49	0.67	0.219	0.314	0.260
$^5D_0 \rightarrow {}^7F_4$	702.0	0.72	1.03	1.026	0.398	0.666

[a] RA: relative area; [b] RI: relative intensity.
The wavelengths are for the aluminosilicate glass preform and the data for other glasses are from the ref. [23].

this behavior. Carbon did not play any significant role as a reducing agent. This preform was phase-separated due to high concentration of dopants and detailed spectroscopic studies have not been carried out.

In fig. 7, the excitation bands of Eu^{+3} in the preform showed different behavior than the Eu^{+3} ions present in an alkaline silicate glass. A significant decrease in intensity of the $^7F_0 \rightarrow {}^5L_6$ (392 nm) was observed in the preform compared with the alkaline silicate glass. In the preform, the excitation bands of Eu^{+3} were more broadened and the doublet of $^7F_0 \rightarrow {}^5D_2$ visible in the alkaline silicate was no longer resolved. In addition, the $^7F_0 \rightarrow {}^5D_1$ and $^7F_1 \rightarrow {}^5D_1$ transitions were not resolved clearly in the preform.

In curve d of fig. 8, emission lines for transitions from $^5D_1$ and $^5D_0$ to ^7F_J levels of Eu^{+3} are shown. Among these transitions, only the $^5D_0 \rightarrow {}^7F_1$ transition is magnetic dipole allowed with selection rules $\Delta J \leq 1$, and $\Delta L = 0$, $\Delta S = 0$, $\Delta l = 0$ [23]. The $^5D_0 \rightarrow {}^7F_2$ emission line has been called the hypersensitive line because it is sensitive to the crystal field mixing of f and d orbitals [13]. From the emission intensity ratio between the $^5D_0 \rightarrow {}^7F_2$ and $^5D_0 \rightarrow {}^7F_1$ transitions, it was possible to estimate the mixing of 4f with 5d orbitals in the host material [24]. The area under the

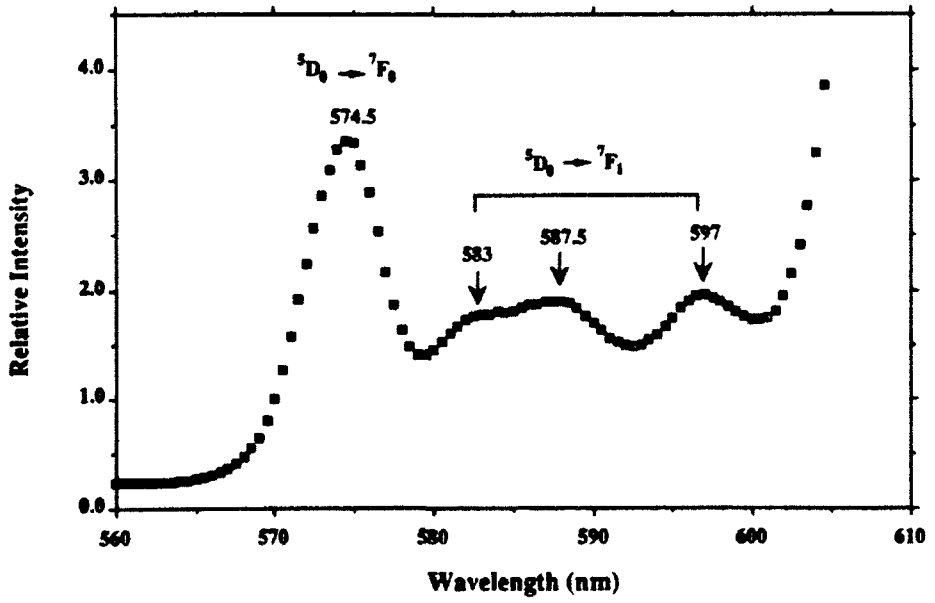

Fig. 10. Emission spectrum of Eu^{+3} ion in the preform in the 560–610 nm region. Here, curve d in fig. 8 is expanded to show fine structure in the spectrum.

$^5D_0 \rightarrow {}^7F_J$ fluorescence lines represents the probability of each transition [23].

The relative intensities and areas for the $^5D_0 \rightarrow {}^7F_J$ transitions for this aluminosilicate, europium-doped preform are summarized and compared with phosphate, silicate and germanate glass hosts [25]. In table 3, the intensity ratio $(^5D_0 \rightarrow {}^7F_2)/(^5D_0 \rightarrow {}^7F_1)$ was 9.15 in the aluminosilicate preform. The relative intensity of the most forbidden transition $^5D_0 \rightarrow {}^7F_0$ increased by a factor of 10 in the preform when compared with the other glasses. The mixing of the 4f and 5d orbitals of Eu^{+3} in the aluminosilicate preform made by MCVD with an aerosol delivery technique was found to be stronger than other single component oxide glasses made by melting. The

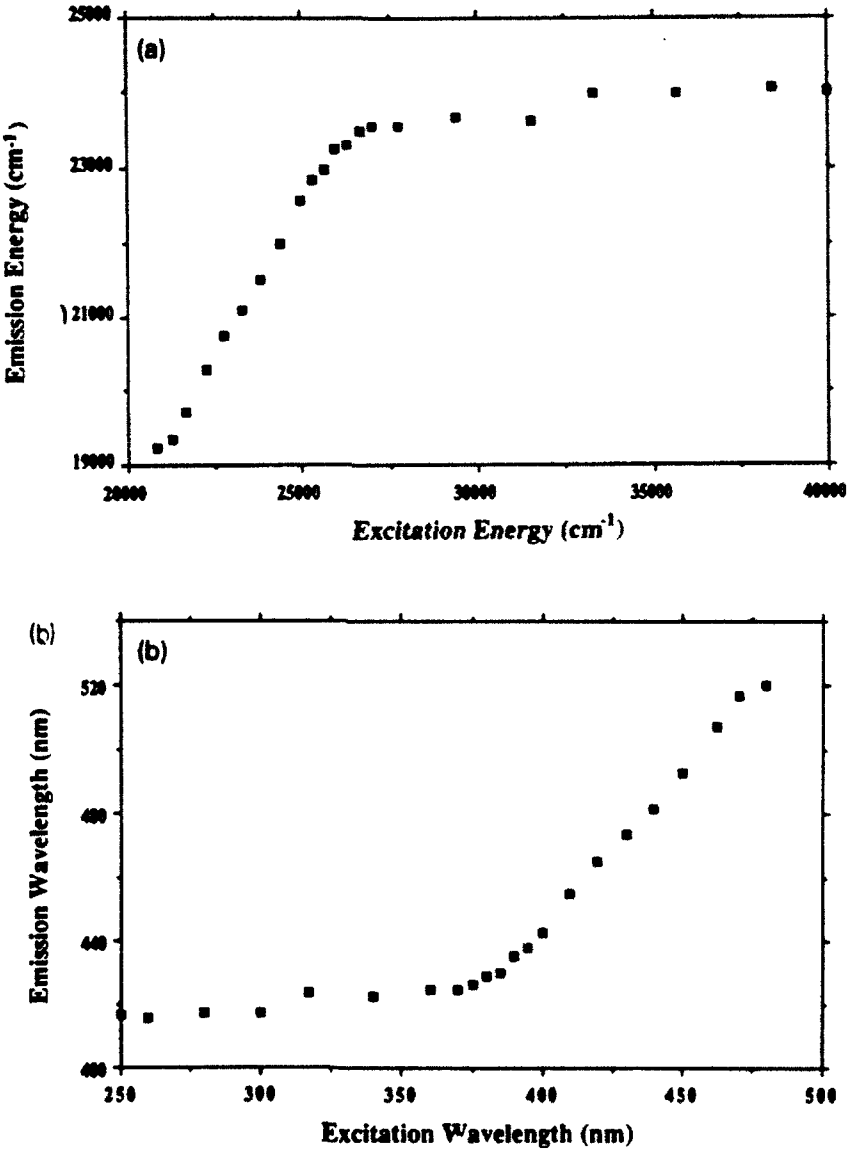

Fig. 11. Characteristics of the $4f^6 5d^1(e_g) \rightarrow 4f^7$ emission band of Eu^{+2} ions in the preform. Here the maximum of the emission band was measured for different excitations. (a) In energy scale (cm^{-1}), (b) in wavelength scale (nm).

glass formers of the preform, aluminum and phosphorus, replace the silicon in SiO_4 tetrahedra, thus producing a different environment for the Eu^{+3} ions. These glass formers in the network may also play a role in the enhancement of crystal field mixing.

As shown in fig. 10, the splitting of $^5D_0 \rightarrow {}^7F_1$ of Eu^{+3} into three lines (583, 587.5 and 597 nm) indicates the removal of the degeneracy of the $^7F_1$ state in the preform. This is taken to be consistent with the Eu^{+3} ions being in a distribution of C_s sites, as observed for Eu^{+3} in other glass hosts [23]. An estimate of the number of sites in glass can be obtained by comparing the half linewidth of $^5D_0 \rightarrow {}^7F_0$ transition in glasses with that in the Eu_2O_3 crystal [25]. The half width of $^5D_0 \rightarrow {}^7F_0$ transition in a Eu_2O_3 crystal is 2 cm^{-1}, and in the core of preform it was 220 cm^{-1}. In comparison, the half bandwidths in germanate glass, silicate glass and phosphate glass are given in table 3. The band for the preform glass was found to be more inhomogeneously broadened due to a wide distribution of sites, and this could explain the observed broadening of $^7F_0 \rightarrow {}^5D_2$, $^7F_0 \rightarrow {}^5D_1$, and $^7F_1 \rightarrow {}^5D_1$ lines in the preform.

Concerning the broad Stokes shifted $4f^6 5d^1(e_g) \rightarrow 4f^7$ emission band of Eu^{+2}, as the excitation wavelength increased beyond a certain boundary (375 nm) near the edge of the $4f^7 \rightarrow 4f^6 5d^1(e_g)$ absorption band, the maximum of the emission also increased in the preform. This is shown for excitation at 317, 405 and 425 nm, for example, as curves a, b and c, respectively, in fig. 8. A linear relation between the excitation and emission was observed from a plot of many such curves and is presented in fig. 11. This behavior is similar to the reported results for Eu^{+3} in aluminosilicate bulk glass [26]. The relaxation energy, which is the difference between excitation and the energy at the maximum of the emission band, is plotted for Eu^{+2} as a function of the excitation energy in fig. 12. In the figure, evidence for two different non-radiative relaxation mechanisms is observed. For the absorption bands of Eu^{+2} between 27000 and 40000 cm^{-1}, the relaxation energy shows a linear dependence on excitation energy. Near the absorption edge where the linear correlation between excitation and emission started, the relaxation energy remained in the range of 2000–3000 cm^{-1}.

The excitation and emission bands of the Eu^{+2} ion have been reported in binary alkaline earth silicate hosts with various composition of CaO,

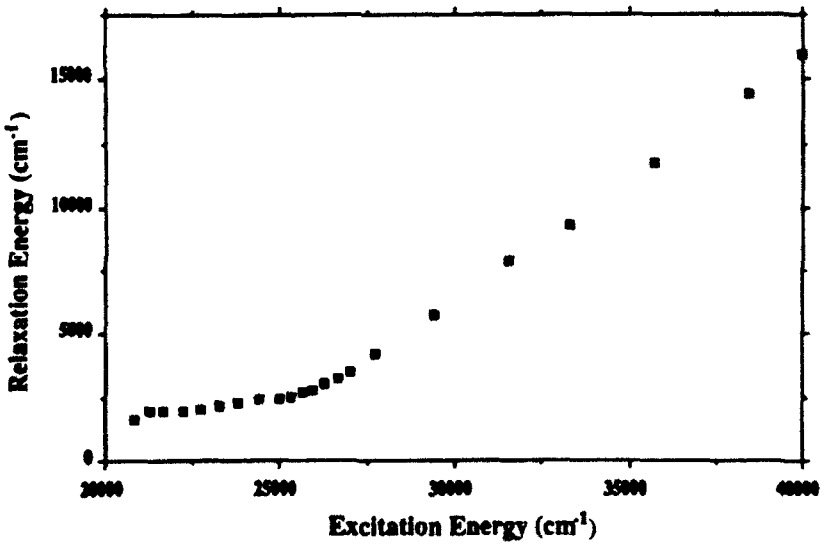

Fig. 12. Relaxation energy as a function of excitation energy for Eu^{+2} ion, where the relaxation energy is defined as the difference between the excitation energy and the energy at the maximum of the emission band of Eu^{+2} ions.

MgO and SiO_2 [27]. For $CaO \cdot MgO \cdot 2SiO_2$, whose local structure is monoclinic, the fluorescence was centered around 430 nm. The absorption bands were near 250 and 350 nm, similar to this study. For $3CaO \cdot MgO \cdot 2SiO_2$, and $3CaO \cdot 3MgO \cdot 2SiO_2$ whose structures are orthorhombic and tetragonal respectively, the emission bands shift to 480 and 520 nm with excitation bands extended to longer wavelengths. The spectra of our aluminosilicate preform show that the Eu^{+3} ions are in a distribution of sites, and this appears to be true also for Eu^{+2}. Compared with the fluorescence and excitation spectra of the Eu^{+2} ions in the $xCaO \cdot yMgO \cdot zSiO_2$ host, in the aluminosilicate preform the majority of Eu^{+2} ions was believed to be monoclinic with a distribution of structures such as orthorhombic and tetragonal. As long as excitation energy is within the $4f^7 \rightarrow 4f^6 5d^1(e_g)$ absorption band, electrons relax down to the bottom of the $4f^6 5d^1(e_g)$ level of Eu^{+2} in a monoclinic host with multiphonon emission. From this energy state, the emission occurs around 420 nm regardless of the excitation energy. The relaxation energy shows a linear dependence on excitation indicating a typical Stokes shifted fluorescence with multiphonon emission. Beyond the band edge, the distribution of absorption bands of different structures become evident. Clearly, the color of the emission depends on the specific sites excited.

5. Conclusions

The UV photosensitivity of the Eu-doped aluminosilicate fiber was found to be related to the presence of Eu^{+2} ions since the photosensitive wavelength (249 nm) coincided with the $4f^7 \rightarrow 4f^6 5d^1(e_g)$ absorption band of the Eu^{+2} ion. Energy transfer from the Eu^{+2} ion to the Eu^{+3} ion was observed in the UV range with an enhancement of the UV excitation for the $^5D_0 \rightarrow {}^7F_2$ transition of Eu^{+3}. The mixing of d and f orbitals was observed to be more effective in the preform. We observed increased inhomogeneous broadening in the preform. The linear relation between the excitation and emission of Eu^{+2} was explained by the distribution of local symmetries around Eu^{+2} ion, since they have different emission bands. The strong UV absorption associated with the Eu^{+2} and Eu^{+3} in the glass may make it possible to write index gratings holographically, and this is currently being attempted using the 337 nm emission of nitrogen laser and that at 317 nm from a frequency doubled dye laser. The main vibrational modes associated with SiO_4 tetrahedra were measured in the preform fabricated using an aerosol modification of MCVD. The results were consistent with silicate glasses made by conventional MCVD methods.

The authors are indebted to J. Kreidl for helpful discussions and to Heraeus Amersil for their generous donation of MCVD substrate tubes. They also acknowledge Dr J.T. Kohli of Schott Glass Technology for providing Eu^{+3}-doped alkaline silicate glass. They appreciate invaluable help from Professors M. Zimmt, P. Weber and G. Diebold and Mr George Tsagarapoulos of the Brown University Department of Chemistry. This work was supported by grants from NSF, Telecommunications Electrical Science/Material Science, NSF ECS-8916997, Army Research Office, Durham, Material Science, DAAL-91-G-0285 and the Air Force Office of Scientific Researches, Physics, AFOSR-90-0062.

References

[1] T.F. Morse, A. Kilian, L. Reinhart, W. Risen Jr. and J.W. Cipolla Jr., J. Non-Cryst. Solids 129 (1991) 93.
[2] J.E. Townsend, S.B. Poole and D.N. Payne, Electron. Lett. 23 (1987) 329.
[3] B.J. Ainslie, S.P. Craig and R. Wyatt, Mater. Lett. 8 (1989) 204.
[4] S.B. Poole, D.N. Payne and M.E. Fermann, Electron. Lett. 21 (1985) 737.
[5] K.O. Hill, B. Malo, F. Bilodeau, D.C. Johnson, T.F. Morse, A. Kilian, L. Reinhart and Kyunghwan Oh, in: *Optical Fiber Communication Conference*, OFC 91, San Diego, CA, Feb. 1991, Technical Digest, Postdeadline Paper PD3, p. 14.
[6] M.M. Broer, R.L. Clone and J.R. Simpson, Opt. Lett. 16 (1991) 1391.
[7] D.M. Krol and J.R. Simpson, Opt. Lett. 16 (1991) 1650.
[8] K.O. Hill, Y. Fujii, D.C. Johnson and B.S. Kawasaki, Appl. Phys. Lett. 32 (1978) 647.

[9] G. Meltz, W.W. Morey and W.H. Glen, Opt. Lett. 14 (1989) 823.
[10] M.J. Yuen, App. Opt. 21 (1982) 136.
[11] F.M. Durville, E.G. Behrens and R.C. Powell, Phys. Rev. B34 (1986) 4213.
[12] G. Blasse and A. Bril, Philips. Tech. Rev. 31 (1970) 304.
[13] G. Blasse, Handbook of Physics and Chemistry of Rare Earths (North-Holland, Amsterdam, 1979) p. 237.
[14] J.F. Owen, P.B. Dorain and T. Kobayasi, J. Appl. Phys. 52 (1981) 1216.
[15] R. Reisfeld and N. Lieblich, J. Electrochem. Soc. 121 (1974) 1338.
[16] J. Wong and C.A. Angell, Glass Structure by Spectroscopy (Dekker, New York, 1976).
[17] N. Shibata, M. Horigudhi and T. Edahiro, J. Non-Cryst. Solids 45 (1981) 115.
[18] C.J. Pouchert, ed., The Aldrich Library of Infrared Spectra, 2nd Ed (Aldrich Chemical, Milwaukee, WI, 1975).
[19] B.N. Roy, J. Am. Ceram. Soc. 73 (1990) 846.
[20] K. Sun and W.M. Risen Jr., Solid State Commun 60 (1986) 697.
[21] J.B. Bates, R.W. Hendricks and L.B. Shaffer, J. Chem. Phys. 61 (1974) 4163.
[22] B. Malo, F. Bilodeau, D.C. Johnson, I.M. Skinner, K.O. Hill, T.F. Morse, A. Kilian, L.R. Reinhart and Kyunghwan Oh, in: SPIE Proc. 1590 (Submolecular Glass Chemistry and Physics) (1991) 83.
[23] R. Reisfeld, Structure Bonding 13 (1973) 53.
[24] R. Reisfeld and L. Lieblich, J. Phys. Chem. Solids 34 (19) 1476.
[25] D.K. Rice and L.G. DeShazer, Phys. Rev. 186 (1969) 387.
[26] V.I. Arbuzov, V.A. Bonch-Bruevich, E.I. Galant, A.K Przhevuskii and M.N. Tolstoi, Fiz. Khim. Stekla 8 (1982) 216.
[27] K. Yamazaki, H. Nakabayashi, Y. Kotera and A. Ueno, J Electrochem. Soc. 133 (1986) 657.